ABSTRACT

GAS-SOLID TRANSPORT AND REACTION VIA INTERVENED EVAPORATING SPRAYS

by
Pengfei He

Fluid catalytic cracking (FCC) is a major process used for converting heavy oils to transportation fuels and light olefins. The gas-solid transport with reaction via intervened evaporating sprays in the FCC riser is specially important but complicated, with coupled mechanisms of chemical reaction and heat, momentum and mass transfer among multiple phases (liquid, solid and gas) in the restriction of wall boundary. Recent developments in FCC process models have progressed along two lines. One aims to develop composition-based kinetic models derived from molecular characterization of petroleum fractions while overlooking the hydrodynamic effect on local catalyst to oil ratio (CTO). The other aims to develop computational fluid dynamics (CFD) based models which cost too much on emphasizing flow dynamics yet not suitable for real time on-site monitor/control/optimization in industry. This work shows the efforts in developing an FCC model that strikes a right balance between the kinetics- and CFD-dominated approaches. Specifically, the feed injection zone, with multiple evaporating sprays penetrating throughout the hot gas-solid flow ambient and overlapping among each other, is integrally modeled (with coupling of FCC kinetic reactions) by geometrically cascading sub-models of single across spray and gas-solid transport. An innovative experimental method is proposed to obtain the statistical characteristics of solids wetting and solid-droplet collision probability distributions from spray impingement onto free-fall particles. This feed-zone modeling, quantifying liquid feed trajectory, droplet vaporization, gas-solid transport and vapor cracking, is capable to provide hydrodynamic and pre-cracking inlet conditions for downstream gas-solid transport in the remaining part of riser. A two-zone analytic model for FCC

riser, consisting of an entrance zone and a fully developed riser zone, is thus developed. Using a four-lump cracking kinetic model, this work shows that for the first time the commercial data of Derouin et al. (1997, [14]) can be explained and predicted. The success of the prediction reflects an inherent two-zone character of the FCC riser. Inside the entrance zone, cracking intensity is high and changes rapidly, resulting in a sharp rise in VGO conversion. Outside the entrance zone, cracking intensity is low and becomes slowly varying, giving rise to a sluggish increase in conversion. The results show that the two-zone theory is a simple, practical way of capturing the essence of physicochemical phenomena underpinning the FCC process. Further exploitation of this approach is to quantify solid back-flow in gas-solid transportation due to wall restriction. The continuous modeling, which takes into account mechanistic of radial heterogeneity by considering radial mass and momentum balances between the collision-induced diffusion and the turbulent convection of solids, is proposed. Results are partially validated against published experiment data for radial and axial distributions of both solids and gas characteristic properties. Back-flow ratio can be thus predicted quantitatively for further optimization of riser reactor.

GAS-SOLID TRANSPORT AND REACTION VIA INTERVENED EVAPORATING SPRAYS

by
Pengfei He

A Dissertation
Submitted to the Faculty of
New Jersey Institute of Technology
in Partial Fulfillment of the Requirements for the Degree of
Doctor of Philosophy in Mechanical Engineering

Department of Mechanical and Industrial Engineering

May 2014

APPROVAL PAGE

GAS-SOLID TRANSPORT AND REACTION VIA INTERVENED EVAPORATING SPRAYS

Pengfei He

Dr. Chao Zhu, Dissertation Advisor — Date
Professor of Mechanical Engineering, NJIT

Dr. Ian S. Fischer, Committee Member — Date
Professor of Mechanical Engineering, NJIT

Dr. Teh C. Ho, Committee Member — Date
Sr. Research Associate, ExxonMobil Co.

Dr. Zhiming Ji, Committee Member — Date
Associate Professor of Mechanical Engineering, NJIT

Dr. I. Joga Rao, Committee Member — Date
Professor of Mechanical Engineering, NJIT

BIOGRAPHICAL SKETCH

Author: Pengfei He

Degree: Doctor of Philosophy

Date: May 2014

Date of Birth: January 1986

Place of Birth: China

Undergraduate and Graduate Education:

- Doctor of Philosophy in Mechanical Engineering,
  New Jersey Institute of Technology, Newark, NJ, 2014
- Master of Science in Engineering Mechanics,
  Tsinghua University, Beijing, China, 2009
- Bachelor of Science in Thermal Energy and Power Engineering,
  Hefei University of Technology, Hefei, China, 2006

Major: Mechanical Engineering

Presentations and Publications:

Pengfei He, Dawei Wang, Chao Zhu, "Liquid Attachment and Momentum Transfer by Collisions between Free-fall Solids and Liquid Spray Droplets" *Powder Technology*, Vol. 239, 1-11, 2013.

Rajesh Patel, Pengfei He, Bo Zhang, Chao Zhu, "Transport of Interacting and Evaporating Liquid Sprays in a Gas-Solid Riser Reactor" *Chemical Engineering Science*, Vol. 100, 433-444, 2013.

Pengfei He, Bo Zhang, Chao Zhu, Zhiming Ji, Chao-Hsin Lin, "Dynamic Process Modeling on Depressurization by Cooling-Controlled Condensation in a Closed Chamber" *International Journal of Heat and Mass Transfer*, submitted

Pengfei He, Chao Zhu, Teh C. Ho, "A Two-Zone Model for Fluid Catalytic Cracking Riser with Multiple Feed Injectors" *AIChE Journal*, submitted

Pengfei He, Rajesh Patel, Dawei Wang, Chao Zhu, "A Continuous Model of Axial and Radial Flow Structure " *Powder Technology*, in preparation

Pengfei He, Rajesh Patel, Dawei Wang, Chao Zhu, Bo Zhang, "Hydrodynamic Model of Gas-Solids Risers Flow with Continuous Axial and Radial Flow Structure" *Proceedings of the ASME 2014 4th Joint US-European Fluids Engineering Summer Meeting & 12th International Conference on Nanochannels, Microchannels, and Minichannels*(FEDSM2014/ICNMM2014), August 3-7, 2014, Chicago, Illinois, USA

Bo Zhang, Pengfei He, Chao Zhu, Zhiming Ji, Chao-Hsin Lin, "Dynamic Process Modeling on Depressurization by Cooling-Controlled Condensation in a Closed Chamber" *Proceedings of the ASME 2014 4th Joint US-European Fluids Engineering Summer Meeting & 12th International Conference on Nanochannels, Microchannels, and Minichannels*(FEDSM2014/ICNMM2014), August 3-7, 2014, Chicago, Illinois, USA

Bo Zhang, Pengfei He, Chao Zhu, "Modeling on Hydrodynamic Coupled FCC Reaction in Gas-Solid Riser Reactor" *Proceedings of the ASME 2014 4th Joint US-European Fluids Engineering Summer Meeting & 12th International Conference on Nanochannels, Microchannels, and Minichannels*(FEDSM2014/ICNMM2014), August 3-7, 2014, Chicago, Illinois, USA

Pengfei He, Chao Zhu, Fen Du, Zhiming Ji, Chao-Hsin Lin, "Effect of Wall Cooling with Condensation on Depressurization of A Steam-Prefilled Chamber" *Proceedings of ASME 2012 International Mechanical Engineering Congress & Exposition*(IMECE2012), November 9-15, 2012, Houston, Texas, USA

Pengfei He, Rajesh Patel, Bo Zhang, Chao Zhu, "Probability Distributions of Collision and Liquid Attachment on Flowing Solids by an Atomized Liquid Spray" *Proceedings of ASME 2012 International Mechanical Engineering Congress & Exposition*(IMECE2012), November 9-15, 2012, Houston, Texas, USA

Pengfei He, Rajesh Patel, Chao Zhu, Chao-Hsin Lin, "Cooling-Induced Depressurization of a Steam-Filled Chamber" *Proceedings of the ASME/JSME 2011 8th Thermal Engineering Joint Conference*(AJTEC2011), March 13-17, 2011, Honolulu, Hawaii, USA

This dissertation is dedicated to

my daughter, April Yuzhou He, and all my unborn children, for every minute they shared/are sharing/will share with me, who tell me that life is so beautiful and mysterious;

my wife, Hua Zhou, for her faithful love, complete understanding and gelivable support, who keeps me always motivated and refreshed;

my parents, Cun He and Guowei Wang, for their endless love and unconditional support, who gave me the life to taste and enjoy the world.

Pengfei He
May 2014

ACKNOWLEDGMENT

I would like to express my deepest appreciation to Dr. Chao Zhu, who gave me guidance, supervision and research intuition, but also is a sincere friend providing experience, support, encouragement, and reassurance throughout my life during my study at New Jersey Institute of Technology. I would also like to acknowledge Dr. Teh C. Ho, Dr. Zhiming Ji, Dr. Ian S. Fischer and Dr. I. Joga Rao for their active participation on my dissertation committee.

I would like to acknowledge the Teaching/Research Assistantships from the Department of Mechanical Engineering of New Jersey Institute of Technology, ExxonMobil Research and Development Corporation, Boeing Commercial Airplanes and Petroleum Research Fund for their support. I appreciate the friendship and cooperation of Dr. Dawei Wang, Dr. Jun You, Dr. Rajesh Patel, Dr. Raivat Patel, Mr. Jiayi Tong, Mr. Yuxiang Fang, Mr. Bo Zhang and Mr. Gao Pan in the Particulate Multiphase Flow Laboratory.

I would like to express my endless gratitude to my parents, my parents-in-law and other family members, who have always supported my academic pursuits and helped me in every possible way.

Last, I want to thank my beloved wife, Hua Zhou, and my adorable daughter, April, for their love and encouragement throughout these years.

TABLE OF CONTENTS

TABLE OF CONTENTS
(Continued)

Chapter **Page**

TABLE OF CONTENTS
(Continued)

Chapter **Page**

LIST OF TABLES

LIST OF FIGURES

LIST OF FIGURES
(Continued)

Figure **Page**

LIST OF FIGURES
(Continued)

Figure **Page**

LIST OF SYMBOLS

$\bar{k}_{i0}$ Corrected pre-exponential factor for 1^{st} and 2^{nd} order reaction

ΔH_i Heat of reaction from ith cracking reaction (J/kg)

ΔM_{dp} Momentum transferred from droplet to particle by collision (kg-m/s)

Δm_d Mass of droplet attached to solid particle after collision (kg)

$\dot{m}_{ge}$ Gas entrainment mass flux rate (kg/m^2-s)

$\dot{m}_{se}$ Solid entrainment mass flux rate (kg/m^2-s)

$\dot{m}_{sp}$ Solid penetration by convection (kg/m^2-s)

$\dot{m}_v$ Droplet vaporization rate (kg/m^3-s)

$\mathbf{X}$ Space position vector (m)

A Spray cross section area; Riser cross section area (m^2)

C Conversion of VGO (wt%)

c Coefficient of polynomials

C_c Coke content in weight percentage (wt%)

C_j Molar concentration of jth component (mol/m^3)

c_p Specific heat at constant pressure (J/kg-K)

CTO Catalyst to oil mass flow rate ratio

D Diameter of riser (m)

d Diameter (m)

D_{sD} Radial transport coefficient for particles due to radial concentration gradient

E_c Convective heat transfer rate (J/s)

E_R Reaction heat transfer rate (J/s)

E_{ai} Activation energy of the ith cracking reaction (kJ/mol)

f Probability density function (pdf)

G Mass flux rate(kg/m^2-s)

g Gravitational acceleration (m/s^2)

H Height; Total height of riser (m)

h Convective heat transfer coefficient (W/m^2-K)

k_i Rate constant of ith cracking reaction

k_{sT} Turbulent fluctuation induced radial transport coefficient for particles

L Length (m); Latent heat of vaporization (J/kg)

l Perimeter of cross section of spray (m)

M Momentum (kg-m/s)

m Mass (kg)

M_j Molecular weight of jth lump (kg/mol)

N Number of particles/droplets; Number of rays for single spray

n Number density (1/m^3)

n_{RZ} Empirical Richardson-Zaki index

Nu Nusselt Number

p Pressure (Pa)

Pr	Prandtl Number
Q	Volumetric flow rate (m^3/s)
R	Radius of riser (m); Universal gas constant (J/mol-K)
r	r-coordinate; Radius position (m)
r_i	Mass based reaction rate of i^{th} cracking reaction (kg/m^3-s)
Re_p	Particle Reynolds Number
S	Slip factor
St	Stokes Number
T	Temperature (K)
t	Time (s)
U	Velocity, velocity in riser flow (m/s)
u	Velocity in spray jet(m/s)
V	Velocity in radial direction (m/s)
x	x-coordinate
y	y-coordinate
Y_i	Weight fraction (Yeild) of i^{th} lump (wt%)
z	z-coordinate; Riser height (m)
C_D	Drag coefficient
F_C	Collision force (N)
f_C	Collision force per unit volume (N/m^3)

F_D Drag force (N)

f_D Drag force per unit volume (N/m^3)

k_{i0} Empirical pre-exponential factor of ith cracking reaction (g oil/(s g cat))

Greek

α Volume fraction, Voidage

δ Liquid thickness of wet particle (m)

γ Partition function for vapor convection

λ Local catalyst to oil ratio

μ Dynamic viscosity of fluid (N-s/m^2)

Φ_s Catalyst deactivation coefficient

ρ Density (kg/m^3)

σ Characteristic bandwidth

τ Friction stress (Pa)

θ Spray injection angle (degree)

φ Spray angle of each ray (degree)

ξ Spray direction coordinate; Correction factors

Subscripts

0 Centerline

∞ Gas-solid (ambient) flow condition

a After-collision properties

c	Coke; Core regime
D	Diffusive
d	Liquid droplet
e	Entrainment
g	Gas
i	Variables in ith bin; Inlet of riser
j	Variables at jet outlet
l	Liquid
p	Particle, Penetration by convection
s	Solid phase; Species as droplet, dry or wet particles; Catalyst solid
st	Steam
T	Turbulent
t	Terminal
v	Vapor
w	Wall

CHAPTER 1

INTRODUCTION

1.1 Application Background and Research Interest

Transport of interacting and evaporating liquid sprays can be exemplified by the application of liquid feed injection for fluid catalytic cracking (FCC), which is a hydrodynamically complex oil refining process involving a vast number of reactions. It is the primary boiling-point reduction process in the petroleum and petrochemical industries. It uses a riser reactor to crack heavy petroleum fractions, such as vacuum gas oil (VGO, 340-570°C), into high-value hydrocarbons such as gasoline, diesel, and light olefins. In fact, FCC is a major producer of propylene. The importance of the FCC process is evidenced by its voluminous scientific and patent literature.

As shown in Figure 1.1, the atomized VGO spray enters the riser bottom circumferentially through multiple nozzles, collides with hot catalyst particles and is vaporized and cracked to lighter hydrocarbons and coke. The resulting vapor continues to crack as it flows upward along with the catalyst against gravity in the riser. Because of vaporization and cracking, the vapor expands, thus increasing the velocities of both reacting gas mixture and catalyst along the riser. The increased velocities, along with the vapor expansion via cracking and depressurization, dilute the catalyst volumetric concentration and hence lower the local catalyst-to-oil (CTO) ratio. Concomitant with this is the deposition of coke, a reaction byproduct, on the catalyst surface, which deactivates the catalyst. The deactivated catalyst is separated out from the hydrocarbon stream through cyclones at the riser exit. Upon regeneration via coke burning in a high-temperature regenerator, the catalyst is fed back to the riser to complete the circuit. The heat generated in the regenerator is used to vaporize and crack hydrocarbons in the riser.

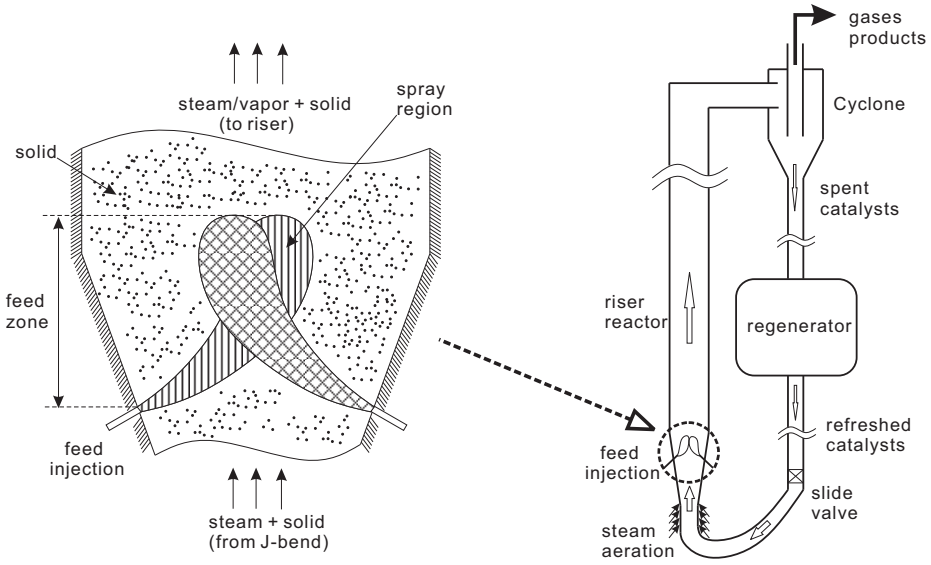

Figure 1.1 Liquid feed injection zone in FCC riser reactor.

Recent advances in analytical chemistry and computing made it possible to perform molecular speciation analyses on petroleum fractions and follow the reactions of a vast number of species computationally. This provided an opportunity for enhancing oil refining efficiency via molecular management of various hydrocarbon streams. A low- cost approach to improving the FCC process is to develop a robust process model capable of predicting how product quality is affected by feedstock composition, operating conditions, catalyst properties, and hardware configuration. Moreover, the model must also be usable for plant monitoring, on-line control, and optimization [40]. To achieve this objective, one should first obtain intrinsic kinetics from laboratory reactors. The thus-obtained intrinsic kinetic model is then used for scale-up by incorporating hydrodynamic and transport effects. To do so requires the development of a quantitative treatment of the interplay of reaction, hydrodynamics, and transport processes throughout the FCC process.

1.2 Literature Survey and Academic Challenges

Most prior FCC riser models were based on the assumption that the cracking time scale is much longer than the time scales of vaporization and interfacial transport. So the feed injection zone instantaneously reaches a thermal equilibrium state before cracking sets in. Such models generally fall into two broad categories. One is the traditional one-dimensional, homogeneous plug-flow model [80, 46] which, due to its simplicity, can accommodate a huge number of reactions, thus allowing for a composition-based model to be developed. An example of this type of model has as many as 30,000 reactions involving over 3000 species [11]. The problem with such a kinetics-dominated model is that they do not consider hydrodynamic effects that affect not only the reaction time but also the local CTO variations. At the other end of the spectrum is the computational fluid dynamics (CFD)-based models [30, 77, 13, 29]. Here the allowable number of chemical reactions is necessarily small due to limited computing power even with today's computers. The CFD-dominated models would not enable refiners to manage FCC feedstocks and products at a molecular level. Neither of the above-mentioned modeling approaches can be directly used for FCC on-line control, monitoring, and optimization. This state of affairs motivated us to develop a hybrid modeling approach aimed at striking the right balance between the two asymptotic approaches mentioned above.

Also, there is a need to address the issue of entrance cracking via development of a quantitative treatment of the riser bottom including the feed injection zone. While the modeling of feed-zone transport and reaction has gained a rapidly growing attention in the past decade, there are only a very limited number of publications available in the public domain. Research efforts have been made via experimental, theoretical and numerical approaches. Some basic experimental studies have been focused on the behavior of evaporative liquid sprays in gas-solid flows, typically using liquid nitrogen sprays injected into FCC flows at room temperature without

any cracking reactions (e.g., [73, 89, 19]). In order to explore the parametric effects, various parametric models have been proposed to investigate the fundamental characteristics of evaporative liquid sprays in gas-liquid-solid three-phase flow systems (e.g., [90, 19, 87, 65, 26]). Most of these parametric models, however, are based upon the hydrodynamic transport of a single spray in uniform and undisturbed gas-solid flows without catalytic reactions. With recent CFD developments of multiphase flow, especially with implement of sub-models (such as granular flow theory) to account for the inter-particle transfer of solids, numerical simulations of evaporating spray in dense gas-solid flows become possible (e.g., [79, 64, 48])). The CFD simulations can handle complex flows or geometry of nozzles and reactors (e.g., [75])), which provide field descriptions of phase transport and reaction yields (e.g., [74, 55, 10, 45, 4]). Most of the CFD simulations are focused on the scale of overall reactor, rather than local phase transport and interactions of spray in the feed zone. Although the gas-solid riser flow with vaporization effect has been investigated numerically, yet many have questioned the accuracy of vaporization model (e.g., [28, 51]). In fact, few CFD models of sprays are based on the mechanistic account of droplet-solids collisions that plays the dominant role in spray vaporization and transport in the feed zone.

Though spray impingement caused droplet-particle collision is an essential mechanism of interacting and evaporating liquid sprays into gas-solids flow, the literature search reveals that very few studies on droplet-particle collisions at any of the listed conditions have been reported. Most studies on droplet-particle collisions are under ideal or limiting conditions such as droplet colliding on flat solid surface (i.e., extremely large particle-to-droplet size ratio) (e.g., [54, 76, 43]) or droplet dripping onto a fixed particle (i.e., small collision velocity and particle density equivalent to infinity) (e.g., [25, 78]). Many of these studies are focused on the microscopic hydrodynamics process of droplet deformation (e.g., [34, 22]) and breakup or scattering (e.g., [31, 66, 83]) and various influential factors such as surface wettability

(e.g., [50]), surface temperature (e.g., [33, 23, 24, 85, 15, 2]) and high pressure (e.g., [17]). Moreover, most of these studies only involved a single-pair collision (typically in the center-to-center collision mode) without any statistical considerations such as off-center or oblique collision probability distributions. It can be summarized that there is little reported information on the collision-induced liquid attachment (droplet coating) and momentum transfer in terms of after-collision velocities of colliding parties. Furthermore, no studies have been reportedly attempted to obtain either experimental measurements or theoretical modeling on the statistical characterization on the liquid attachments and momentum repartition by the collisions of a liquid spray onto flowing particles.

1.3 Dissertation Objectives and Structure

The major objective of this study is to understand the mechanisms of gas-solid transportation and reaction interacted with evaporating spray in riser reactors. To this aim, several key issues is studied in prior such as spray impingement caused solids wetting and solid-droplet collision probability distributions, the multi-evaporating spray trajectory and their interactions throughout the ambient gas-solid cross flow coupled with reaction, and the wall boundary restricted solid back-flow in the gas-solid transportation. In this regards, the study is divided into several parts and presented in following chapters, respectively.

In the first part of the study, described in Chapter 2, is focused on experimental and modeling work to identify the statistical distributions of liquid attachment and collision probability of the impingement of a liquid spray onto free-fall particles. An innovative experimental method is developed and performed. With assistance of a Lagrangian trajectory model, these statistical characteristics can be obtained, which are accountable for droplet-particle collisions caused heat transfer/evaporation in feed zone injection modeling .

In the second part, illustrated in Chapter 3, a modeling work to quantify the liquid feed transport, vaporization and cracking in the feed injection zone is developed. The theoretical framework coupled the important mechanisms as three dimensional multi-spray geometrical structure with multi-phase transport, reaction and heat/mass transfer. To test the modeling capability, the three-phase transport in a feed zone with feed injected from four square nozzles have been investigated. The spray transport model builds up a mutual-penetrating structure of sprays, with each individual spray spreading and vaporizing in its associated injection plane, to predict ambient gas-solid flow passing through the evaporating planes and its pre-cracking in feed zone.

In Chapter 4, a two-zone model on riser reactor consisting of feed zone and fully developed zone is then presented and validated. Adopting feed zone modeling proposed in Chapter 3, this integrated model is able to obtain hydrodynamic and pre-cracking properties after feed zone. These obtained information is then imported as inlet conditions of downstream gas-solid flow for predicting further hydrodynamic coupled cracking reaction characteristics (e.g., unconverted VGO, production yields and selectivity).

To further explore the heterogeneous characteristics of gas-solid flow in riser reactor, the continuous modeling is elaborated Chapter 5. The dynamic transport of gas-solids in a riser leads to a highly non-uniform and complex flow distributions in both axial and radial directions. Over a cross-section of the riser beyond the dense acceleration region, a typical core-annulus pattern can be found with dilute solids transported upwards in the central core and a dense layer moving down in the wall annulus. The continuous modeling approach proposed in this study takes the mechanistic of radial heterogeneity into account, which based on the gas stagnation as well as the radial mass and momentum balances between the collision-induced diffusion and the turbulent convection of solids due to the riser wall effects.

At the end, a summary of this study and its future directions are discussed and suggested in Chapter 6.

CHAPTER 2

LIQUID ATTACHMENT AND MOMENTUM TRANSFER BY COLLISIONS BETWEEN FREE-FALL SOLIDS AND LIQUID SPRAY DROPLETS

2.1 Introduction and Research Methodology

Spray jet impingement on flowing particles is essential to many important industrial processes such as spray pigment coating, spray cooling in polymerization reactors, spray-feed coking in fluidized cokers, and spray-feed catalytic cracking in riser reactors.

During an impingement process of a liquid spray onto flowing solids, there are a wide variety of droplet-particle collision modes (such as center-to-center collision, oblique and off-center collisions) and various collision properties (including relative collision velocity and sizes of droplets and particles). The hydrodynamic mechanisms involved in such an impingement is quite complex in nature, as the process is typically coupled with droplet breakup or liquid scattering, liquid attachment or particle wetting, and re-partitions of velocities of colliding droplets and particles. Thus, in order to understand the process of spray jet impinging on particles, the investigations are focused on not only the microscopic mechanism of each droplet-particle collision modes but also the macroscopic effect of the statistical combination of different collision modes, such as the transferred momentum and mass distribution along the spray penetration.

Modeling with above mentioned industrial application backgrounds calls for the fundamental information of the statistical characterization in liquid attachment and velocity redistributions under the following conditions:

1) Both particles and droplets are fully suspended and moving;

2) Relative velocities between the colliding particles and droplets before collision are very high;

3) Sizes of droplets and particles are at the same order of magnitude;

4) Combination of various collision modes with a significant number of collisions should be included.

All of above are essential to mimic the realistic collisions between a liquid spray and dispersed flowing particles.

In this chapter, an experiment was designed and set up to investigate the statistic characteristics of liquid attachment and momentum transfer onto free-fall particles by collisions with droplets from a horizontal spray jet. Most importantly, an experimental methodology is developed to separate the individual contributions to the measurements of combined effects of droplet breakup (or liquid scattering), particle wetting (or liquid attachment), and velocity re-distribution during the droplet-particle collisions. Specifically, an individual impingement experiment, respectively with hydrophobic or hydrophilic particles of the same otherwise properties, needs to be performed under the same conditions. Consequently, the statistical probability distributions of particle wetting thickness, the colliding frequency and momentum partition along the spray penetration can be experimentally determined, which are obtained via the aid of a simple Lagrangian model developed to simulate the after collision trajectories of particles and droplets (so that, based on the locations of collection bins, the after-collision velocities of particles and droplets can be identified).

The main objective of this chapter is to introduce a methodology for the investigation of the statistical distribution of momentum and mass transfer under the fore-mentioned conditions of interested collisions between spray droplets and flowing particles. The cases discussed here serve as the preliminary demonstration of the approach, with the understanding that the statistical characterization of liquid attachment and momentum transfer may also depend on other influential

factors such as the nozzle spray properties (e.g., droplet size, number density and velocity distributions), the transport and material properties of flowing particles, the measurement techniques employed, and the physical complicities in the Lagrangian models used for data interpretation.

2.2 Theoretical Basis

2.2.1 Basic Logics

In order to study the spray-collision-based wetting of particles, consider a simple case of collisions between a group of free-fall particles and a horizontal high-speed spray of liquid. Assume that there is a series of collecting bins along the spray jetting or penetration so that all particles and droplets can be collected by their gravity-inertia-driven sedimentation. The collected mass in each bin includes a combined mass of liquid and particles, contributed by various transport mechanisms including, but not limited to, the jet-deflected particles and droplets, collision-scattered droplets (daughter droplets) and particles, and collision-wetted particles by liquid attachment. The key issue is to find a method that can separate these individual contributions from the measurements of combined effect.

To quantify the various resources that contribute to the collected liquid and particles, it is desired to run a set of separate experiments with each one of them only contributing to or adding an individual contribution once a time under the same or very similar conditions. Specifically, to estimate the contribution of particles blown off by the gaseous jet, an experiment with the free-fall particles passing a gas jet without liquid spray is performed. Then, to estimate the contribution of droplets by the spray jet without collisions, a separate experiment of a spray jet without free-fall particles is conducted. Next, to estimate the contribution of droplets scattering without particle wetting, another experiment of a spray jet with free-fall hydrophobic particles is carried out, which has a combined result of all

contributions except for the particle wetting or liquid attachment. Finally, to obtain the contribution of liquid-attachment on wetted particles, an experiment of a spray jet with free-fall hydrophilic particles is investigated, which has a combined result of all contributions. Thus, with the assistance of above individual experiments, logically and conceptually, the individual mechanistic contributions towards the measurements of droplets and particles along the jet penetration can be separated, and hence the needed information on liquid attachment as well as statistical collision characteristics is obtain. Above logics in the experiment design clearly ignore the coupling effects among these individual experiments. Hence, the current proposed method should be regarded as the first-order approach.

2.2.2 After-collision Velocity and Sedimentation Trajectory

To study the statistical collision characteristics on momentum transfer between colliding parties, one must investigate the changes in velocity after the collision. It is realized that the after-collision velocity of a droplet or a particle can be indirectly estimated from the particle sedimentation trajectory or its sedimentation location in the collection bin, which can be calculated using a corresponding deterministic trajectory model and assuming no further collisions along this trajectory.

The binary collisions between free-falling particles and a horizontal liquid spray jet are schematically depicted in Figure 2.1, where the settling particles are described, approximately, by a two-zone representation: one zone of a dense-particle layer and the other zone of dilute dispersed particles. There are two coordinate systems introduced for the convenience of the modeling. A cylindrical coordinate system for gaseous round-nozzle jet where the gravity effect is neglected with the comparison to the jet momentum, whereas the Cartesian coordinates are used for the trajectory modeling of gravity-inertia settling of particles or droplets.

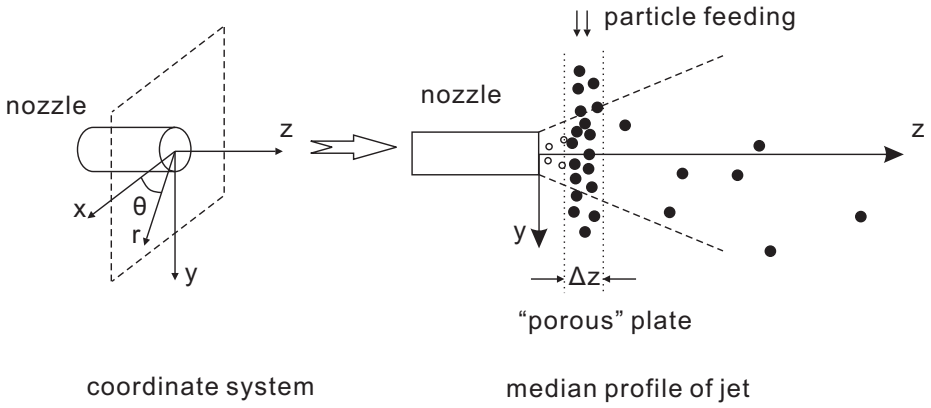

Figure 2.1 Coordinate systems and zones of moving particles.

Lagrangian trajectory equation with gas-particle interactions In particle-droplet collisions resulting particle wetting, the after-collision droplets consist of two basic groups: one attached and the other scattered. The attached liquid joins the colliding party, forming a larger and wet particle; whereas the scattered droplets are treated in the same way as scattered in non-wetted collisions. Thus, given the initial droplet or particle size, the collision probability statistics can be obtained in terms of after-collision velocities analyzed from collected mass distribution by a series of bins along the jet penetration. This collision probability statistics reflect the statistical nature of the non-deterministic properties such as the collision modes (center-to-center or off-center or oblique) and/or droplet size and its jetting velocity. For simplicity, in the deterministic trajectory model introduced below, only the drag force and the gravitational force are considered. Thus, the after-collision trajectory of a sphere (wetted particle, dry particle or scattered droplet) can be described in general by

$$\frac{d^2\mathbf{X_s}}{dt^2} = \frac{\mathbf{F_{D,s}}}{m_s} + \mathbf{g} \tag{2.1}$$

where $\mathbf{X_s}$ is the position vector of traced particles; the subscript s stands for colliding species (droplets, dry particles or wet particles); $\mathbf{g}$ is the gravitational force, and

$\mathbf{F_{D,s}}$ is the drag force due to the relative movement to the gas phase, which can be expressed as,

$$\mathbf{F_{D,s}} = C_{D,s}\rho_g \frac{\pi d_s^2}{8}\left(\mathbf{U_g} - \frac{d\mathbf{X_s}}{dt}\right)\cdot\left|\mathbf{U_g} - \frac{d\mathbf{X_s}}{dt}\right| \tag{2.2}$$

where $\mathbf{U_g} = \mathbf{U_g}(z, r)$is the local gas velocity. For a round-nozzle gas jet, the axial velocity $U_{g,z}$ distribution in the fully-developed region can be approximated by [1]:

$$U_{g,z} = \begin{cases} \left(\sqrt{\frac{15}{8}}\frac{U_j \cdot d_j}{0.22z}\right)\left[1 - \left(\frac{r}{0.22z}\right)^{3/2}\right]^2 & r \le 0.22z \\ 0 & r > 0.22z \end{cases} \tag{2.3}$$

where U_j and d_j are jet velocity and diameter at the nozzle outlet. The radial velocity of gas can be estimated by the continuity equation as

$$\frac{\partial U_{g.z}}{\partial z} + \frac{1}{r}\frac{\partial (rU_{g,r})}{\partial r} = 0 \tag{2.4}$$

However, since $U_{g,z} \gg U_{g,r}$, it is assumed $U_{g,r} = 0$ for simplicity. It should also be pointed out that Equation (2.3) is obtained assuming the conservation of jet momentum without any external forces. When a significant amount of particles interact with the jet flow, the gas jet velocity could be damped and altered by the dense flowing particles in the jet region. The particle damping may be roughly accounted by balancing the pressure drop required for gas to pass through this porous media against the equivalent pressure drop that would be caused by the jet momentum decrease over the same region. With the assumption that the variation of flow cross-section area over this porous media zone can be neglected, as depicted in Figure 2.1, the modified equation for the gaseous jet flow in the zone of dense particle layer is expressed as:

$$\frac{d}{dz}(\alpha\rho U_g^2) = -150\frac{(1-\alpha)^2}{\alpha^3}\frac{\mu U_g}{d_p^2} - 1.75\frac{1-\alpha}{\alpha^3}\frac{\rho U_g^2}{d_p} \tag{2.5}$$

The right hand side of the above equation is based on the Ergun equation [18]. The gas volume fraction indicates the particle volume density in the jet region, which is then determined with the particle dispersion along the jet. In this study, it is noticed that only a small fraction of particles is deflected or dispersed by the spray jet while the most of particles retaining their course of free fall. Hence, it is assumed that the gas volume fraction remains constant over the jet-collision region and then the flow becomes very dilute. For a liquid spray jet, it is further assumed that the gas velocity distribution in the fully-developed region is unaltered by the presence of droplets.

Partition of mass and momentum in a partially-wet collision Consider a partially-wet collision between a droplet and a particle, as shown in Figure 2.2. Upon the collision, the droplet will break up into two parts, one is attached to the particle surface due to mass transfer (Δm_d) and the other part will move forwards with a different momentum.

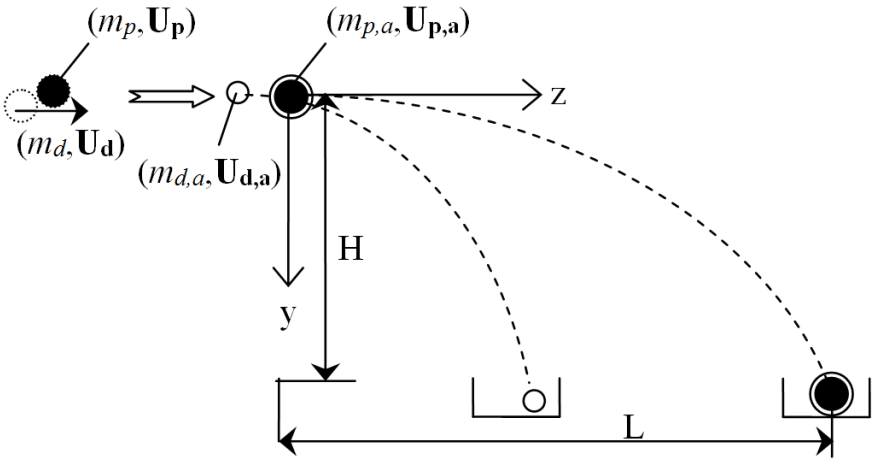

Figure 2.2 Mass and momentum transfer upon a droplet-particle binary collision.

The momentum transfer by collision can be divided into two parts: momentum transferred due to mass transfer ($U_d \Delta m_d$) and additional momentum transfer (ΔM_{dp}). The resulted characteristic parameters of wetted particle can be written as:

Mass:

$$m_{p,a} = m_p + \Delta m_d \tag{2.6}$$

Diameter:

$$d_{p,a} = \sqrt[3]{d_p^3 + \frac{6}{\pi}\frac{\Delta m_d}{\rho_d}} \tag{2.7}$$

Density:

$$\rho_{p,a} = \frac{m_p + \Delta m_d}{\frac{\pi}{6} d_p^3 + \frac{\Delta m_d}{\rho_d}} \tag{2.8}$$

Velocity:

$$\mathbf{U_{p,}}_a = \frac{\mathbf{U_d}\Delta m_d + \mathbf{\Delta M_{dp}}}{m_p + \Delta m_d} \tag{2.9}$$

By substituting Equation 2.2 into Equation 2.1 and decoupling the vector form, the governing equations of particle velocity along y and z-direction is obtained as:

$$\begin{cases} \dfrac{dU_{y,s}}{dt} = g \\ \dfrac{dU_{z,s}}{dt} = \dfrac{C_{D,s}\rho_g \frac{\pi d_s^2}{8} \left(U_{g,z} - U_{z,s}\right) \left|U_{g,z} - U_{z,s}\right|}{m_s} \\ \dfrac{dz}{dt} = U_{z,s} \\ \dfrac{dy}{dt} = U_{y,s} \end{cases} \tag{2.10}$$

The drag coefficient, $C_{D,s}$, of a spherical particle is a function of the particle Reynolds number ($Re_p = |U_p - U_g| d_p \rho / \mu$):

$$C_{D,s} = \begin{cases} \dfrac{24}{\mathrm{Re}_p} & \mathrm{Re}_p < 2 \\ 0.4 + \dfrac{24}{\mathrm{Re}_p} & 2 < \mathrm{Re}_p < 500 \\ 0.44 & 500 < \mathrm{Re}_p < 2 \times 10^5 \end{cases} \tag{2.11}$$

There are four time-dependent unknowns ($U_{z,s}$, U_y,s, z, y) and four independent equations, so the problem is closed and solvable. With a given set of initial conditions, by tracking the time, the corresponding particle trajectory can be obtained. From the vertical location H (when $y = H$), the particle settling location L is then determined. Thus, the initial velocity of a given particle can be correlated to the bin location, or vice versa.

The above model leads to the relationship among the location of collection bin $z(L, H)$, the size and density of s-particle, and velocity of after-collision particle, which can be expressed in general as:

$$f\left(d_s, \rho_s, U_{z,s}, z(L, H)\right) = 0 \tag{2.12}$$

In summary, when a collection bin located at $z(L, H)$ collects the wetted particles, one can easily determine the mass by simply weighing the collected particles and decoupling other scattered droplet and particles, which will be explained in detail at Section 2.3. Then, based on Equation 2.12, the after-collision velocity of the wetted particle can be further determined. Repeating such an approach to the entire series of collection bins along the spray penetration will yield the desired statistics of particle wetting, momentum transfer and other collision-based parameters in terms of the after-collision velocity or penetration length. A similar procedure of above analysis can also be applied for gas jet dispersion of non-wetted particles or droplets.

2.2.3 Liquid Attachment and pdf of Particle Collision

As outlined in Section 2.2.1, based on the four different sets of experiments under the same but one conditions, conceptually the individual contributions of liquid and particles to the bin collections along the spray penetration can be separated. These individual contributions are, respectively, from the jet deflection of dry particles, spray inertia settling of droplets, scattering of dry particles from non-wetted collisions, scattering of droplets from non-wetted collisions or scattering of daughter-droplets from partially-wetted collisions. In quantifications of above separations of measurements, the simplest approach is to assume that the total collected liquid and particles are additive linearly according to the various mechanistic contributions, which ignores the coupling effects among these mechanisms. This simple method is adopted as the first-order approach in this study at current status.

Determination of individual mass contributions in a collection bin For the spray collision experiment with hydrophilic particles, the total mass of liquid by collision in each bin includes attached, scattered and non-collided droplets. Hence, the mass of collision liquid (attached and scattered) for i^{th} bin can be expressed below:

$$m_{d,attached+scattered,i} = m_{d,total,i} - m_{d,non-collided,i} \tag{2.13}$$

In order to estimate the mass contribution by non-collided droplets, $m_{d,non-collided,i}$, from the particle-free spray jet experiment, it is assumed that for each bin, the mass ratio of collected non-colliding droplets to that would-be-collected in the particle-free spray jet is the same as the mass ratio of all collected non-colliding droplets to the total droplets of the spray. Thus,

$$m_{d,non-collided,i} = \left(\frac{\sum_{i=1}^{n} m_{d,total,i} - \sum_{i=1}^{n} m_{d,attached+scattered,i}}{\sum_{i=1}^{n} m_{d,total,i}} \right) m_{d,sprayed,i} \tag{2.14}$$

where $m_{d,sprayed,i}$ stands for the gravity-settled droplets from the particle-free spray jet under the same experimental conditions. It should be pointed out that Equations 2.13 and 2.14 need to be solved together for the two coupled unknowns, i.e. $m_{d,non-collided,i}$ and $m_{d,attached+scattered,i}$. Alternatively, they can also be solved using the iterative method.

Similarly, the total mass of particles by collision in each bin also includes both the particles of collisions (either wetted or scattered) and the particles deflected by gas jet. Therefore, the mass of collision particles for i^{th} bin can be expressed as:

$$m_{p,collided,i} = m_{p,total,i} - m_{p,non-collided,i} \tag{2.15}$$

In order to estimate $m_{p,non-collided,i}$, it is assumed that, for each bin, the relative mass distribution of the non-colliding particles to that of the total particle collected is the same as the relative mass distributions of particles by the droplet-free gas jet, i.e.,

$$\frac{m_{p,non-collided,i}}{\sum_{i=1}^{n} m_{p,total,i}} = \frac{m_{p,deflected,i}}{\sum_{i=1}^{n} m_{p,deflected,i}} \tag{2.16}$$

The number of particles of collision for i^{th} bin is thus given by

$$N_{p,collided,i} = \frac{m_{p,collided,i}}{m_p} \tag{2.17}$$

where m_p is the averaged mass of a single particle.

The scattering effect is analyzed by the aid of the experiment of spray collisions with hydrophobic particles, whose parameters are marked by adding prime ($'$) compared to those of hydrophilic particles. The collected mass of collision-scattered liquid for i^{th} bin can be expressed as:

$$m'_{d,scattered,i} = m'_{d,total,i} - m'_{d,non-collided,i} \tag{2.18}$$

where $m'_{d,scattered,i}$ is estimated in a similar way to the case of collisions with hydrophilic particles by:

$$m'_{d,non-collided,i} = \left(\frac{\sum_{i=1}^{n} m'_{d,total,i} - \sum_{i=1}^{n} m'_{d,scattered,i}}{\sum_{i=1}^{n} m'_{d,total,i}} \right) m_{d,sprayed,i} \tag{2.19}$$

Similarly, Equations 2.18 and 2.19 need to be solved together for the two coupled unknowns, i.e. $m'_{d,non-collided,i}$ and $m'_{d,scattered,i}$. The mass of scattered particles for i^{th} bin can also be assessed by:

$$m'_{p,collided,i} = m'_{p,total,i} - m'_{p,non-collided,i} \tag{2.20}$$

Conceptually, the mass contribution of non-collided hydrophobic particles should be very similar, if not exactly identical, to that for the hydrophilic particles since both particles share otherwise the same geometric and physical properties, namely,

$$\frac{m'_{p,non-collided,i}}{\sum_{i=1}^{n} m'_{p,total,i}} = \frac{m_{p,non-collided,i}}{\sum_{i=1}^{n} m_{p,total,i}} \tag{2.21}$$

The number of particles of non-wetted collision for i^{th} bin is determined by

$$N'_{p,collided,i} = \frac{m'_{p,collided,i}}{m_p} \tag{2.22}$$

Based on the $m_{d,attached+scattered,i}$ solved from Equation 2.13, the mass of attached liquid can be deduced as,

$$m_{d,attached,i} = m_{d,attached+scattered,i} - m_{d,scattered,i} \tag{2.23}$$

However, it is realized that scattered mass of droplet is different between hydrophobic collisions and hydrophilic collisions. In order to estimate scattered mass of droplet in a hydrophilic collision from the information of hydrophobic collisions, it is further assumed that the mass ratio of scattered droplets in a hydrophilic collision to that in a hydrophobic collision is the same that mass ratio of collided particles in a hydrophilic collision to that in a hydrophobic collision , namely

$$m_{d,scattered,i} = {m'}_{d,scattered,i} \left(\frac{m_{p,collided,i}}{{m'}_{p,collided,i}} \right) \tag{2.24}$$

Thus, Equations 2.23 and 2.24 lead to the final equation for the estimation of liquid attached in a hydrophilic collision as

$$m_{d,attached,i} = m_{d,attached+scattered,i} - {m'}_{d,scattered,i} \left(\frac{m_{p,collided,i}}{{m'}_{p,collided,i}} \right) \tag{2.25}$$

Consequently, the film thickness (δ) of attached liquid for i^{th} bin on each wetted particle can be calculated, by assuming $\delta \ll d_p$, as

$$\delta_i = \frac{m_{d,attached,i}}{N_{p,collided,i}} \cdot \frac{1}{\rho_d \pi d_p^2} \tag{2.26}$$

where ρ_d is the liquid density.

In summary, there are 11 unknowns to be determined: δ_i, $m_{d,attached,i}$, $m_{d,attached+scattered,i}$, $m_{d,scattered,i}$, $m_{p,collided,i}$, ${m'}_{p,collided,i}$, $N_{p,collided,i}$, $m_{d,non-collided,i}$, $m_{p,non-collided,i}$, ${m'}_{d,non-collided,i}$, ${m'}_{p,non-collided,i}$. These 11 unknowns can be coupling

solved by 11 independent equations (Equations 2.13 to 2.21, 2.25, and 2.26). To solve those 11 equations, six parameter ($m_{d,total,i}$, $m'_{d,total,i}$, $m_{p,total,i}$, $m'_{p,total,i}$, $m_{d,sprayed,i}$, and $m_{p,deflected,i}$ are necessary to be known from experiments (see Section 2.3). Detailed step-by-step data analysis is explained below in Figure 2.3.

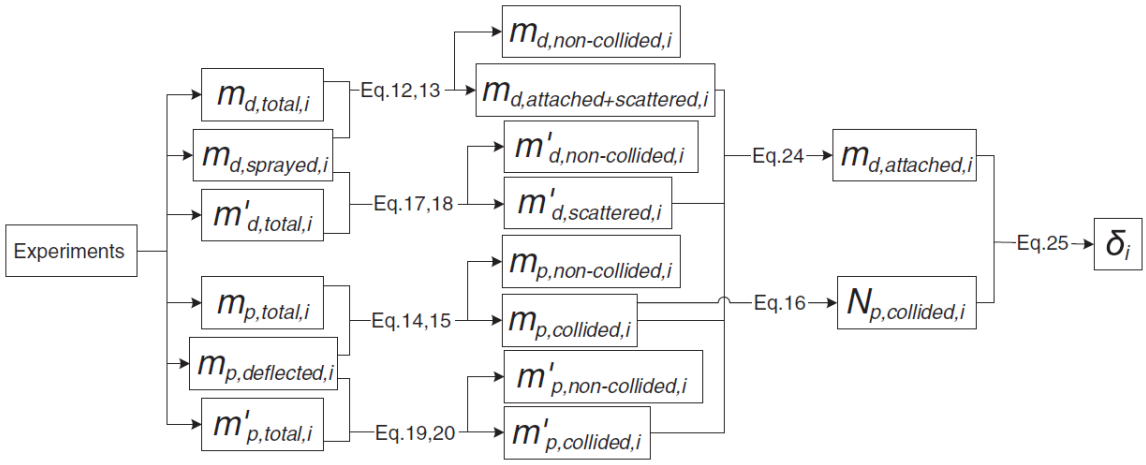

Figure 2.3 Logics chart of data analysis.

Determination of probability density function and momentum transfer

The probability density function of particle collision in the i^{th} bin can be calculated as:

$$f_i(U) = \frac{m_{p,collided,i}}{\sum_{i=1}^{n} m_{p,collided,i}} \cdot \frac{1}{U_{\max,i} - U_{\min,i}} \tag{2.27}$$

where $U_{\max,i}$ and $U_{\min,i}$ are the limiting bounds of after-collision velocities of particles that would be collected by the i^{th} bin. The after-collision velocity is calculated from the deterministic trajectory model introduced in Section 2.2. It is noted that the normalization condition is satisfied automatically from

$$\int_0^{\infty} f(U)dU = \sum_{i=1}^{n} f_i \Delta U_i = \sum_{i=1}^{n} \left(\frac{m_{p,collided,i}}{\sum_{i=1}^{n} m_{p,collided,i}} \right) = 1 \tag{2.28}$$

The deterministic trajectory model dictates the unique correspondence between locations of particles or droplets collected and their initial velocity (after-collision velocity), provided that the gas flow field can be predetermined and un-interfered in the presentation of the traveling particles or droplets. Since the particles are in a free-fall status before colliding with a horizontal spray jet, it would be reasonable to assume the horizontal component of before-collision velocity of all falling particles to be zero (assuming the gas-blowing effects are only for the non-collision deflected particles). Therefore, the after-collision velocity actually becomes the direct indicator of the momentum transfer of collisions between a colliding pair of a particle and a droplet. Consequently the statistic distribution of this momentum transfer along the spray region could be interpreted as the probability of momentum transfer of particles by spray collisions.

Ignored influential factors While the above theoretical analysis covers major mechanisms that govern the mass collection in the bins, there are some mechanisms that are ignored in the modeling or analysis, either due to the secondary importance or due to their complicities whose modeling quantification is beyond the reality at the current stage.

First of all, the spray jet is turbulent with wide distributions of droplet size and droplet velocity. The effects of turbulence, size distribution and initial velocity distributions of droplets are all ignored for simplicity. The neglect of turbulent diffusion and fluctuations is essential to the adoption of the simple deterministic trajectory model. The effect of droplet size, however, is not directly relevant to the measurement and data interpretation, while it could be important for further collision characteristics analysis. Further, the possibility of multiple collisions of the same particle during its passing through the spray region is omitted. The detailed

accounts of above discussed minor mechanistic contributions may need to be assessed or addressed in future studies.

2.3 Experimental Approach and Validation Method

2.3.1 Experimental Setup

The schematic diagram of experimental setup is shown in Figure 2.4, which is designed to investigate the statistic distribution of mass and momentum transfer during the collision between free-releasing particles and horizontal water spray jet. The entire setup consists of four major sub-systems, namely, the particle-feeding system, the jet spray system, the sample collection system (from the top view of the chamber, as illustrated in Figure 2.5), and the data analysis system.

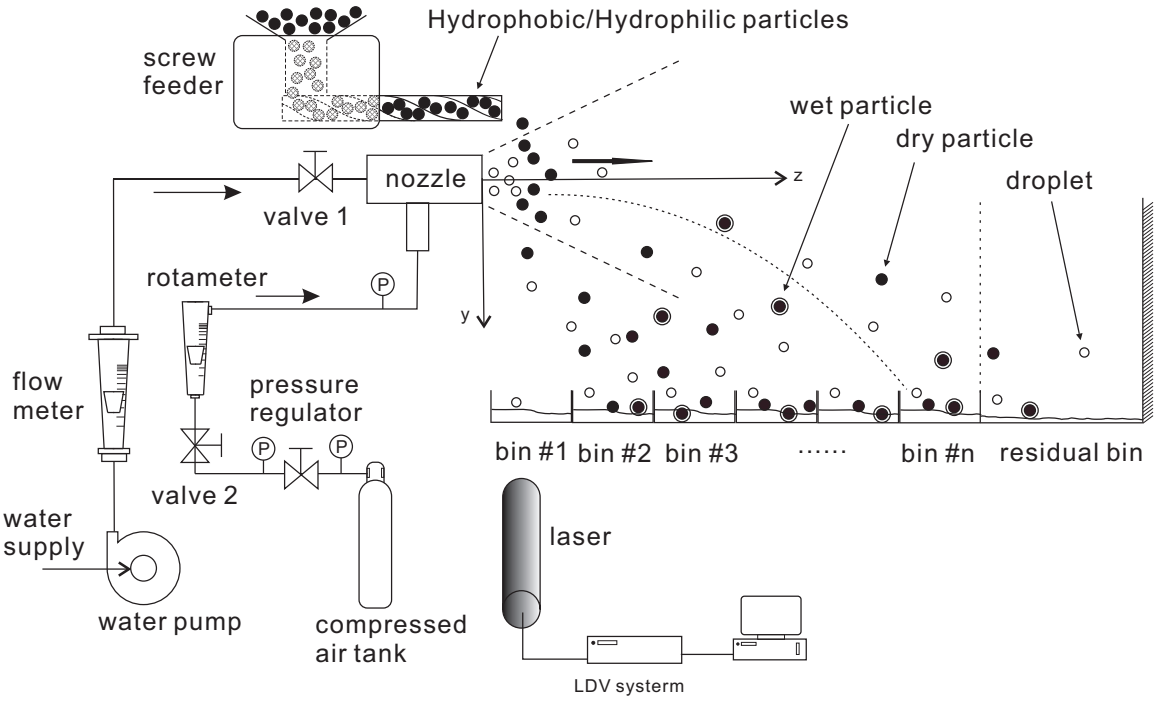

Figure 2.4 Schematic diagram of experimental system.

The particles are glass beads from MO-SCI Specialty Products. The average size of each particle is 2.1 ± 0.4 mm (GL0191SB1700-2500SC / GL0191SB1700-2500). There are two types of glass beads: one is hydrophilic and the other is hydrophobic.

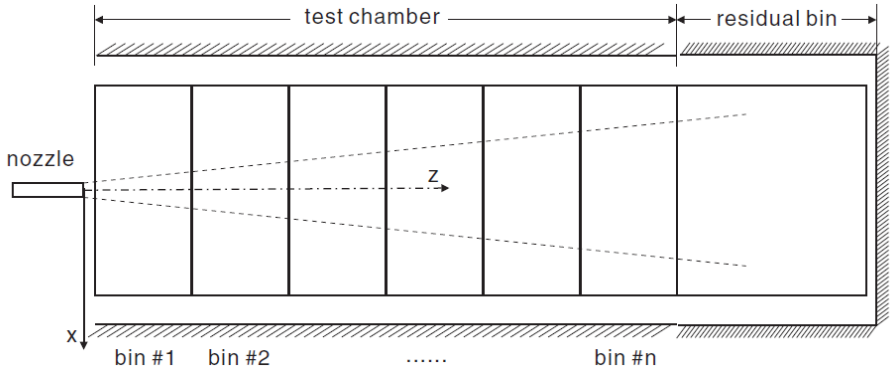

Figure 2.5 Top view of serial bins and open top/end chamber.

The particles are fed via a screw feeder [AccuRate] whose outlet is located right above the spray nozzle. When there are concerns of the particle attrition or fragmentation of fragile particles such as activated carbons, the screw feeder may be replaced by a simple hopper. The water-air spray jet is generated using a CANMET pilot nozzle with an openness of 3.3 mm [9]. The pressurized water and air are supplied by a booster pump (Dayton, model 2PC320) and a compressed air tank, with the flow rates and pressures accurately controlled by the flow meters and pressure regulators. The spray jet is injected horizontally into an open-top and open-ended rectangular chamber ($2500mm \times 300mm \times 600mm$), as shown in Figure 2.5. The initial injection velocity of droplets from the nozzle spray can be determined by use of a Laser Doppler Velocimetry (Dantec, BSA Flow 1.6). The volume fraction of liquid dj and the initial jetting velocity U_j are solved from the following equations of continuity, which are linked to the feeding rates of liquids and jetting gas:

$$\alpha_{dj} U_{dj} \cdot \frac{\pi}{4} d_j^2 = Q_d \tag{2.29}$$

$$\left(1 - \alpha_{dj}\right) U_j \cdot \frac{\pi}{4} d_j^2 = \left(\frac{p_{rotameter}}{p_{ambient}}\right) Q_g \tag{2.30}$$

The gas jet velocity is also measured by LDV by releasing fine tracers into the droplet-free jet region. The air volume flow rate can be calculated and compared

to that shown on rotameter (which is under pressure), and then the compression ratio $\left(\frac{p_{rotameter}}{p_{ambient}}\right)$ in Equation 2.30 can be obtained. It may be noted that, when the calculated jetting velocity of gas is close to that of speed of sound, a correction factor for compressibility shall be included into Equation 2.29. A series of collection bins ($80mm \times 80mm \times 240mm$) are arranged continuously, without any gaps between the two neighboring bins, along the horizontal penetration direction of the spray jet at the bottom of the chamber to collect the scattered, wetted or deflected particles and droplets. An extended collection section, known as residual bin, is attached to the end of the open-ended rectangular chamber to collect all the residue liquids and particles, if any. The vertical distance from nozzle outlet to the bottom of bin is 0.35 m. To minimize the measurement error, the collection bins are pre-covered by a protection plate and become only uncovered during the sampling period. The collected mass (particles with water) in each bin is weighted by a scale with an accuracy of 0.01 g (Scout Pro, Model SP402). Particles will be weighted again after they are completely dried in an electric oven (Hamilton Beach, Model 31507R).

2.3.2 Experimental Procedures and Operational Conditions

As previously stated, the collected particles are a combination of wet particles, scattered particles due to non-wetting collision with droplets and entrained particles due to gas-particle drag from the high speed jet. A series of sub-experiments are designed to separate the portions of collected particles and liquid due to different contributing mechanisms. The determinants and required types of jet, spray and particles in these individual experiments are tabulated in Table 2.1.

The detailed operational conditions for the experiments are listed in Table 2.2. During the experiment, the variation of air-to-liquid ratio is realized by adjusting the averaged air flow rate from 20 ± 5 to 40 ± 15 CFH under the same pressure. The gas feed rate is measured by a rotameter (Dwyer, 100 SCFH AIR). The reading of

Table 2.1 Determinants and Requirements of Individual Experiments

Experiment	Particle type	Spray type	Determined term
1	Either	Air jet	$m_{p,deflected,i}$
2	No	Spray jet	$m_{d,sprayed,i}$
3	Hydrophobic	Spray jet	$m'_{d,total,i}$, $m'_{p,total,i}$
4	Hydrophilic	Spray jet	$m_{d,total,i}$, $m_{p,total,i}$

Table 2.2 Operational Conditions

Case No.	Glass beads diameter (mm)	Gas feed rate (SCFH)	Water flow rate (GPM)
1	2.1 ± 0.4	60	1.0 ± 0.2
2	2.1 ± 0.4	70	1.0 ± 0.2

gas feed rate before the gas-liquid spray nozzle can be fluctuated up and down. An averaged reading is taken with the fluctuation range (See Table 2.2). The water flow rate, measured by a ball flow indicator, is kept at constant of 1.0 ± 0.2 GPM. The pressure in the nozzle is set as of 110 PSIG by a pressurized air tank. The air flow rates at standard condition (SCFH) have been calibrated separately against readings of the flow rate at pressurized conditions, which is equivalent to a range from around 60 to 70 SCFH.

2.4 Exemplified Results and Discussions

Two different cases (two gas-feed loads) were investigated in this study, with experimental conditions listed in Table 2.2. For each case, four sub-experiments were conducted to separate the mass contributions of individual mechanisms, as outlined in Table 2.1. For each sub-experiment, a series of liquid-particle mixtures can be collected by the collecting bins along the trajectory of spray jet. The momentum

transfer and the particle collision statistics can then be analyzed by methodology and equations described in Section 2.2.2.

2.4.1 Individual Contributions to the Mass Collection

First of all, the individual contributions to the collected mass in each bin must be separated in order to further pursuit the data analysis. The collected mass in a bin include both particles and liquid.

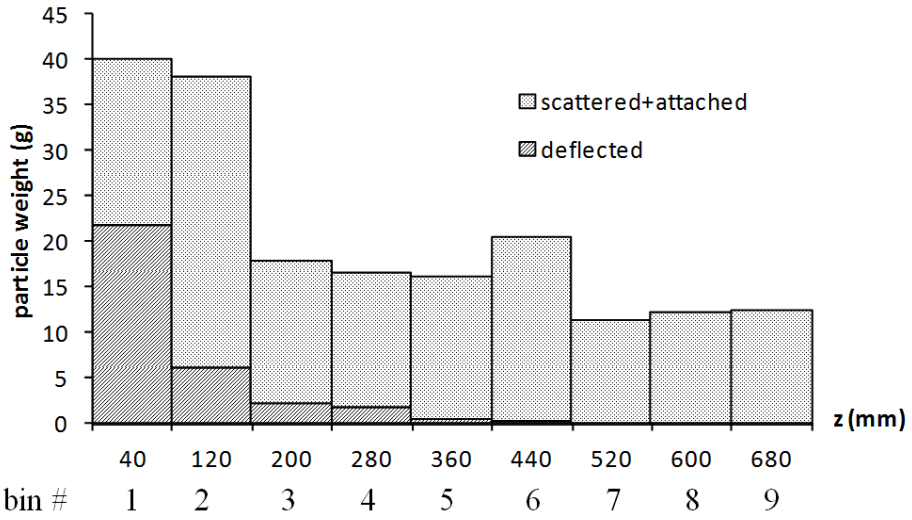

Figure 2.6 Individual contributions to the particle mass distribution (Case 2 in Table 2.2): Hydrophilic particles.

Similar to the case for particles, the collected liquid in a bin is also a combination of various individual contributions, including the liquid attached to particles, scattered droplets due to non-wetting collision, and the gravity settling of non-collision droplets of spray jet. Experiments 2, 3 and 4 of Table 2.1 are operated to separate these individual contributions, with the aid of Equations 2.13, 2.14, 2.18, and 2.19. Figure 2.8 shows an example of the individual contributions to the liquid distributions along the spray penetration direction (Case 2 in Table 2.2). It can be seen that there is a significant contribution of the gravity settling (non-collided) droplets, compared to the other contributions in this example.

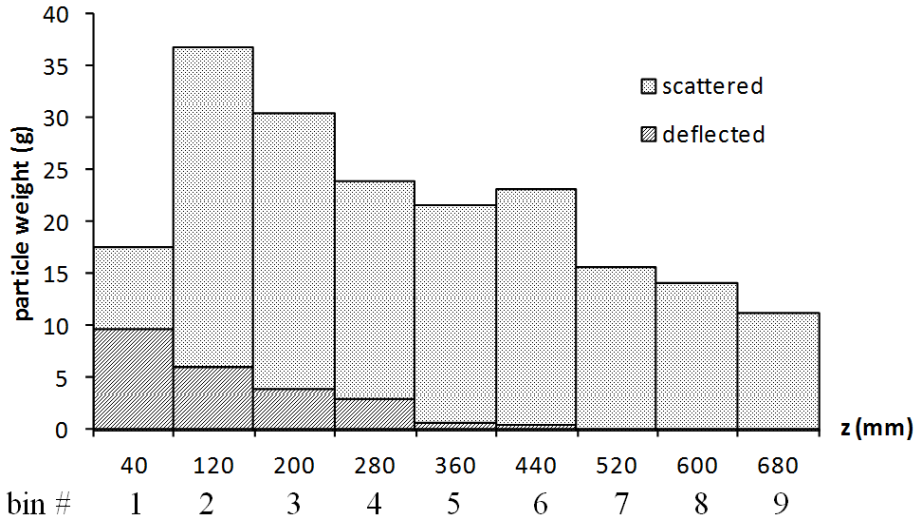

Figure 2.7 Individual contributions to the particle mass distribution (Case 2 in Table 2.2): Hydrophobic particles.

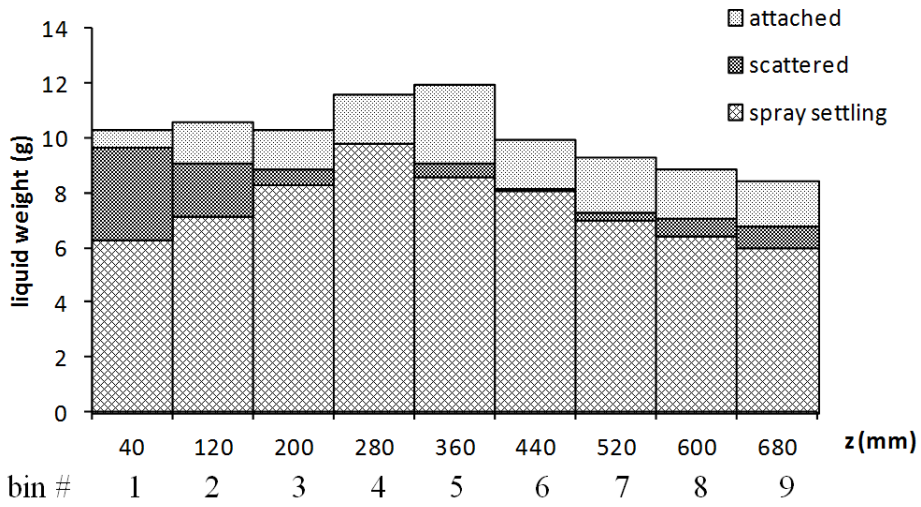

Figure 2.8 Liquid decoupling (Case 2).

2.4.2 Collision Probability

From the amount and collection position of separated mass contributions of particles and droplets, the after-collision velocity could be traced back by the deterministic Lagrangian trajectory model presented in Section 2.2.2. Specifically, after-collision velocity of a particle or droplet can be obtained by solving Equation 2.10. Thus, from the above mass distribution of liquid and particles, the collision probability density

function, statistical probabilities of mass and momentum transfer upon collision can all be obtained and analyzed.

For various cases in Table 2.2, the relationship between the after-collision velocity of interested particle or droplet and the collection location at the bottom of the chamber (where collection bins are located) is calculated and shown in Figure 2.9. For all cases investigated here, the after-collision velocity of the particles appears to follow a linear relation with the collection location along the spray penetration.

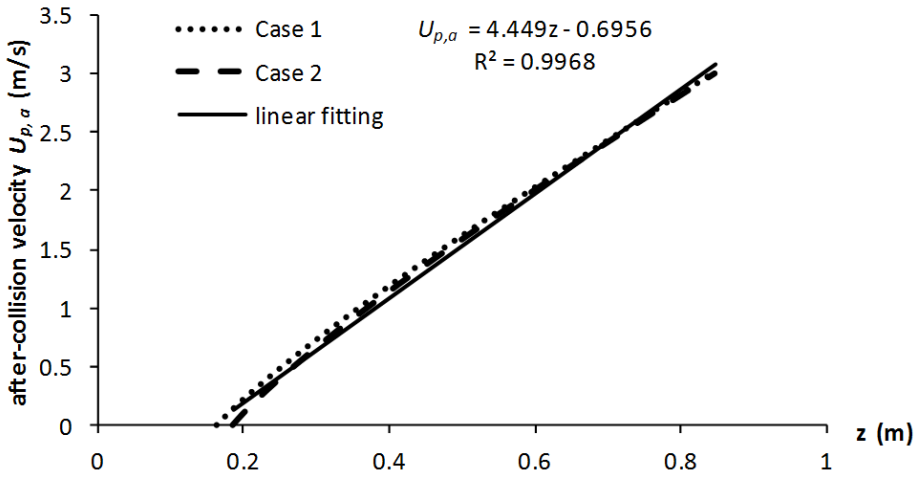

Figure 2.9 After-collision velocity with penetration length.

Now consider the bin collection location as an intermediate variable. Based on the mass distribution (Figures 2.6, 2.7 for particles or Figure 2.8 for droplets) and Figure 2.9, along with the definition of the particle-droplet collision probability density function (as defined in Equation 2.27), the particle-droplet collision probability density can be yielded, as exemplified in Figure 2.10 for Case 2 and Case 1. It should be noted that the horizontal axis in both figures is based on the ratio of the particle after-collision velocity over the gas jetting velocity. It can be seen that the collision probability is very high near the nozzle injection region or at low after-collision velocity and then decreases along with the jetting distance or after-collision velocity. For Case 1 and Case 2, most of the collisions

have the after-collision velocities between $0.002U_j$ and $0.01U_j$, comparing to the lower probability of higher after-collision velocity. This may be interpreted in the probability of collision modes, namely, the frequency of oblique collision (for less momentum transferred) between particles and droplets is very high, while the frequency gradually falls down when more momentum is transferred (such as by normal collisions). Based on the calculation with the probability density function, the averaged after-collision velocity of particles could be obtained. For example, $\frac{\bar{U}_s}{U_j} = 0.0144$ for Case 1, and $\frac{\bar{U}_s}{U_j} = 0.0152$ for Case 2.

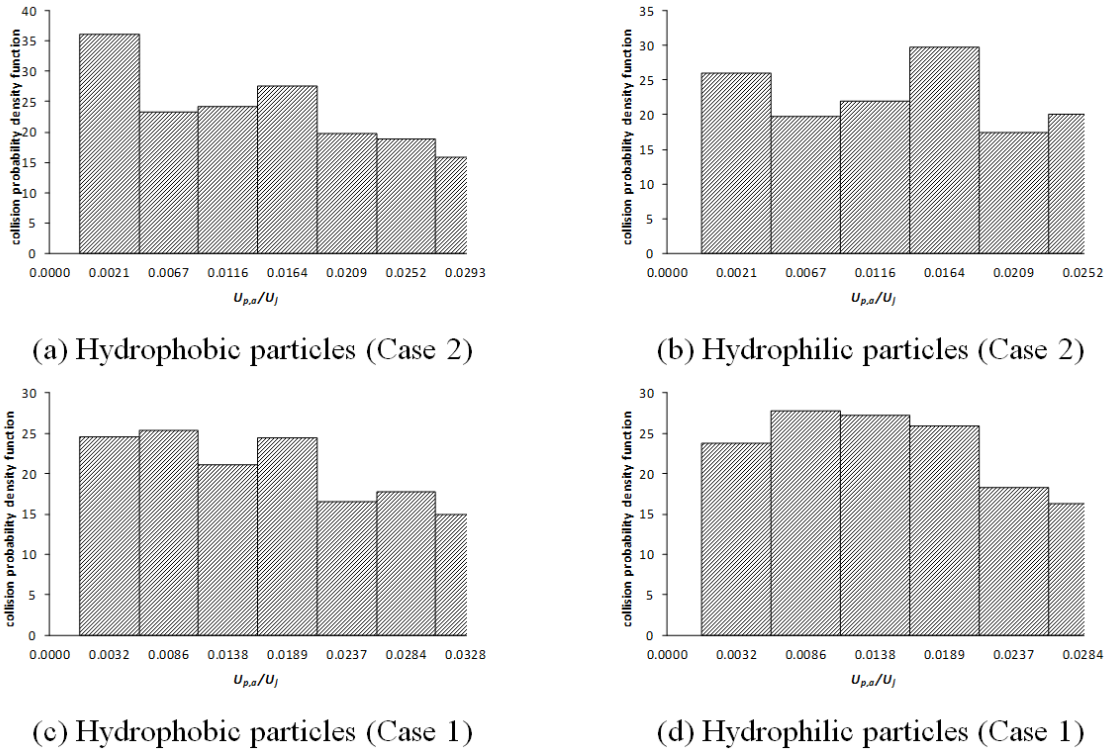

(a) Hydrophobic particles (Case 2)

(b) Hydrophilic particles (Case 2)

(c) Hydrophobic particles (Case 1)

(d) Hydrophilic particles (Case 1)

Figure 2.10 Collision probability density against after-collision velocity.

For the convenience of developing a continuous and simple model, the experimental distributions of probability density function in Figure 2.10 may be re-plotted by scattering data points, as shown in Figure 2.11.

The re-plotted distribution indicates that the particle-droplet collision probability would quickly increase to a maximum value and then decrease asymptotically

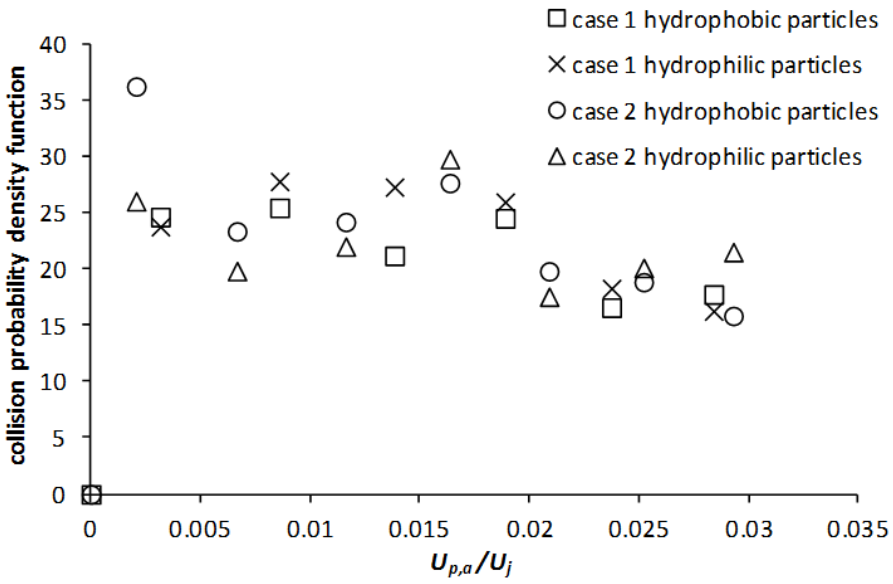

Figure 2.11 Collision pdf against after-collision velocity.

in an exponential manner with the increasing of the particle after-collision velocity. Such a trend may suggest a general two-parameter phenomenological model of pdf, as expressed by

$$y\left(a,b\right)=\frac{x^{a}\mathrm{e}^{-bx^{2}}}{\int_{0}^{\infty}x^{a}\mathrm{e}^{-bx^{2}}dx} \tag{2.31}$$

where a and b are case-adjustable coefficients. An alternative form of Equation 2.31 can be expressed in terms of x_m (relative velocity at which pdf reaches its maximum) and the characteristic bandwidth σ as

$$y\left(x_{m},\sigma\right)=\frac{x^{\frac{x_{m}^{2}}{\sigma^{2}}}\mathrm{e}^{-\frac{x^{2}}{2\sigma^{2}}}}{\int_{0}^{\infty}x^{\frac{x_{m}^{2}}{\sigma^{2}}}\mathrm{e}^{-\frac{x^{2}}{2\sigma^{2}}}dx} \tag{2.32}$$

It can be shown that $b=1/(2\sigma^{2})$, $a=2bx_{m}^{2}$. For the least-square curve fitting of Figure 2.11 with Equation 2.32, the rough range of x_m is about 0.007 whereas σ is around 0.024, respectively. The corresponding curves of Equation 2.32 with the typical x_m and σ are exemplified in Figure 2.12.

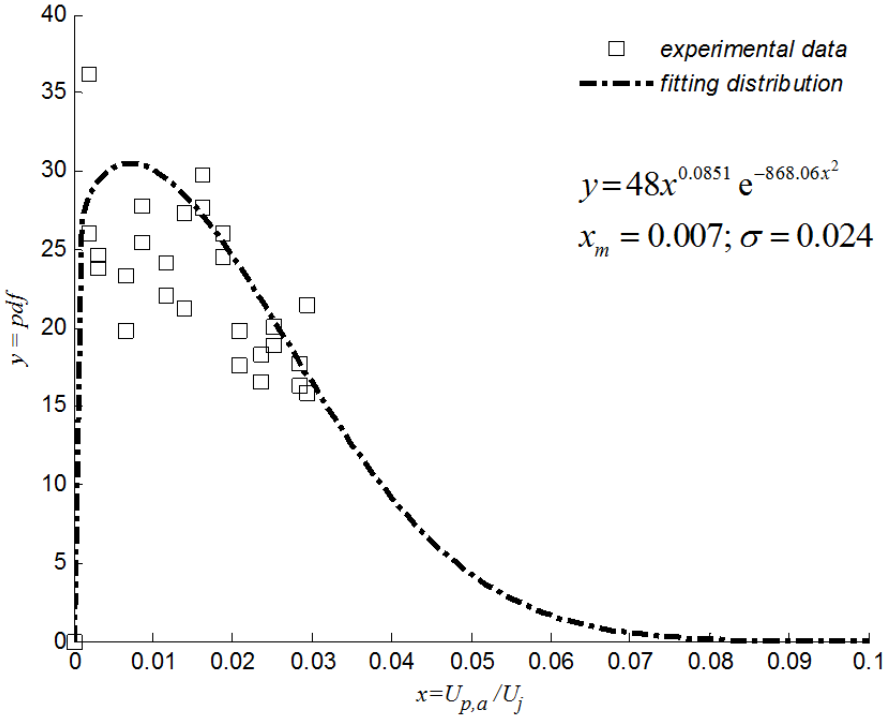

Figure 2.12 Corresponding curves of Equation 2.32.

2.4.3 Liquid Attachment Statistics

One of the main objectives of the study is to determine statistically averaged liquid attachment on each hydrophilic particle. As described in Section 2.2 and Equation 2.26, by separating the combined measurement (spray, deflection and scattering collisions), the thickness of liquid attachment on particles (mass transferred) could be calculated in terms of the ratio of after-collision velocity over jet velocity, as shown in Figure 2.13. The thickness of liquid attachment on an averaged hydrophilic particle for Case 1 is within the range of 1% to 4% of the particle diameter; whereas for Case 2 the thickness varies from 4% to 8% of particle diameter. This suggests that a higher gas flow rate is likely to generate a thicker coating than that from a lower gas flow rate.

The thickness of attachment can also be expressed against the collision probability, as shown in Figure 2.14, which shows that it is more probable of thinner

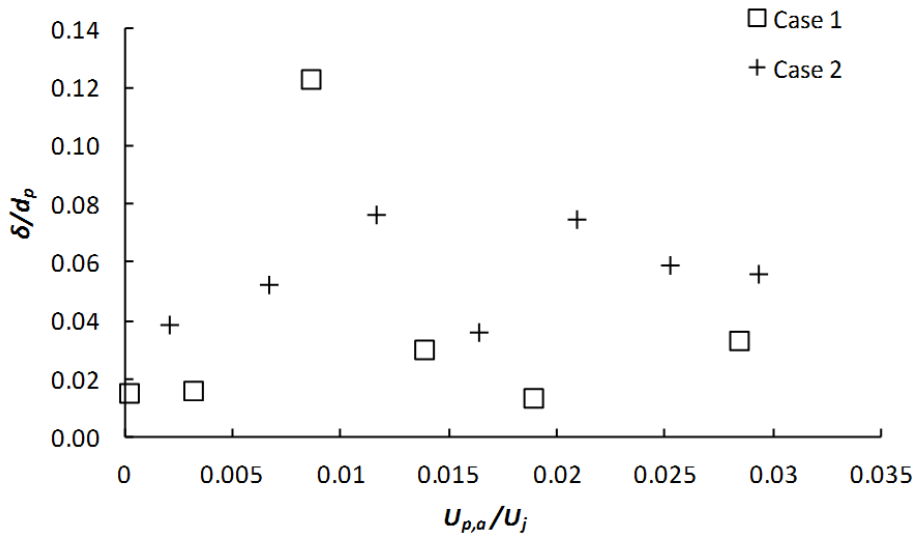

Figure 2.13 Coating thickness against after-collision velocity.

attachment than thicker. The thickness is less than 8% of particle diameter for the case studied. Based on the calculation with the probability density function, the averaged thickness could be found. For instance, $\frac{\bar{\delta}}{d_p} = 0.021$ for Case 1, whereas $\frac{\bar{\delta}}{d_p} = 0.046$ for Case 2.

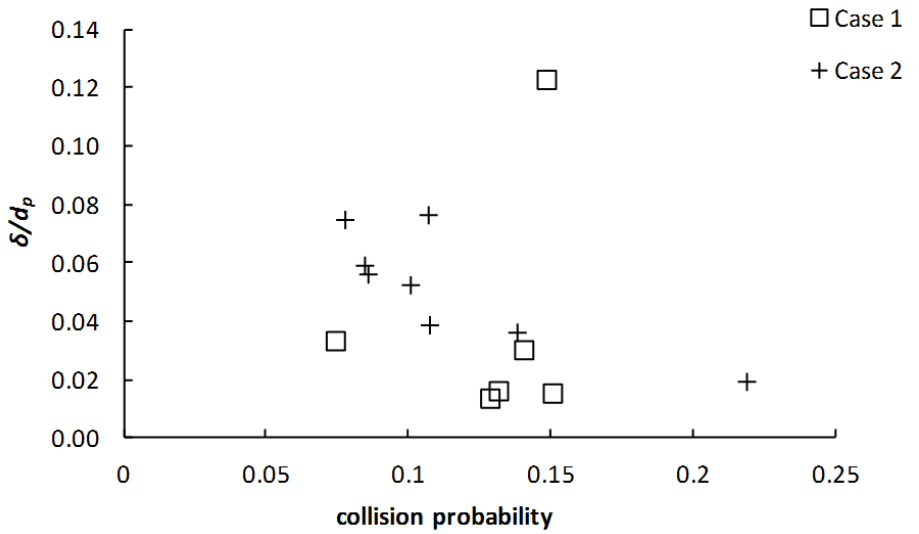

Figure 2.14 Coating thickness against collision probability.

2.5 Relevance to Other Chapters

This chapter focused on the statistical study of spray impingement caused solids wetting (liquid attachment) and collision probability distributions along the spray trajectory. This information is essential to the modeling work of spray feed penetration into gas-solid flow. The liquid spray transportation and vaporization in the feed zone is predominantly affected by the solid-droplet collision induced heat, mass and momentum transfer. This statistical investigations provide an experimental basis in the mechanisms of spray penetration induced collision in terms of collision probability and solid wetting distribution to the modeling work of Chapter 3.

CHAPTER 3

TRANSPORT OF INTERACTING AND EVAPORATING LIQUID SPRAYS IN A GAS-SOLID RISER REACTOR

3.1 Introduction

Transport of interacting and evaporating liquid sprays in a gas-solid flow reactor (e.g., FCC) is an important petroleum refining process for converting heavy hydrocarbon feed stocks into high-value products such as gasoline and light olefins. The process starts with injecting atomized oil feed into the bottom of a riser reactor, followed by feed vaporization and vapor cracking that are coupled with acceleration, cooling and concentration changes of catalysts and reacting vapor compositions. Typically the liquid feed are injected, in forms of atomizing sprays aerated by high-speed steam jets, into the dense cross-flow of hot steam-catalysts through multiple nozzles installed circumferentially on the reactor wall, referring to Figure 1.1.

The liquid spray transport in the feed zone is predominantly affected by the solid-droplet collisions, which not only promotes a rapid vaporization but also limits the spray penetration. Due to the mutual interactions of multiple sprays, as discussed in detail in Section 3.2.2, a cascade structure with mutual penetrating spray planes is formed in the feed zone. Both gas and solids are accelerated, coupled with cracking reactions, between any two neighboring spray planes towards the downstream of the riser flow. The changed transport conditions of gas-solid flows are consequently affecting the penetration and vaporization of sprays located directly in the downstream of the riser flow. Hence an integrated modeling approach needs to be developed to combine the mentioned spray mutual penetration, phase interactions, and coupled vaporization and cracking reaction.

According to literature in Section 1.2, there appear no reported studies on the detailed transport and reaction modeling of liquid sprays (with multi-spray interactions) in a dense gas-solid flow system. In order to develop such a model, one must include the following mechanisms that have been overlooked so far.

(1) A liquid spray transport model should be based upon the mechanistic phase transfer between solids and droplets by collisions. The model should also be coupled with vaporization, vapor-cracking reaction and multi-spray interactions;

(2) A mutual penetrating spray structure model needs been constructed. With the aid of (1), the mutual-interacting spray structure should yield not only the spray coverage and cross-sectional penetration but also the feed zone length.

(3) A transport and reaction model of gas-solid phases in the sub-regions between neighboring layers of sprays should be developed. Such a model will interact, in a cascade structure, with the spray transport of (1).

(4) Certain radial transport effects should be considered inside the spray injection zone.

(5) A final integrated three-phase transport and reaction model should be developed to yield radial profiles of transport and reaction variables at the end of spray injection zone.

Thus, this chapter aims to develop a theoretical framework to quantify the liquid feed transport, vaporization and cracking in the riser feed zone as well as to predict the radial profile of key transport variables at the end of feed zone. These key variables include velocities of gas and solids, volume fraction of solids, temperature, and molar concentrations of gases reactants. The radial profiles at the end of feed zone will provide the flow conditions for the modeling of downstream gas-solids transport and cracking reactions in the remaining part of the riser reactors.

In this chapter, the liquid spray model is based on the Lagrangian transport approach, whereas the gas-solid flow is described by a convection-dominated Eulerian

transport model. A four-lump kinetic reaction model is employed to account for the catalytic cracking reactions between vapor and solids. To illustrate the modeling capability, a case study with four square nozzles is presented and discussed.

3.2 Modeling Approaches and Construction of Sub-Models

3.2.1 Modeling Logic

The feed zone transport and reaction start with the injection of atomized oil feed into the dense cross-flow of hot steam and regenerated catalysts. The only give flow conditions are inlet transport properties of catalyst and steam as well as the injection properties of liquid spray. The entire riser reaction regions may be roughly divided into two sub-regions: the feed zone (where three-phase transport and reaction occur) and the main transport and reaction riser (where gas-solid two-phase transport and reaction occur). The radial profiles of transport and reaction properties at the end of the feed zone are thus regarded as the inlet conditions for the follow-up transport and reactions in the main riser reactors. In order to obtain such profiles, detailed quantitative modeling in the feed injection zone must be established. Such a model should be based upon all interacting mechanisms including (1) spray penetration and vaporization dominated by droplet-solids collisions, (2) mutual penetrating spray interactions, (3) accelerating transport of gas and solids stimulated by rapid spray vaporization, and (4) coupled catalytic cracking between the catalytic solids and reacting vapors. In this study sub-models have been developed to account for each individual mechanism mentioned above. Figure 3.1 provides a basic modeling logic of such an approach.

Firstly, the geometric modeling of mutually penetrating multi-spray interactions is built up; and a single spray transport model is developed with constrains of mutual penetrating multi-spray interactions. The multi-spray interaction model is designed to capture the transport characteristics of liquid phase and its interactions with gas

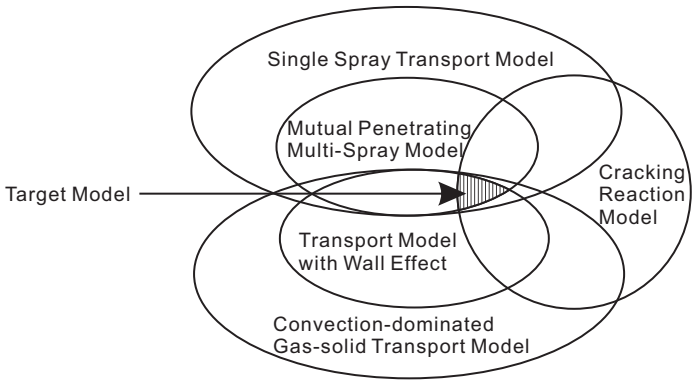

Figure 3.1 Multi-spray modeling logic.

and solid phases. Secondly, the convection-dominated gas-solid transport model is developed. In order to account for the wall effect, correlations based on numerical experiments are obtained to provide the radial re-distributions of gas and solids phases within the feed zone. The cascade interaction between the spray penetration model and the gas-solid transport model is thus able to yield the final radial profiles of transport and reaction variables at the end of feed zone. Concurrently, a reaction kinetic model needs to be implemented to couple with the transport models of spray, gas and solids. To end this, a simple four-lump kinetic network (VGO, gasoline, light gases and coke) is used for cracking reactions along the spray vaporization and transport region as well as within the transport region of reacting vapor and catalytic solids.

3.2.2 Mutual Penetrating Structure of Multi-Sprays

The geometry model of multi-spray interaction in a cross gas-solid flow can be quite complex, depending not only on the characteristic of nozzles (shape, size and number of nozzles), their location and injection angle, but also on the flow charactristics (both liquid spray and gas-solid flow) and the coupling physics including reaction and evaporation. Take four-nozzle case (evenly distributed along the riser wall) as an example. The schematic 3-D structure is shown Figures 3.2 and 3.3.

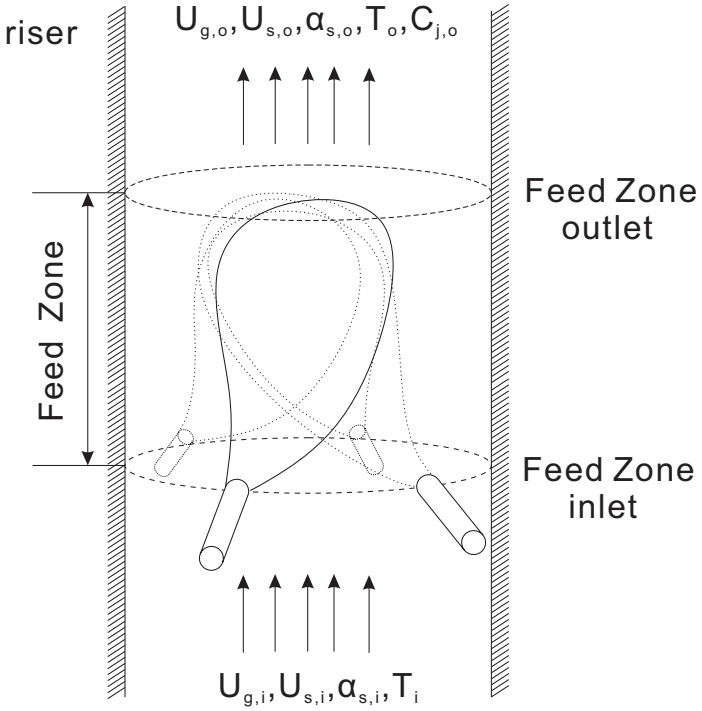

Figure 3.2 Spacious structure of four-nozzle sprays: side view.

To simplify the geometric analysis of this 3-D structure, without losing major interactive mechanisms, some assumptions are necessary:

a. The droplet inertia dominates the spray penetration path, with little deflections from the droplet-solids collisions (more discussions are given in Section 3.3.1).

b. The spray plane can penetrate each other without droplet-droplet collisions (due to the low volume fraction of liquid in the spray transport region).

c. The multi-spray are identical and axial-symmetrically arranged. Thus the interactive multi-spray penetration layers may be approximated by a cascade series of conical surface.

With above assumptions, the 3-D multi-spray structure can be modeled as shown in Figure 3.4. A major difference of multi-spray from the single spray is the gas and solids flow condition. For the single spray, the gas and solids flow condition is kept the same for spray coverage, while for each spray in a multi-spray system, the gas and solids flow condition can be changed due to the spray penetrating over

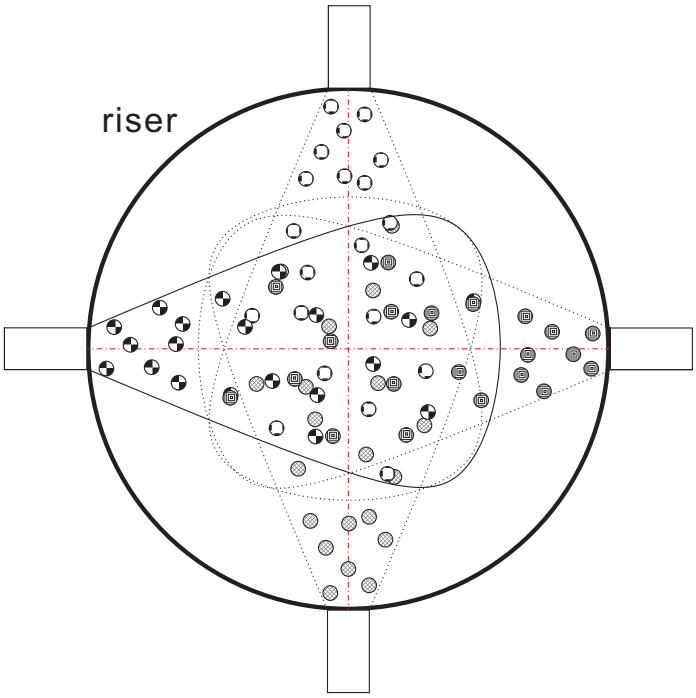

Figure 3.3 Spacious structure of four-nozzle sprays: top view.

each other. In other words, the gas and solids flow condition will be changed (due to the evaporation of spray) when the spray reaches the intersection with its left neighbor spray, and going to be further changed when it reaches to the intersection with opposite spray until passing through the last intersection.

In order to catch the side-to-side interaction effect (spray angle caused spray overlap), a single spray can be divided into N rays, as shown in Figure 3.4. Each ray can be represented as a smaller single spray. The spray angle of i^{th} ray can be given as,

$$\varphi_i = \frac{\varphi}{N_{ray}} \tag{3.1}$$

The above equivalency is based on the assumption that 1) there is no interaction between each ray inside the spray; 2) the liquid amount of spray is proportional to the injection area of the smaller nozzle; 3) all the rays share the same initial conditions of the whole spray characteristics (e.g., droplet injection velocity and its temperature).

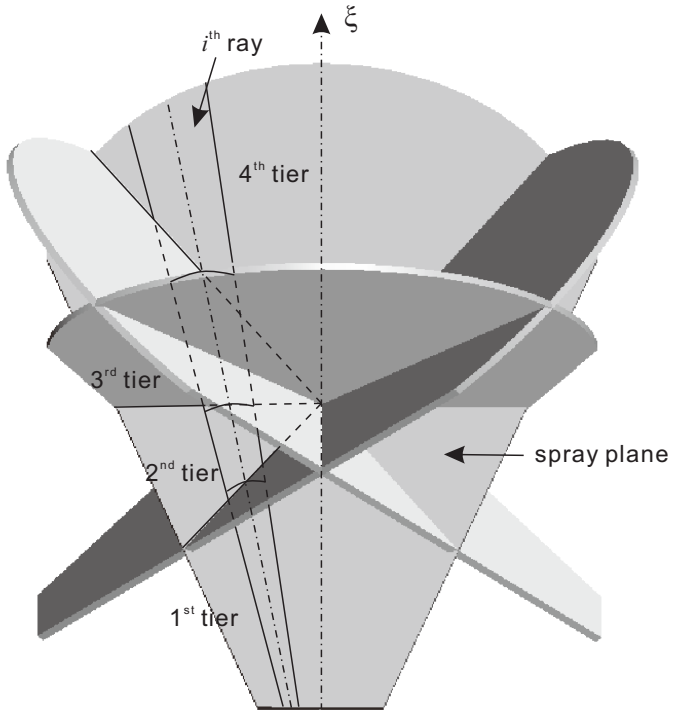

Figure 3.4 Spatial structure of multi-spray interactions.

The gas and solids flow condition for different rays is different as the intersections. Thus the penetration of each ray can be calculated and a profile can be given for the whole spray. It is noted that the injection angle of each ray can be different due to the spatial structure of spray angle, as shown in Figure 3.5. From the geometry structure, the injection angle of i^{th} ray (θ_k) can be related to the its position angle (φ_k) and injection angle (θ).

In order to couple the gas-solid transport sub-model [88] into the multi-spray model, a 2-D axial symmetric concept is introduced into the 3-D interactive structure. Figure 3.6 provides a view meridian plane of this axial symmetric approximation. Each spray interacts with all the other sprays sequentially from nearest neighbor to the farthest. These interactions form a series of spray and evaporating cone-shaped planes in the multi-spray structure. The gas and solids flow will pass through all the series of cones until to the outlet of feed zone. The gas and solids flow characteristics

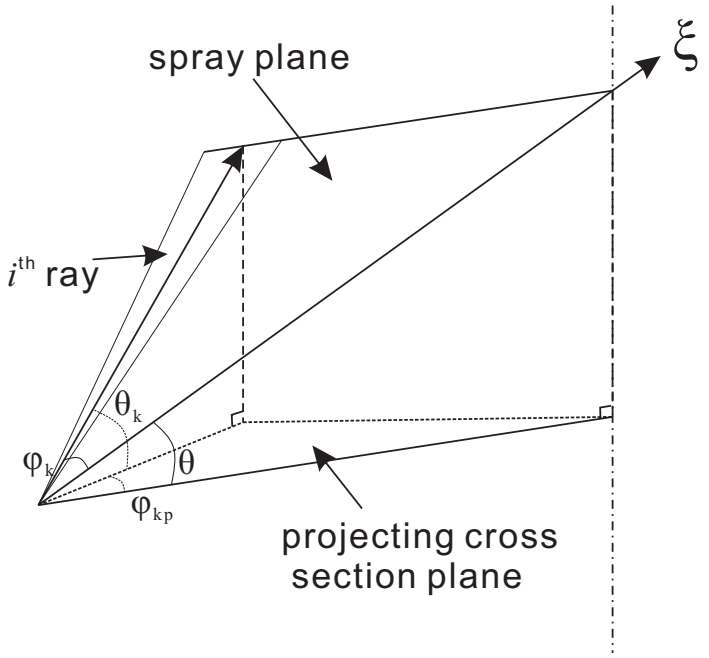

Figure 3.5 Spatial structure of injection angle (i^{th} ray).

will be changed (e.g., increasing in gas velocity; decreasing in temperature) whenever passing through a cone plane. In order to generally express this idea, a definition of tier is introduced and shown in Figure 3.6. Tier i is defined as the structure from i^{th} evaporation plane to $(i+1)^th$ evaporation plane.

From the view of tier structure, the gas and solids flow is affected and updated by passing through each spray evaporation plane, while each spray in the multi-spray structure is also influenced back by the updated gas and solid flow condition by passing through each intersection with other sprays (Figure 3.4). Based on this structure, the multi-spray interaction modeling framework can be achieved with the aid of sub-models (detailed in Sections 3.2.3 to 3.2.6).

For simplisity, the conical section (Figure 1.1) of the riser is replaced by an cylindrical section in the current modeling. The conical divergence effect on gas-solid flow and consequent impact on spray behavior is too complicated to be dealt with and thus should be regarded as a seperated research topic in future studies.

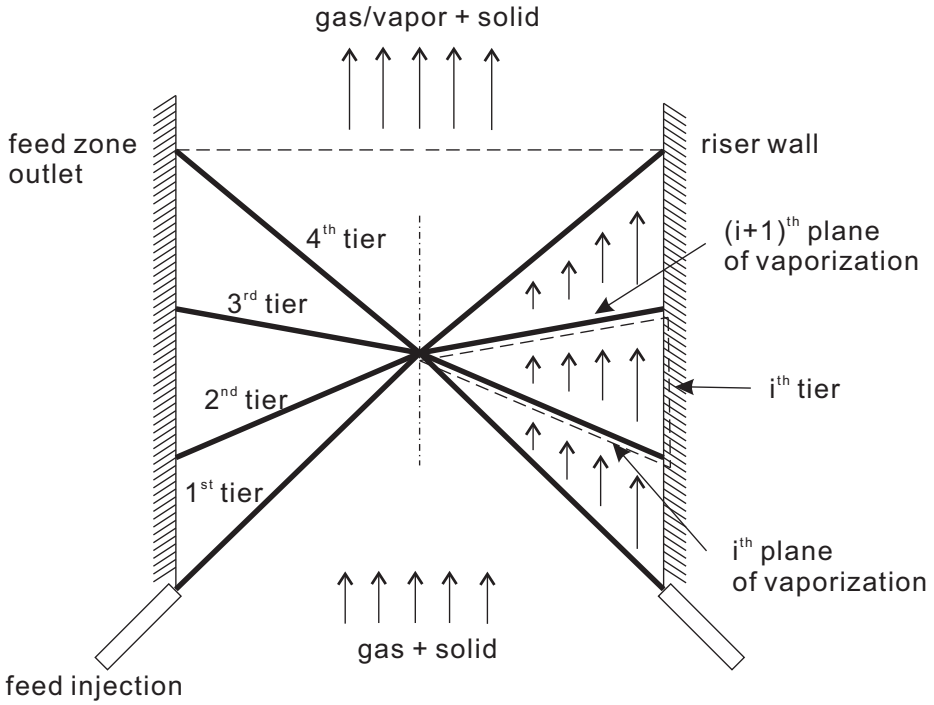

Figure 3.6 Multi-spray axial-symmetric approximation.

3.2.3 Transport of a Spray Ray

Consider a plain-orifice atomizer that injects a compact, uniform spray at an angle into an unbounded cross-flow of hot catalyst particles (See Figure 3.7). The temperature of the catalyst is far higher than the boiling point of the heaviest component of the oil drop. The collision between the high-velocity liquid spray and the flow of massive catalyst particles promotes intense momentum and heat transfer, leading to vaporization of the drops, and cracking of reactive hydrocarbon species. Thus, it is a complex system involving inter-phase transport accompanied by cracking reactions in a vaporizing gas-solid-liquid flow governed by droplet-catalyst collision. Following assumptions are made to develop as simple a model as possible and capture most of the dominant features of the system. (1) The adiabatic riser is at a quasi-steady state, (2) The spray penetration trajectory is one-dimensional and symmetric, (3) Catalyst entrainment in the spray region is by the gas jet,(4) A local thermal equilibrium between hot solids and gas phase is quickly established outside the spray region,

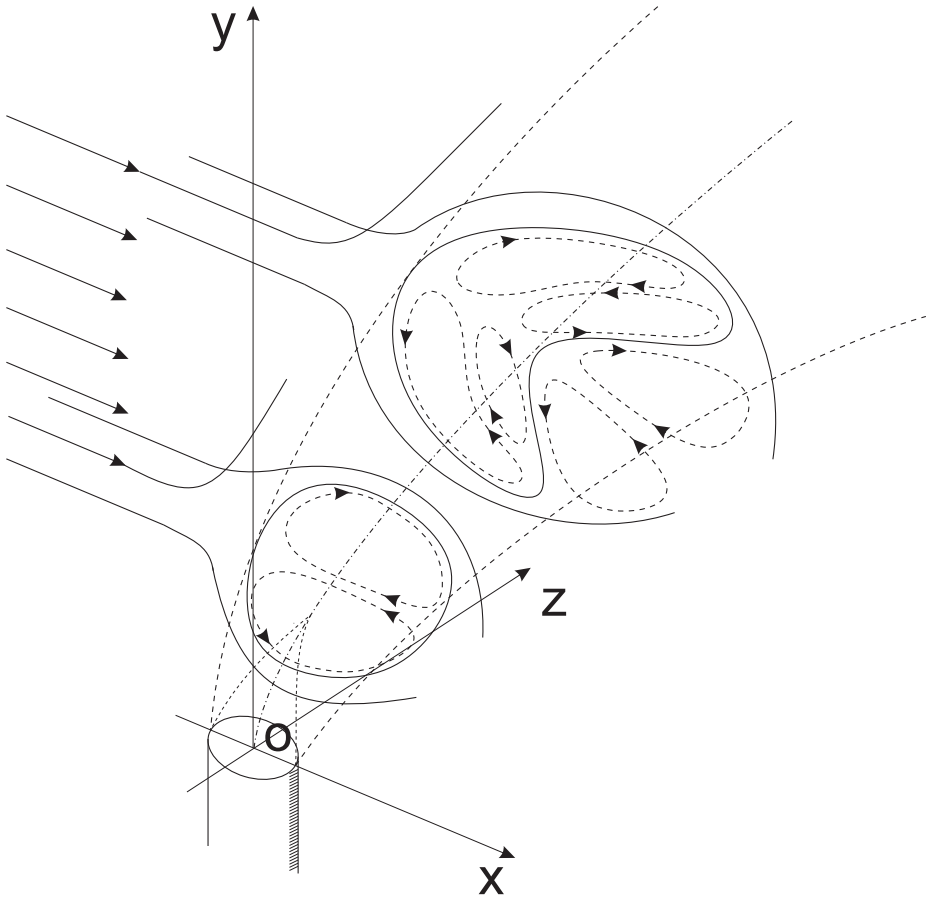

Figure 3.7 Unbounded jet injected into gas-solid cross flow.

Source: [1]

(5) Drop sizes variation is represented by an average drop size, (6) Thermophysical parameters are constants, (7) Heat transfers by radiation and natural convection are negligible, (8) The same catalyst deactivation function can be used for all reactions, and (9) Hydrocarbon vapors and steam behave like an ideal gas.

A deterministic Lagrangian trajectory approach is used to develop the governing conservation equations for the three-phase flow along the sprays centerline. The spray is injected at an angle θ to the horizontal into an unbounded cross-flow of hot catalyst. The one dimension model proposed in this study is along the centerline of evaporating spray (denoted as the ξ direction). The general forms of the mass, momentum, and

energy balance equations over a control volume in each phase are of the following form [60].

$$\frac{d}{d\xi}\left(\alpha_i \rho_i u_i A \phi_i\right) = S_{\phi i} + S_1 \tag{3.2}$$

When the index i takes on the values g, d, and s, the corresponding phases are gas, liquid (droplet), and solid, respectively. The expressions for the source terms and are shown in Table 3.1. The physical meanings of the symbols are listed in the nomenclature section.

Table 3.1 Definitions of ϕ_i and Source Terms in Equation 3.2

Phase	Equation	ϕ_i	$S_{\phi i}$	S_1
Gas	Continuity	1	$\dot{m}_{ge} l - \gamma \alpha_g \rho_g u_g l$	$\dot{m}_v A$
	Momentum	u_g	$\dot{m}_{ge} u_{g\infty} l \cos\theta - \gamma\, \alpha_g \rho_g u_g^2 l$	$\dot{m}_v u_d A - \left(F_{Dd} + F_{Ds}\right) A$
	Energy	$c_{pg} T_g$	$\dot{m}_{ge} l c_{pg} T_\infty - \gamma \alpha_g \rho_g u_g c_{pg} T_g l$	$\dot{m}_v L A + E_{Cs} - E_{Cd} - E_R$
Liquid	Continuity	1	$-\dot{m}_v A$	0
	Momentum	u_d	$-\dot{m}_v u_d A$	$\left(F_{Dd} - F_{Cds}\right) A$
	Energy	$c_{pd} T_d$	$-\dot{m}_v L A$	$E_{Cds} + E_{Cd}$
Solid	Continuity	1	$\dot{m}_{se} l + \dot{m}_{sp} l$	0
	Momentum	u_s	$(\dot{m}_{se} l + \dot{m}_{sp} l) u_{se} \cos\theta$	$\left(F_{Ds} + F_{Cds}\right) A$
	Energy	$c_{ps} T_s$	$(\dot{m}_{se} l + \dot{m}_{sp} l) c_{ps} T_\infty$	$-E_{Cds} - E_{Cs}$

Note that the gas and solids flow conditions are denoted by the subscript ∞ in the following tables. The volume fractions of the three phases are constrained by

$$\alpha_s + \alpha_g + \alpha_d = 1 \tag{3.3}$$

Correlations and constitutive relations that are derived mechanistically, empirically, or phenomenologically are listed in Tables 3.2 and 3.3. The details of the correlations and other supplementary information can be found elsewhere [60].

Table 3.2 Constitutive Relations and Correlations

Physical meaning	Symbol	Expression
Drag force	F_{Di}	$n_i c_{Di} \frac{\pi}{8} {d_i}^2 \rho_g \left\|u_g - u_i\right\| (u_g - u_i), i = d, s$
Collision momentum transfer	F_{Cds}	$f_{ds} \frac{m_s m_d}{(m_s + m_d)} (u_d - u_s)$
Collision frequency [20]	f_{ds}	$\eta_{co} n_d n_s \frac{\pi (d_s + d_d)^2}{4} \left\|u_s - u_d\right\|$
Collision efficiency [90]	η_{co}	$\eta_{co} = \left(1 + 34 \frac{d_d}{d_s} \frac{\rho}{\rho_s} \frac{1}{\mathrm{Re}_{sd}}\right)^{-2}$
Collision heat transfer	E_{Cds}	$f_{ds} \frac{\pi}{6} d_s^3 \rho_s C_{p,s} (T_s - T_d)$
Reaction heat	E_R	$-\sum_{i=1}^{5} r_i . \Delta H_i A$
Heat convection	E_{ci}	$n_i \pi d_i^2 h_i (T_g - T_i), i = d, s$
Heat transfer coefficient	h_i	$h_i = \frac{Nu_i K}{d_i}, i = d, s$
Nusselt number for evaporating droplet	Nu_d	$\frac{2 + 0.6 \,\mathrm{Re}_d^{*0.5} \mathrm{Pr}^{0.333}}{\left[1 + \frac{C_p (T_g - T_d)}{L}\right]^{0.7}}$
Nusselt number for particle [7]	Nu_s	$2 + 0.6 \mathrm{Re}_s{}^{0.5} \mathrm{Pr}^{0.333}$
Reaction rate Constant	k_i	$k_i = \bar{k}_{i0} \left(\frac{C}{O}\right) \exp\left(-\frac{E_i}{R T_i}\right)$
Partition function for vapor convection	γ	$\left(\frac{\alpha_{s\infty} \rho_s {u_{s\infty}}^2 + \alpha_{g\infty} \rho_g {u_{g\infty}}^2}{\alpha_s \rho_s {u_s}^2 + \alpha_g \rho_g {u_g}^2 + \alpha_d \rho_d {u_d}^2}\right)^n$
Droplet vaporization rate	$\dot{m}_v$	$\chi_v \frac{E_{Cds} + E_{cs}}{L}$

Source: [60]

Here C/O is the local catalyst-to-oil ratio along the spray. Note that the pre-exponential factor $\bar{k_{i0}}$ in Table 3.2 is molar-based, which can be expressed in terms of mass-based pre-exponential factors k_{i0}.

Table 3.3 Empirical Correlations

Item	Symbol	Correlation
Entrainment	$\dot{m}_{ge}, \dot{m}_{se}$	$\alpha_{i\infty}\rho_{g\infty}\left[0.06(u_i - u_{i\infty}\cos\theta) + 0.3u_{i\infty}(\cos\theta - \cos\theta_0)\right], i = d, s$
Solid penetration	$\dot{m}_{sp}$	$\alpha_{s\infty}\rho_s u_{s\infty}\sin\theta \exp\left(-\frac{\alpha_{s\infty}\rho_s(u_{s\infty}\sin\theta)^2}{\alpha_s\rho_s {u_s}^2 + \alpha_g\rho_g {u_g}^2 + \alpha_d\rho_d {u_d}^2}\right)$

Source: [62]

In this single unbounded spray model, the spray cross section varies along its trajectory, shown as Figure 3.8. Assume that the height of the spray (h) is considered as constant while the width (w) is increasing based on the initial injection angle. It is also assumed that the shape of the rectangular cross section is not affected by the recirculation inside caused by the gas and solids flow (see Figure 3.8b).

It is noted that for the multi-spray interaction model to take into account the interaction between sprays with certain spray angle, a single spray model is adopted directly for each ray of a spray and iterated with the gas-solid transport sub-model when the spray reach the boundary of each tier, as shown in Figure 3.4.

3.2.4 Convective Transport of Gas-Solid

Based on convection dominated gas-solid transport assumption, the governing conservation equations for gas and solid phase flow along the riser axis are developed. The general forms of the continuity and momentum balance equations over a control volume in each phase are of the following form [88],

$$\frac{d}{dz}\left(\alpha_i\rho_i u_i\phi_i\right) = S_{\phi i} + S_1 \tag{3.4}$$

Where the index i takes on the values g and s. The expressions for the source terms and are shown in Table 3.4. The details of the correlations and other supplementary information can be found elsewhere [88].

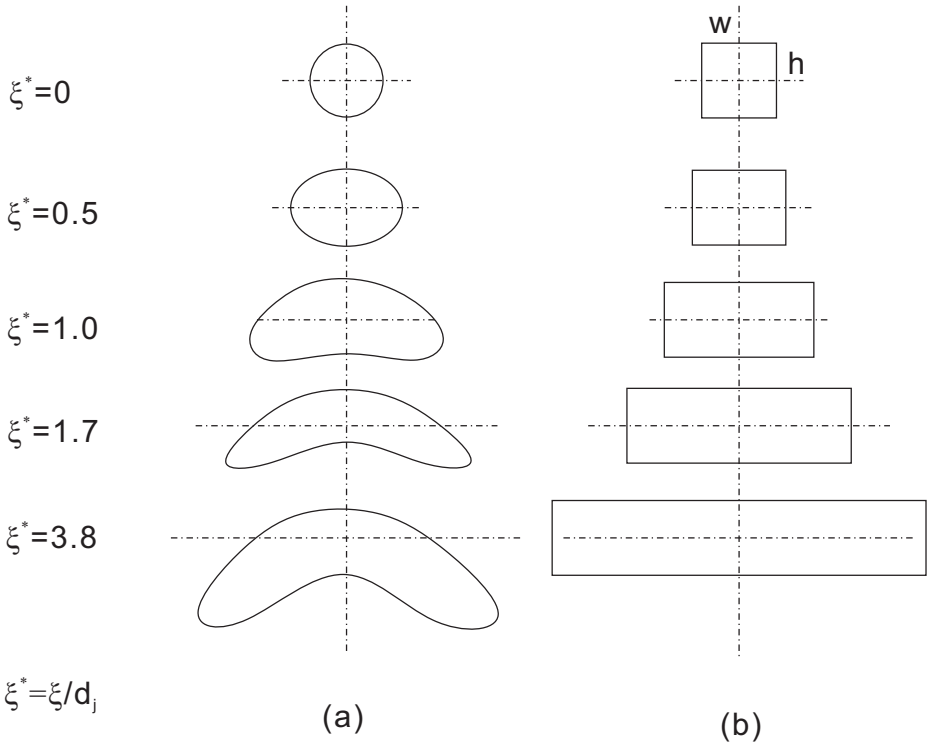

Figure 3.8 Cross section of a cross-flow jet along trajectory (a) Typical cross section* (b) Rectangular approximation.

Source: * [1]

Table 3.4 Definitions of ϕ_i and Source Terms in Equation 3.4

Phase	Equation	ϕ_i	$S_{\phi i}$	S_1
Gas	Continuity	1	0	$-(r_3 + r_5)$
	Momentum	u_g	$-\alpha_g \rho_g g$	$-\frac{dP}{dz} - F_D$
Solid	Continuity	1	0	$r_3 + r_5$
	Momentum	u_s	$-\alpha_s \rho_s g$	$F_D - F_C$

It is noted that to consider the radial effect during the transport, the riser is divided to a certain number of annular rings. The gas-solid convection dominated transport model is thus adopted for each annular ring, as shown in Figure 3.9. By averaging the amount of evaporation in each ray (spray) to the annular ring through

each spray penetration, the convection dominated gas and solids conditions can be updated through each tier.

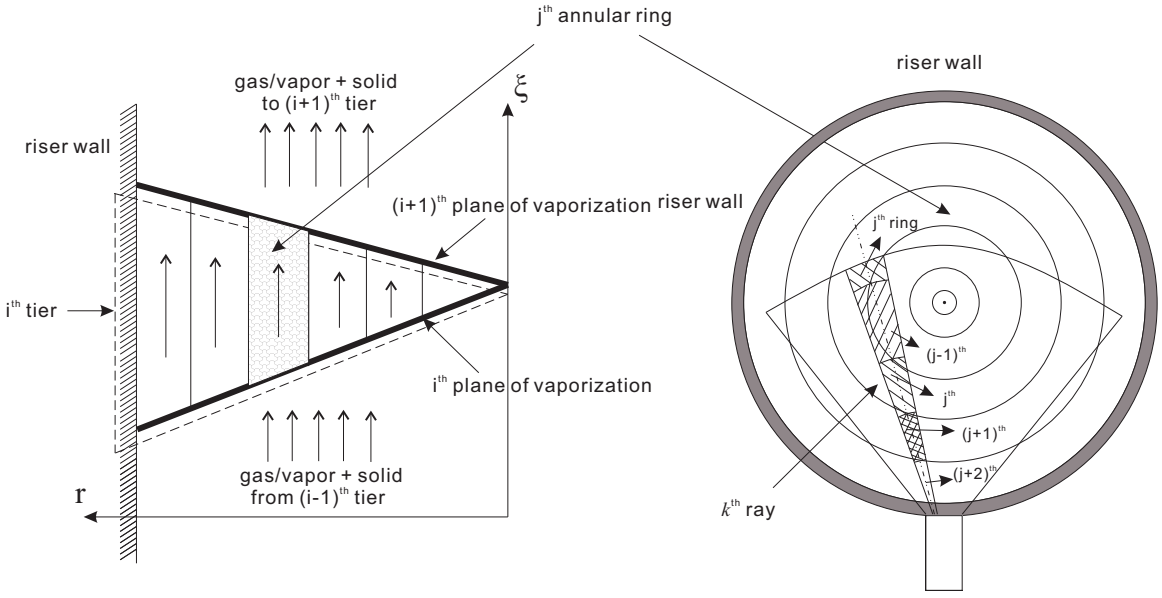

Figure 3.9 Gas-solid transport in annular ring.

3.2.5 Catalytic Reaction Model

In FCC riser reactors, steam is injected upstream of the feed injection zone to help disperse the catalyst. Here, the effect of steam on cracking kinetics can be ignored.

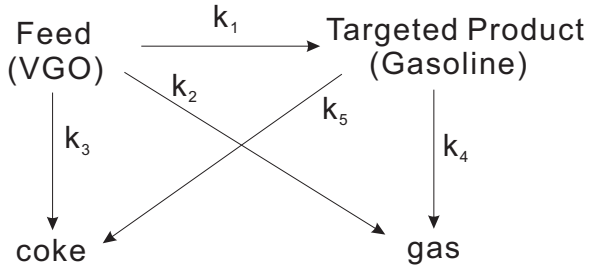

Figure 3.10 Four-lump reactions.

Based on the afore-mentioned four-lump kinetic model (See Figure 3.10), the molar concentration balance equations for each chemical lump as well as steam can

Table 3.5 Coefficients for Equation 3.5

Lump	Γ_{1j}	Γ_{2j}	Γ_{3j}
VGO	$-\left(k_1+k_2+k_3\right){C_1}^2$	0	$\frac{\dot{m}_v A}{M_1}-\gamma C_1 u_g l$
Gasoline	$\frac{M_1}{M_2}k_1{C_1}^2$	$-(k_4+k_5)C_2$	$-\gamma C_2 u_g l$
Light Gases	$\frac{M_1}{M_3}k_2{C_1}^2$	$\frac{M_2}{M_3}k_4 C_2$	$-\gamma C_3 u_g l$
Coke	$\frac{M_1}{M_4}k_3{C_1}^2$	$\frac{M_2}{M_4}k_5 C_2$	$-\gamma C_4 u_g l$
Steam	0	0	$\frac{\dot{m}_{ge} l}{M_5}-\gamma C_5 u_g l$

Source: [58]

be written as follows [60]:

$$\frac{d}{d\xi}\left(C_j u_g A\right)=\Gamma_{1j}\Phi_s A+\Gamma_{2j}\Phi_s A+\Gamma_{3j} \tag{3.5}$$

Where Φ_s is the catalyst deactivation function due to coke deposition on the catalyst surface. Where the index j takes on the values 1, 2, 3, 4, and 5, the corresponding species are VGO, gasoline, light gases, coke, and steam, respectively. The expressions for Γ_{1j}, Γ_{2j} and Γ_{3j} are listed in Table 3.5.

The gas density of the vapor mixture can be obtained based on the ideal gas law

$$\rho_g=\frac{P}{RT_g}\frac{\sum_{j=1}^{5}\left(C_j.M_j\right)}{\sum_{j=1}^{5}C_j} \tag{3.6}$$

Correlations and constitutive relations that are derived mechanistically, empirically, or phenomenologically are listed in Tables 3.2 and 3.3. The details of the correlations and other supplementary information can be found elsewhere [58].

3.3 Exemplified Results and Discussion

In order to make an illustration of the proposed model, a case of four-square nozzle sprays into a gas-solid FCC riser is calculated. The flow conditions physical properties of all phases are listed in Table 3.6, and the parameters of kinetic reactions are given in Table 3.7.

3.3.1 Spray Mass Distributions and Coverage

The cut-off or spray ending criterion is defined as the size ratio of ending droplet to the injected droplet less than 1/3. In other words, the spray ends when its mass residue is less than 4% of its injected mass. Figures 3.11 and 3.12 shows the mass residue distributions of spray droplets along the spray trajectory (ξ's) and along the projected trajectories in the cross-section plane, respectively. The mass vaporization distribution is thus determined from the reduction of the droplets mass residue.

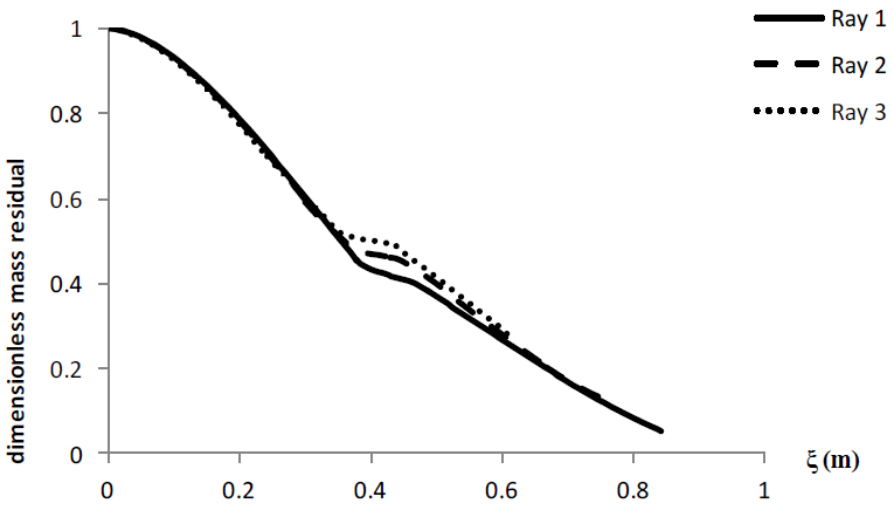

Figure 3.11 Mass residual distributions of various rays: along trajectory ξ.

It should be noted that, in Figures 3.11 and 3.12, different droplet trajectories are dispersed. In other words, the various ξ's do not overlap each other. Figure 3.13 shows the spray coverage from the top view of a riser cross-section. The shaded part shows the area not covered by the spray. When a spray reaches to the riser wall, the

Table 3.6 Operating Parameters and Thermophysical Constants

Parameter	Value
Catalyst feed rate (kg/s)	180
Riser diameter (m)	0.6
Riser inlet temperature (K)	980
Inlet riser pressure (atm)	3
Nozzle size (mm)	40
Nozzle injection angle (degree)	45
Gaseous jet velocity (m/s)	26
Crude oil molecular weight (kg/kmol)	220
Gasoline molecular weight (kg/kmol)	108
Light gases molecular weight (kg/kmol)	28
Coke molecular weight (kg/kmol)	220
Droplet volume fraction at injection	0.09
Droplet velocity at injection (m/s)	26
Droplet temperature at injection (K)	450
Droplet size at injection (m)	270
Droplet density (kg/m3)	900
Droplet saturated temperature (K)	670
Droplet latent heat (J/kg)	279000
Solids (catalyst) size (m)	70
Solids bulk density (kg/m3)	1450
Solids volume fraction at riser inlet	0.27
Steam velocity at riser inlet (m/s)	3.5

remaining mass residue is assumed to contribute to the wall region only, i.e., there is no droplets rebounding from the wall collisions.

Table 3.7 Parameters of four-Lump Kinetic Model

Sub-Cracking Reaction	ΔH_i (kJ/kg)	k_{i0} (g oil/(s g cat))	E_{ai} (kJ/kmol)
VGO to Gasoline	195	1457.5	57359
VGO to Light Gases	670	127.59	52754
VGO to Coke	745	1.98	31830
Gasoline to Light Gases	530	256.81	65733
Gasoline to Coke	690	0.022	66570

Source: [30]

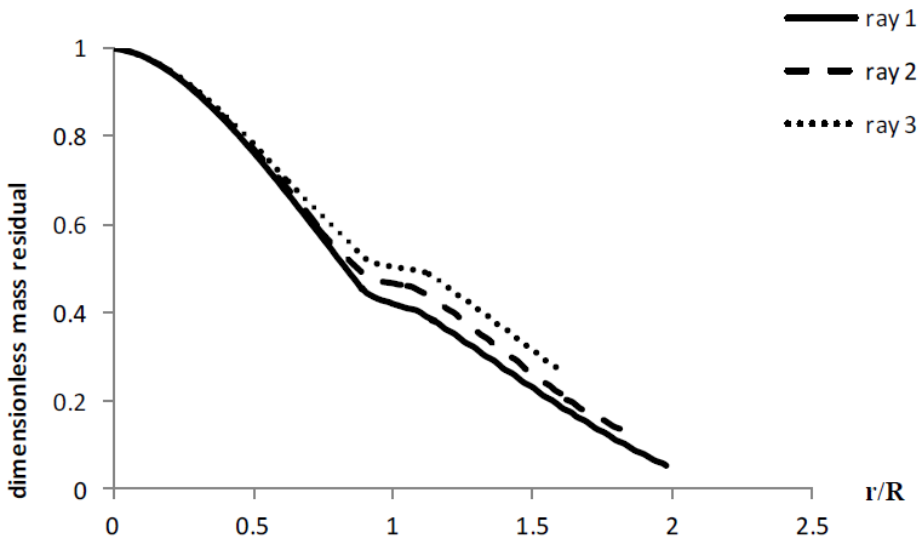

Figure 3.12 Mass residual distributions of various rays: along projected ξ in cross-section.

The mutual penetrating spray structure in Section 3.2 is based upon an important assumption of no deflection of spray trajectories, i.e., inertia-only sprays. Such an assumption can be tested from the previous modeling of sprays without spray-spray interactions [60]. A comparison between deflected trajectory and non-deflected one (inertia line) of a single spray is shown in Figure 3.14. The comparison indicates that there is little deflection of the spray until approaching to its ending. This may be due to the fact that, when the spray penetration ends,

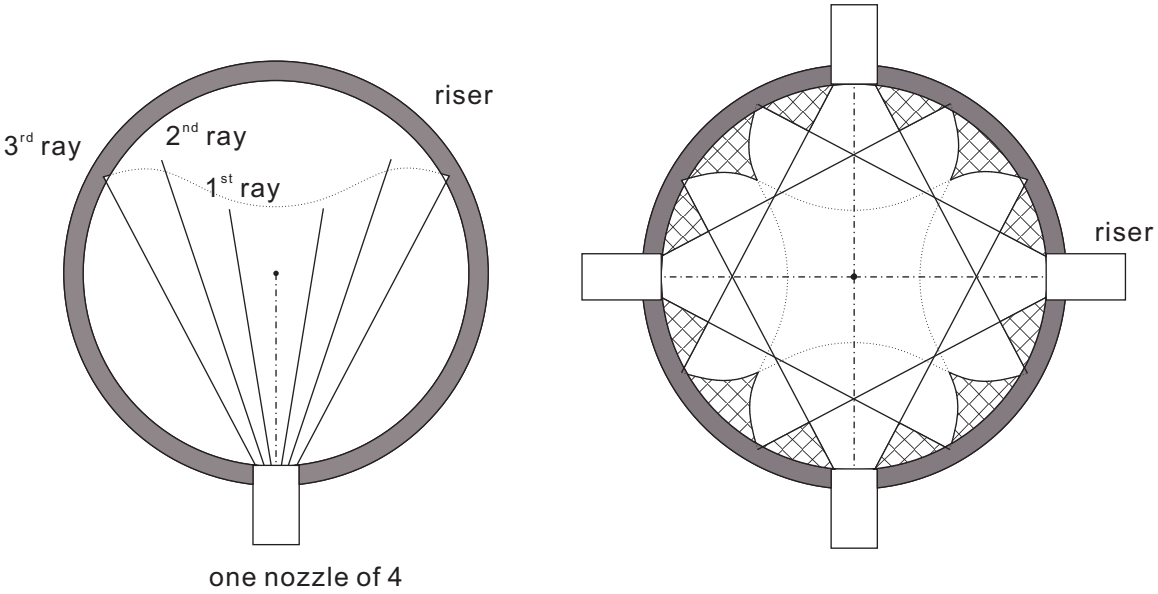

Figure 3.13 Cross-sectional spray coverage of single spray (left) and combination of four sprays (right).

the size of residue droplet can still be considerably larger than that of FCC solids, and hence the inertia trajectory is basically preserved.

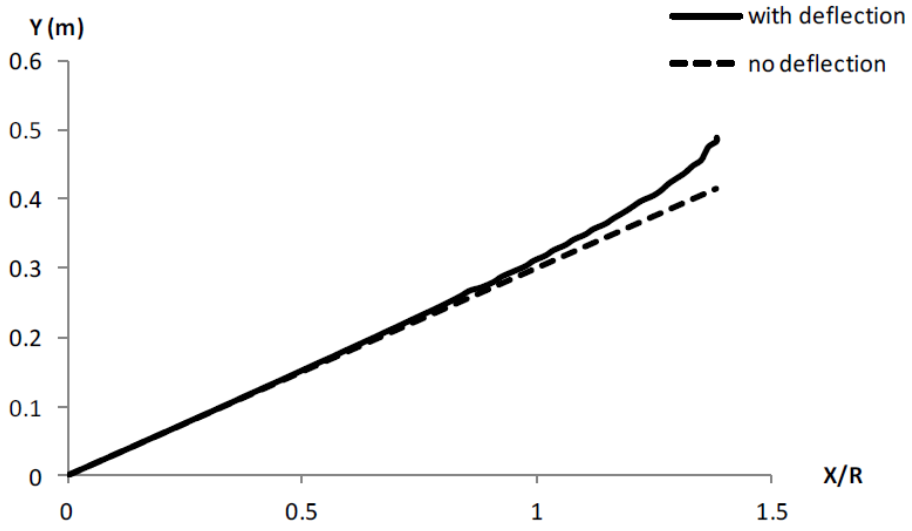

Figure 3.14 Spray trajectory with/without deflection.

3.3.2 Radial Profiles at End of Feed Zone

The radial distributions of phase transport properties and reactant products are presented in this section. Figure 3.15 shows the velocities of vapor and solids before and after the feed zone. Due to the spray vaporization and phase acceleration, the averaged gas velocity is increased from 5 m/s to about 22 m/s. The non-uniform distribution of gas velocity at the end of feed zone suggests a non-uniform vaporization and cracking inside the feed zone. The averaged solid velocity is increased from 2 m/s to about 5.5 m/s. The averaged slip factor between solids and gas velocities is about 0.25, a value far below the slip velocity in a fully developed dilute transport (estimated by the particle terminal velocity to that of gas transport velocity). This low slip factor indicates the transport of solids is very much restricted by the collisions among the dense phase solids.

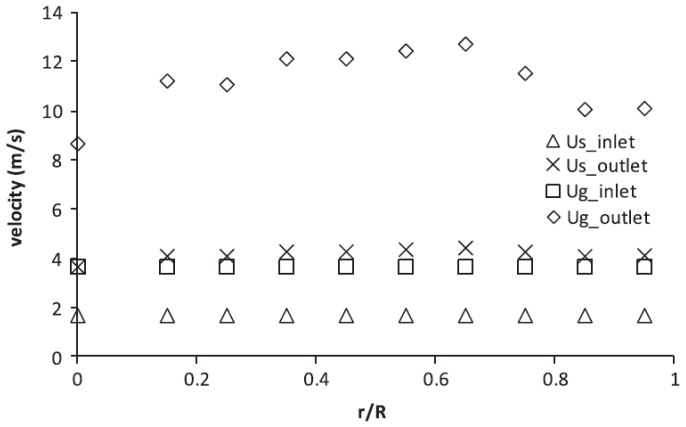

Figure 3.15 Gas/solid velocity profile at end of feed zone.

Figure 3.16 shows the solid volume fraction distribution. Coupled with the solids acceleration, the averaged solid volume fraction is decreased from 0.27 to about 0.09. The radial distribution of solid volume fraction is fairly uniform, compared that of velocity profiles.

Figure 3.17 gives the radial distributions of molar concentration of gaseous reactants or products at the end of feed zone. It is shown that the catalytic

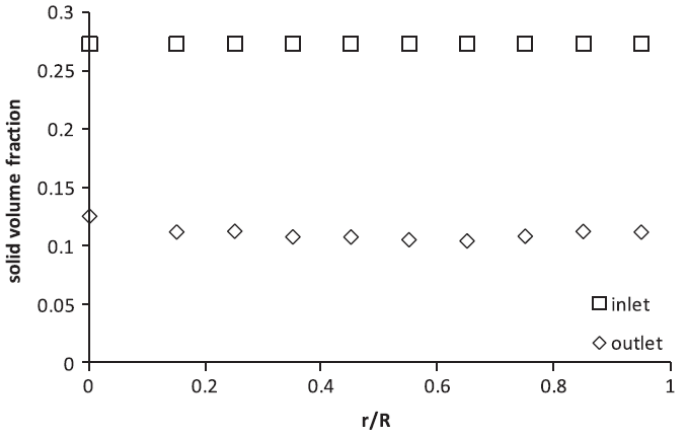

Figure 3.16 Solid volume fraction profile at end of feed zone.

reaction occurs non-uniformly across the radial direction, with the maximum located somewhere between the center and wall of the riser.

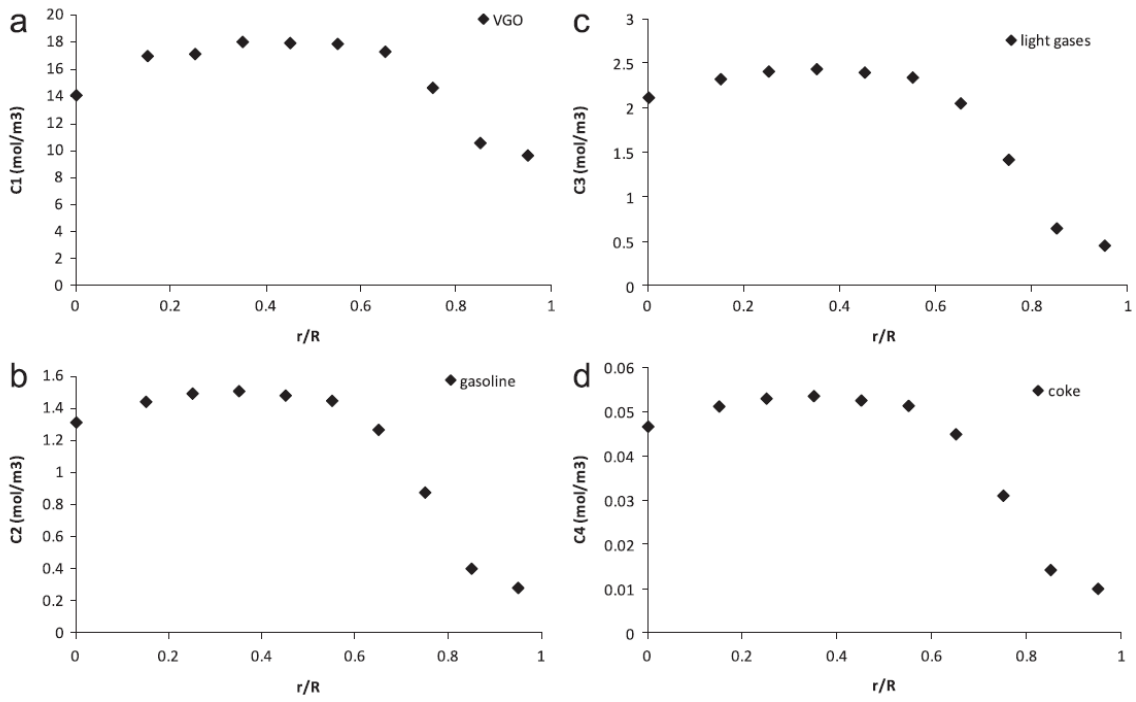

Figure 3.17 Molar concentration radial distribution of reactant. (a) VGO, (b) gasoline, (c) light gases and (d) coke.

3.4 Relevance to Other Chapters

This chapter is focused on the modeling work of multi-spray intervened gas-solid transportation. The liquid spray transport in the feed zone is predominantly affected by the solid-droplet collisions, which not only promotes a rapid vaporization but also limits the spray penetration. Both gas and solids are accelerated, coupled with cracking reactions, between any two neighboring spray planes towards the downstream of the riser flow. The changed transport conditions of gas-solid flows are consequently affecting the penetration and vaporization of sprays located directly in the downstream of the riser flow. Thus the modeling work of Chapter 3 can provide initial inlet condition for the downstream gas-solid transport in the riser flow, which is discussed in Chapter 4.

CHAPTER 4

A TWO-ZONE MODEL FOR FLUID CATALYTIC CRACKING RISER WITH MULTIPLE FEED INJECTORS

4.1 Introduction

FCC riser reactor for converting petroleum fractions is designed to use catalysts to crack heavy-molecular hydrocarbons, such as vacuum gas oil (VGO), into more valuable lighter hydrocarbons. The focus of this chapter is on the riser reactor. Referring to Figure 4.2, the liquid feed enters the riser reactor through multiple feed atomizing nozzles, contacts hot regenerated catalyst, and vaporizes. The resulting vapor cracks as it travels upward along with the catalyst against gravity in the riser. Because of vaporization and cracking, the vapor expands, thus increasing the velocities of both reacting gas mixture and catalyst along their transport through riser. The increased catalyst velocity dilutes the catalyst volumetric concentration and hence lowers the local catalyst-to-oil (CTO) ratio. Concomitant with this is the deposition of coke, a byproduct from cracking, on the catalyst surface, which reduces the catalysts cracking activity. The deactivated catalyst is separated out from the hydrocarbon stream through cyclones at riser exit. Upon regeneration via coke burning in a high-temperature regenerator, the catalyst is fed back to the riser to complete the recirculation loop of catalyst transport. As one of the most important component in this refinery system, the fluid catalytic cracking (FCC) riser reactor consists of a bottom section of liquid feed injection and vaporization and an upward straight riser of vapor-catalysts transport and reaction. The product yield, obtained at the top of riser, is an accumulative result of liquid feed injection, vaporization by contacting with hot catalysts, and subsequent catalytic cracking of feed vapor while being transported concurrently with catalysts through the riser. The FCC process

involves not only these sequential sub-processes but also complicated coupling among multiphase fluid hydrodynamics, heat and mass transfer between phases, and catalytic kinetic reactions of vapor components in each sub-process.

Per literature survey in Section 1.2, up to present there is no modeling approaches can be directly used for FCC on-line control, monitoring, and optimization. This state of affairs motivated us to develop a hybrid modeling approach aimed at striking the right balance between the two asymptotic approaches (i.e., traditional plug-flow model and CFD-based model). In addition, there is a need to address the issue of entrance cracking via development of a quantitative treatment of the riser bottom including the feed injection zone. These considerations led us to construct a one-dimensional (1-D) heterogeneous riser model capturing the dominant features of the interactions between hydrodynamics and cracking kinetics [88]. Specifically, it accounts for catalyst acceleration, particle-particle collision force, and particle-fluid interfacial force. In an ensuing study, an averaging approach for modeling transport-reaction coupling in the feed injection zone with two overlapping round nozzles was developed [60]. The results showed that cracking at the riser bottom plays an important role in determining the performance of an FCC riser. The treatment was further extended to injection zones having four overlapping square nozzles [59].

Based on the approaches developed in the previous studies, here a more realistic FCC model that has four symmetric, overlapping fan-shaped atomizing nozzles is constructed [47, 39]. This type of nozzles provides a wide and fairly uniform feed coverage across the catalyst stream, thus starting the vapor-phase cracking as early as possible. The model consists of two parts: a feed injection zone and a downstream fully developed riser zone. The former provides the inlet condition for the latter. Each of the two zones is represented by a system of first-order ordinary differential equations (ODEs) that governs the interplay of convective transport and cracking reactions.

As such, the two-zone hybrid model (TZHM) can accommodate a large number of reactions, thus allowing full molecular characterization of feedstocks and FCC products. For illustrative purposes, this work uses a literature four-lump cracking kinetic model.

In what follows, the model of the downstream riser zone is developed. This is followed by constructing the feed injection zone model and combining the two sub-models into a single two-zone model for the entire riser. The resulting model provides new insights into the inner working of the riser. Moreover, it can adequately explain the data of [14] obtained from a commercial FCC riser.

4.2 Modeling of Fully Developed Riser Zone

The fully developed riser zone is characterized by transport and reactions involving only gaseous species and catalyst. To proceed further, the following assumptions are made:

(1) gas and catalyst flows are dominated by convection in the axial direction;

(2) all transport variables such as velocity and temperature are locally averaged over the riser cross section, and hence vary only along the flow direction;

(3) the riser is adiabatic;

(4) gaseous species obey the ideal gas law;

(5) cracking rates are described by a four-lump kinetic model including vacuum gas oil (VGO), gasoline, light gases and coke, as shown in Figure 4.1;

(6) the aeration steam is treated as an inert species;

(7) coke is regarded as an added mass to the catalyst.

The overall and component mass balances for the gas phase can be compactly written as

$$\frac{d}{dz}\left(\alpha_g \phi_g U_g\right) = \Gamma_g \tag{4.1}$$

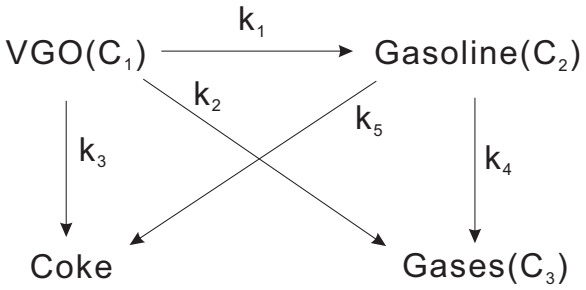

Figure 4.1 Four-lump kinetic model for vacuum gas oil cracking.

where ϕ_g and Γ_g represent, respectively, a transport variable of gas phase and its associated source term, as can be seen in Table 4.1. Note that the meanings of symbols in equations can be found in the nomenclature section.

Table 4.1 Meaning of ϕ_g and Γ_g in Equation 4.1

Species	ϕ_g	Γ_g
Gas phase overall	ρ_g	$-(r_3 + r_5)$
VGO component	$C_1 M_1$ or ρ_1	$-(r_1 + r_2 + r_3)$
Gasoline component	$C_2 M_2$ or ρ_2	$r_1 - r_4 - r_5$
Gases component	$C_3 M_3$ or ρ_3	$r_2 + r_4$
Steam component	$C_{st} M_{st}$ or ρ_{st}	0

The five reactions shown in Figure 4.1 are represented by r_i (i = 1, 2, . . .5). The cracking reactions of the feedstock (VGO) and gasoline are second order and first order, respectively [80, 12, 71]. The mass-based reaction rates r_i (kg/m^3-s) for the i^{th}-reaction in Figure 4.1 are expressed as:

$$r_i = \begin{cases} \Phi_s k_i C_1^2 M_1 & i = 1, 2, 3 \\ \Phi_s k_i C_2 M_2 & i = 4, 5 \end{cases} \tag{4.2}$$

Here the reaction constant k_i takes the Arrhenius form, which is corrected for variation in the local CTO ratio [88]

$$k_i = \bar{k}_{i0}\lambda(z)\exp\left(-\frac{E_{ai}}{RT_s}\right) \tag{4.3}$$

where

$$\bar{k}_{i0} = \begin{cases} \left(\frac{M_1}{\alpha_g \rho_g}\right) k_{i0} & i = 1, 2, 3 \\ k_{i0} & i = 4, 5 \end{cases} \tag{4.4}$$

The local CTO ratio, $\lambda(z)$, is given by

$$\lambda(z) = \left(\frac{C}{O}\right)_i \left(\frac{\alpha_s}{\alpha_{s,avg}}\right)^n \tag{4.5}$$

where the average catalyst volume fraction is calculated by

$$\alpha_{s,avg} = \frac{1}{H}\int_0^H \alpha_s dz \tag{4.6}$$

The catalyst deactivation function, Φ_s, is related to coking content on catalyst and given by the following correlation [21, 61]

$$\Phi_s = \frac{4.29 + 1}{4.29 + \exp\left(10.4 \cdot C_C\right)} \tag{4.7}$$

where C_C is catalyst coke content in weight percentage (wt%).

The overall mass balance is the sum of all component balances, thus only four out of the five equations in Equation 4.1 are independent. Here the gas phase consists of VGO, gasoline, hydrocarbon gases, and steam, while the coke lump is treated as a component of solid phase. The overall gas density ρ_g is given by

$$\rho_g = \sum_{i=1}^{3} \rho_i + \rho_{st} = \sum_{i=1}^{3} C_i M_i + C_{st} M_{st} \tag{4.8}$$

where C_i and M_i are molar concentrations and molecular weights, respectively. The overall gas phase molar concentration is related to the local temperature and pressure

by the ideal gas law as follows

$$\sum_{i=1}^{3} C_i + C_{st} = \frac{p}{RT_g} \tag{4.9}$$

The overall mass balance for the solid phase is given by

$$\frac{d}{dz}\left(\phi_s U_s\right) = \Gamma_s \tag{4.10}$$

where the term ϕ_s and Γ_s are listed in Table 4.2,

Table 4.2 Meaning of ϕ_s and Γ_s in Equation 4.10

Species	ϕ_s	Γ_s
Solid phase overall	$\alpha_c\rho_c + \alpha_s\rho_s$	$r_3 + r_5$
Coke component	$\alpha_c\rho_c$	$r_3 + r_5$
Catalyst component	$\alpha_s\rho_s$	0

The overall mass balance is the sum of all component balances, so only two of the three equations in Equation 4.10 are independent. Also, the volume fractions of catalyst (α_s), coke (α_c) and gas (α_g) are constrained by

$$\alpha_s + \alpha_g + \alpha_c = 1 \tag{4.11}$$

The overall momentum balances for the gas and solid phases, respectively, take the form

$$\frac{d}{dz}\left(\alpha_g\rho_g U_g^2\right) = -\alpha_g\rho_g g - \frac{dp}{dz} - f_D \tag{4.12}$$

$$\frac{d}{dz}\left[\left(\alpha_s\rho_s + \alpha_c\rho_c\right)U_s^2\right] = -\left(\alpha_s\rho_s + \alpha_c\rho_c\right)g + f_D - f_C \tag{4.13}$$

where the drag force per unit volume, f_D, is expressed by the modified Richardson-Zaki equation [84],

$$f_D = \xi_1 \cdot \frac{18\mu\alpha_s}{d_s^2\alpha_g^{(n_{RZ}-2)}}(U_g - U_s) \tag{4.14}$$

The empirical Richardson-Zaki index (n_{RZ}) can be correlated with d_s/D and particle Reynolds number [69]. The term of collision force per unit volume is of the form from a semi-empirical model [84],

$$f_C = (1 - \xi_2\xi_3)\, f_D - (1 - \xi_3)\, \alpha_s \rho_s g \tag{4.15}$$

where the correction factors ξ_1 in Equation 4.14 is introduced to account for pair particle wake effect on drag force, while ξ_2 and ξ_3 in Equation 4.15 are introduced to account for energy dissipation partition effects by collisions, which are expressed in Table 4.3,

Table 4.3 Correction Factors ξ_1, ξ_2 and ξ_3 in Equations 4.14 and 4.15

Correction factor	Formula	Reference
ξ_1	$1 - (1 - A)\exp\left[B \cdot \left(\sqrt[3]{\frac{\pi}{6\alpha_s}} - 1\right)\right]$	[86]
ξ_2	$1 - \exp\left[-\left(\frac{\alpha_s + 0.2}{\alpha_{sc}}\right)^2\right]$	[84]
ξ_3	$\frac{0.3}{\pi}\tan^{-1}(26 - 100\alpha_s) + 0.15$	[84]

Here A and B are empirical coefficients determined by a correlation that is related to the local particle Reynolds number [86], and α_{sc} is a critical solid volume fraction that characterizes the transition from dense transport to dilute transport. Set that $\alpha_{sc} = 0.18$ as it is typically between 0.15 and 0.2.

Since all catalytic reactions occur on the catalyst particles, the reaction heat is assumed to be associated with the particles only. The heat transfer between gas and solids is assumed to be governed by the convection of their relative motion and temperature difference. Thus, the overall energy balance for the gas and solid phases is, respectively, given as

$$\frac{d}{dz}\left(\alpha_g \rho_g U_g c_{pg} T_g\right) = h\,(T_s - T_g)\,\pi d^2 n_s \tag{4.16}$$

$$\frac{d}{dz}\left[\left(\alpha_c\rho_c c_{pc}+\alpha_s\rho_s c_{ps}\right)U_s T_s\right]=-\sum_{i=1}^{5} r_i\Delta H_i-h\left(T_s-T_g\right)\pi d^2 n_s \tag{4.17}$$

The effective heat transfer coefficient between gas and solid phase is determined by the following empirical correlation

$$Nu=0.02\,\mathrm{Re}_p^{1/2}\,\mathrm{Pr}^{1/3} \tag{4.18}$$

In summary, the above development leads to 13 independent ODEs with 13 unknowns (α_s, α_g, α_c, U_s, U_g, p, ρ_g, C_1, C_2, C_3, C_{st}, T_g, T_s), thus a closure is reached. These coupled first-order ODEs can be easily solved numerically, such as by using the Runge-Kutta 5^{th}-order method in this study. The required initial (or inlet) conditions are provided by the output of the feed injection model as described in the following section.

4.3 Modeling of Feed Injection Zone

Building on the previous modeling of two round nozzles [60] and four square nozzles [59], here four fan-shaped nozzles with large aspect ratios are investigated. As Figure 4.2 shows, the interactions among the four nozzles are far stronger than those considered in earlier studies. A vaporizing and reacting spray will penetrate into the territory of another spray. The flows of gas and catalyst are accelerated by vaporization and cracking, both of which are dominated by droplet-catalyst collision.

The general forms of the mass, momentum, and energy balance equations over a control volume in each phase along the centerline of a single vaporizing ray (denoted as the ξ direction) are of the following form,

$$\frac{d}{d\xi}\left(\alpha_i\rho_i u_i A\phi_i\right)=S_{\phi i}+S_1 \tag{4.19}$$

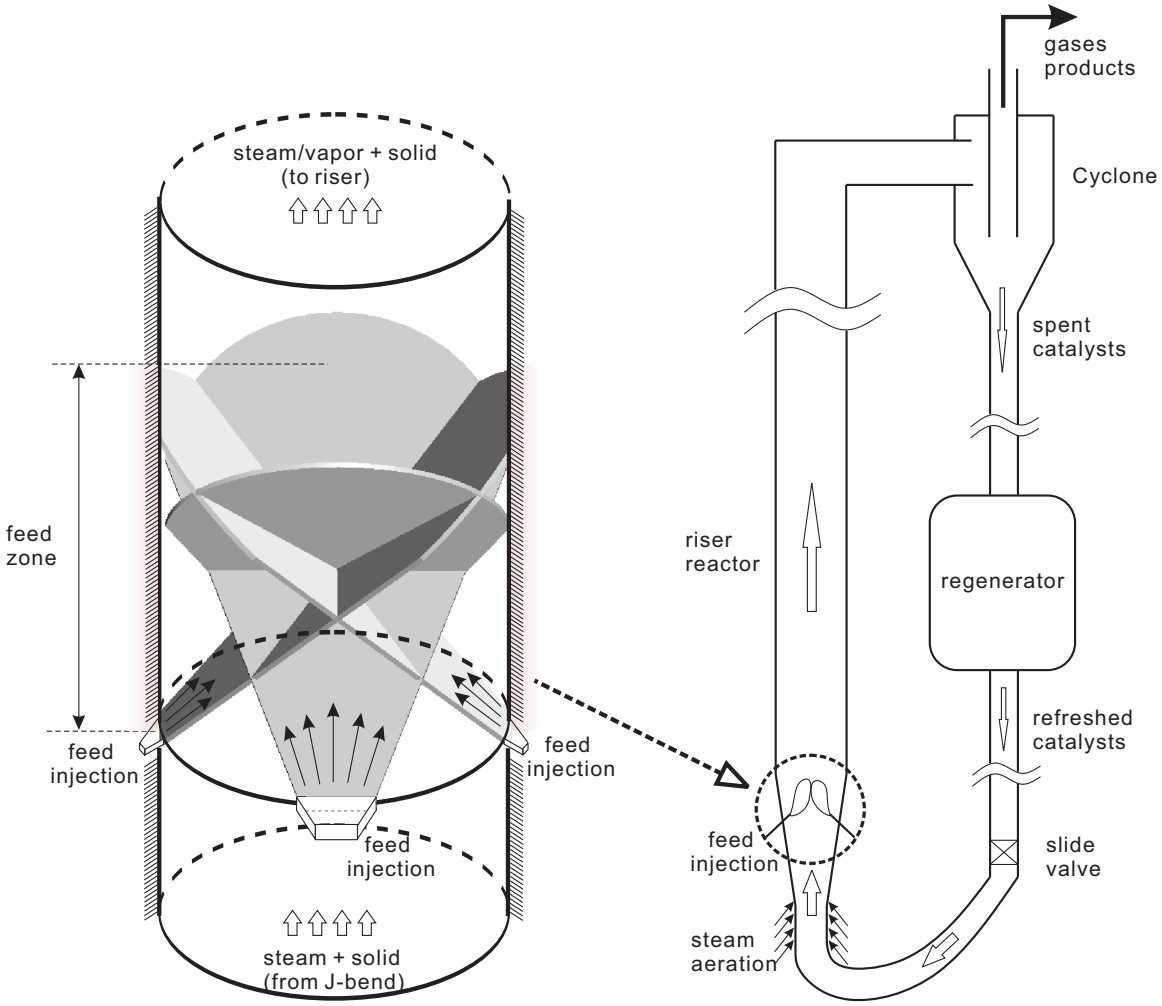

Figure 4.2 Liquid feed injection zone in an FCC riser reactor.

where the index i takes on the values g, d, and s, corresponding to the gas, liquid (droplet), and solid phases, respectively. The constraint set forth in Equation 4.11 also holds in this zone. The expressions for ϕi and the source terms $S_{\phi i}$ and S_1 are shown in Table 4.4.

More information on the source terms ($S_{\phi i}$, S_1) and the associated constitutive relations can be found elsewhere [59]. Thus, the single spray model reaches a closure with ten independent equations and ten unknowns (d_d, α_s, α_g, α_d, u_s, u_g, u_d, T_g, T_d, T_s).

Table 4.4 Definitions of ϕ_i and Source Terms in Equation 4.19

Phase	Equation	ϕ_i	$S_{\phi i}$	S_1
Gas	Continuity	1	$\dot{m}_{ge}l - \gamma\alpha_g\rho_g u_g l$	$\dot{m}_v A$
	Momentum	u_g	$\dot{m}_{ge}u_{g\infty}l\cos\theta - \gamma\,\alpha_g\rho_g u_g^2 l$	$\dot{m}_v u_d A - (F_{Dd} + F_{Ds})\,A$
	Energy	$c_{pg}T_g$	$\dot{m}_{ge}lc_{pg}T_\infty - \gamma\alpha_g\rho_g u_g c_{pg}T_g l$	$\dot{m}_v LA + E_{Cs} - E_{Cd} - E_R$
Liquid	Continuity	1	$-\dot{m}_v A$	0
	Momentum	u_d	$-\dot{m}_v u_d A$	$(F_{Dd} - F_{Cds})\,A$
	Energy	$c_{pd}T_d$	$-\dot{m}_v LA$	$E_{Cds} + E_{Cd}$
Solid	Continuity	1	$\dot{m}_{se}l + \dot{m}_{sp}l$	0
	Momentum	u_s	$(\dot{m}_{se}l + \dot{m}_{sp}l)u_{se}\cos\theta$	$(F_{Ds} + F_{Cds})\,A$
	Energy	$c_{ps}T_s$	$(\dot{m}_{se}l + \dot{m}_{sp}l)c_{ps}T_\infty$	$-E_{Cds} - E_{Cs}$

The major difference between the multi-spray and the single-spray models lies in the ambient gas and catalyst flow conditions. For the latter, the flow conditions remain the same for the entire spray coverage, while for each spray in a multi-spray system, the gas and catalyst flow conditions can change due to spray interferences with each other. For instance, as a result of vaporization and cracking, the gas and catalyst flows will change whenever a spray reaches the intersections with an adjacent spray or an opposing spray.

As detailed elsewhere [59], each nozzle spray is divided into multiple rays to account for the overlapping geometry generated by the fan-shaped coverage and injection angle. The single-spray model is adopted for each ray and then the reaction-transport model (presented in the previous section) is used to obtain updated gas-solid conditions (e.g., spray penetration, vaporization, conversion, etc.) for the next section of the spray. The cascade iteration between the spray penetration and the

reaction-transport models provides the state variables (temperature, oil composition, etc.) at the end of feed injection zone.

4.4 Model Validation

Here the commercial data of Derouin et al. (1997, [14]) is used to test the current two-zone model against the traditional homogeneous plug-flow model (TPFM) and a heterogeneous hydrodynamics-reaction coupled model (HRCM, [88]) accounting for gas-catalyst momentum transfer. Table 4.5 lists the operating conditions and hydrocarbon properties. Figure 4.3 shows Derouin et al.'s data, which, to the best of the knowledge, have thus far not been predicted by any model, including the HRCM. The trickiest part is the prediction of the first data point for VGO conversion ($\sim 49\%$ conversion at 3.5m riser height). This says that the first 10% of the riser height provides more than 65% of the total conversion over the entire riser, implying the importance of entrance cracking.

For the four-lump kinetic model, the first-order rate constants provided by Han and Chung (2001, [30]) is used, which are listed in Table 4.6. For consistency purposes, the rate constants for VGO cracking were converted to pseudo-second-order rate constants via appropriate scaling [58].

Figure 4.3 shows the VGO conversion and gasoline yield versus riser height, which are predicted by the above-mentioned models against Derouin et al.s data. As can be seen, the TPFM significantly overestimates both the VGO conversion and gasoline yield, especially in the dilute phase zone. The HRCM predicts the gasoline yield well but underestimates the VGO conversion [88]. By contrast, the two-zone model satisfactorily predicts the VGO conversion and gasoline yield. Of particular significance is the prediction of the fairly high conversion near the riser bottom. After the initial steep rise, the conversion increases slowly in the dilute phase zone.

Table 4.5 FCC Riser Operating Condition and Hydrocarbon Properties

Operation Parameters and Properties	Values
Catalyst feed rate (kg/s-m2)	470
VGO feed rate (kg/s-m2)/CTO ratio	85/5.5
Inlet temperature of VGO feed (K)	650
Inlet temperature of catalyst (K)	960
Riser diameter (m)	1
Riser height (m)	35
Catalyst diameter (μm)	75
Inlet riser pressure (atm)	3.15
Catalyst density (kg/m3)	1800
Gas specific heat (J/kg-K)	3299
Liquid specific heat (J/kg-K)	2671
Catalyst specific heat (J/kg-K)	1150
Molecular weight of VGO (kg/kmol)	400
Molecular weight of Gasoline (kg/kmol)	100
Molecular weight of Light gases (kg/kmol)	50
Molecular weight of Coke (kg/kmol)	400

Source: [14]

This characteristic behavior, to the best of the knowledge, has hitherto not been satisfactorily predicted.

The product yields (wt%) and unconverted VGO are plotted in Figure 4.4. Note that the gas products, though small in weight, account for a large proportion of molar flow.

Figure 4.5 shows the axial temperature profiles of gas and solid phases along the riser, comparing with those calculated from the HRCM and TPFM. The latter

Table 4.6 Heats of Reaction, Pre-Exponential Factor, and Activation Energy

Sub-Cracking Reaction	ΔH_i (kJ/kg)	k_{i0} (g oil/(s g cat))	E_{ai} (kJ/kmol)
VGO to Gasoline	195	1457.5	57359
VGO to Light Gases	670	127.59	52754
VGO to Coke	745	1.98	31830
Gasoline to Light Gases	530	256.81	65733
Gasoline to Coke	690	0.022	66570

Source: [30]

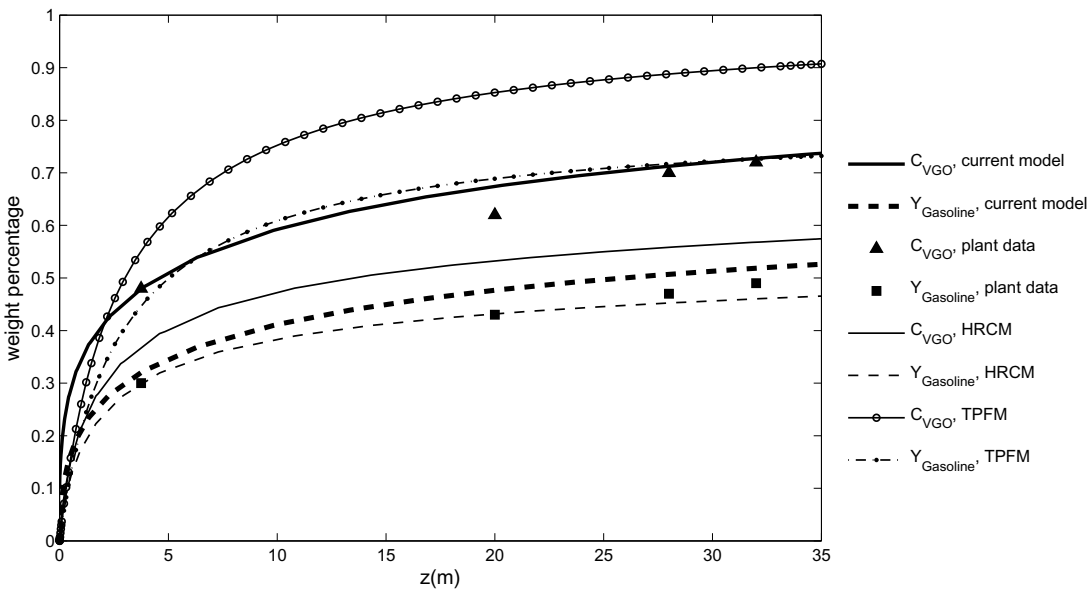

Figure 4.3 Gasoline yield and VGO conversion.

assumes that both gas and solid phases have the same temperature. The heat transfer rate between gas and solid phase is high initially when the temperature difference is big. As the two phases mix together and flow upward, with the involvement of cracking endothermicity, the temperatures of solid phase and gas phase eventually approach to equilibrium. An important point here is that the heat transfer rate is not instantaneously fast, which was a common but untested assumption in many

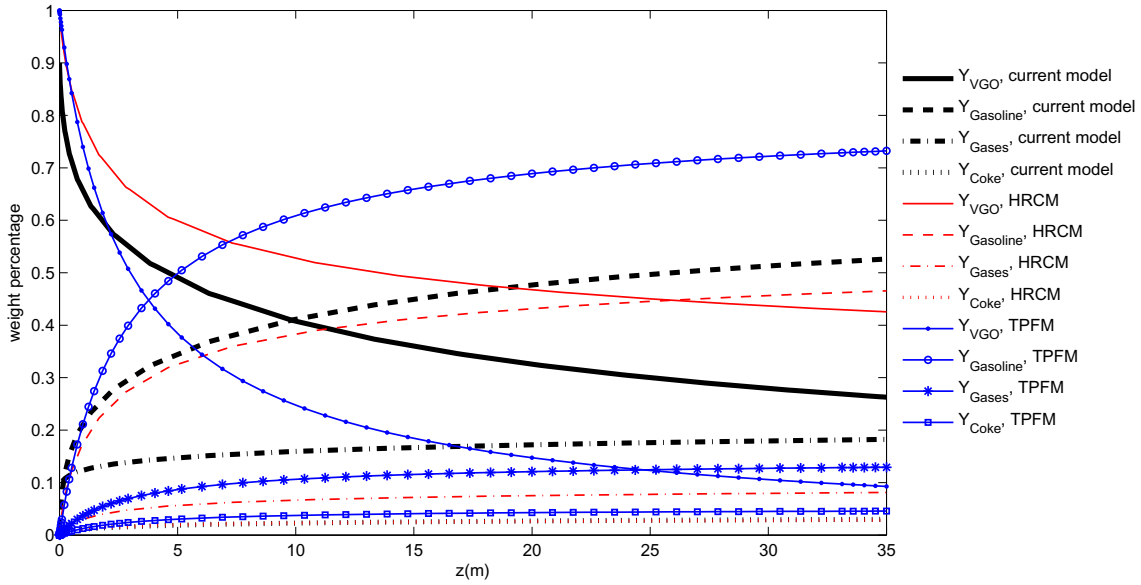

Figure 4.4 Weight fraction yields with comparison to HRCM and TPFM.

literature models. Figure 4.5 indicates that there exists a significant temperature difference between the gas and catalyst near the riser bottom (say, less than 5m height).

Figure 4.6 contrasts nominal CTO with local CTO. In a riser reactor, from dense- to dilute-phase regimes, the CTO cannot be constant but decreases precipitately over a short distance above the riser inlet. This is one of the reasons why the VGO conversion increases rather sluggishly after the dense-phase zone. The high VGO conversion predicted by the TPFM is mainly the result of using the nominal CTO throughout the entire riser.

Temperature and CTO are the most important FCC intensity factors. Qualitatively, they behave similarly, as revealed by Figures 4.5 and 4.6. Both are nearly constant except in a narrow entrance region. Inside this entrance zone, cracking intensity is high and changes rapidly, resulting in a sharp rise in VGO conversion. Outside the entrance zone, cracking intensity is low and becomes slowly varying, giving rise to a sluggish increase in conversion. This depicts an inherent two-zone character of the

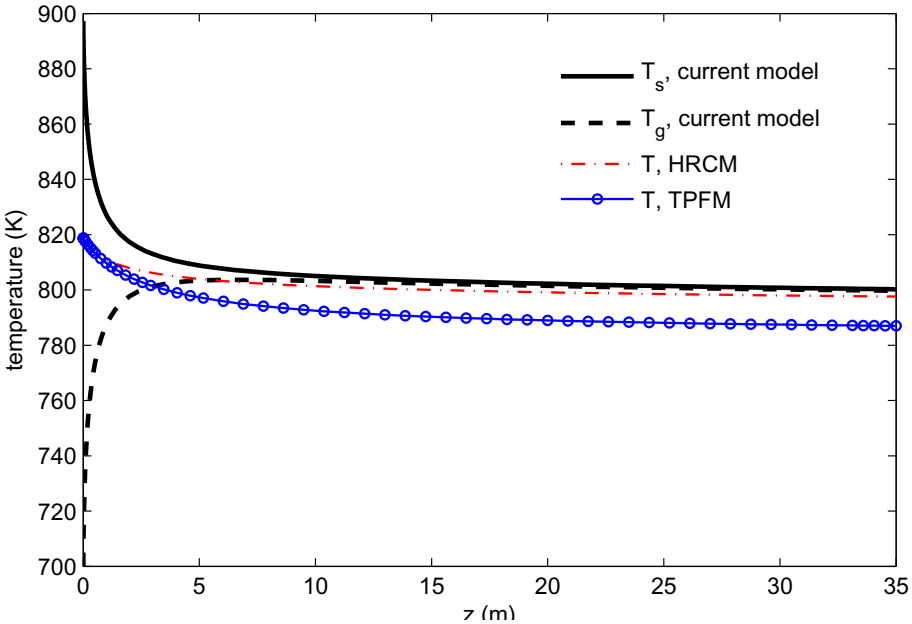

Figure 4.5 Temperature of gas and solid phase along riser.

FCC riser and speaks of the importance of developing a simple, practical model that captures the essence of the interactions between the two zones.

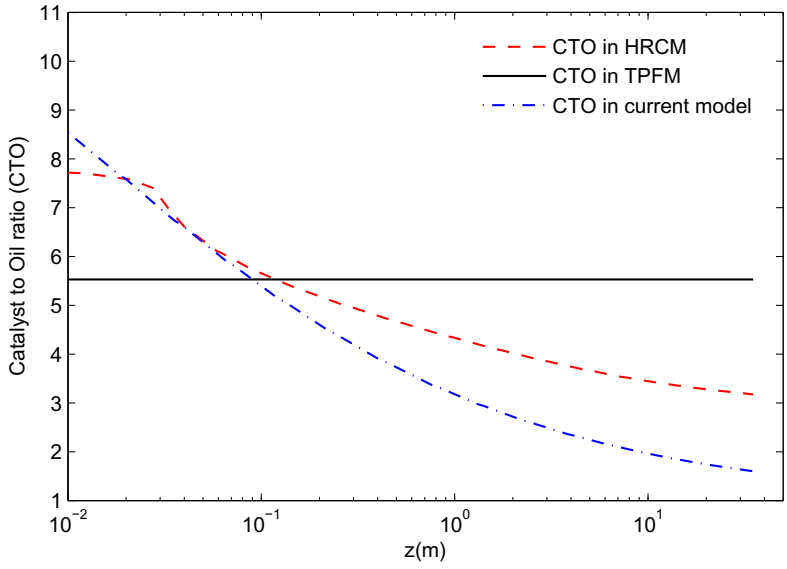

Figure 4.6 Local and nominal CTO.

The hydrodynamic characteristics of the riser transport is shown in Figures 4.7 to 4.9, respectively in terms of the phase velocities, pressure and phase volumetric fractions, in which the predictions from the present two-zone model are compared with those from the HRCM. Both gas and solid velocities increase along the reactor height due to the cracking-induced volume expansion. The increase at the bottom part of the riser is much larger than that in the rest of the riser. It is noted that the two-zone model gives a lower velocity than the HRCM. This is mainly due to the non-thermal equilibrium consideration taken in the two-zone model, which leads to a much lower temperature of vapor and hence higher vapor density in the entrance region. This lower velocity of vapor, compared to that from HRCM, results in a less drag force between the gas and catalyst and hence smaller pressure drop, as shown in Figure 4.8.

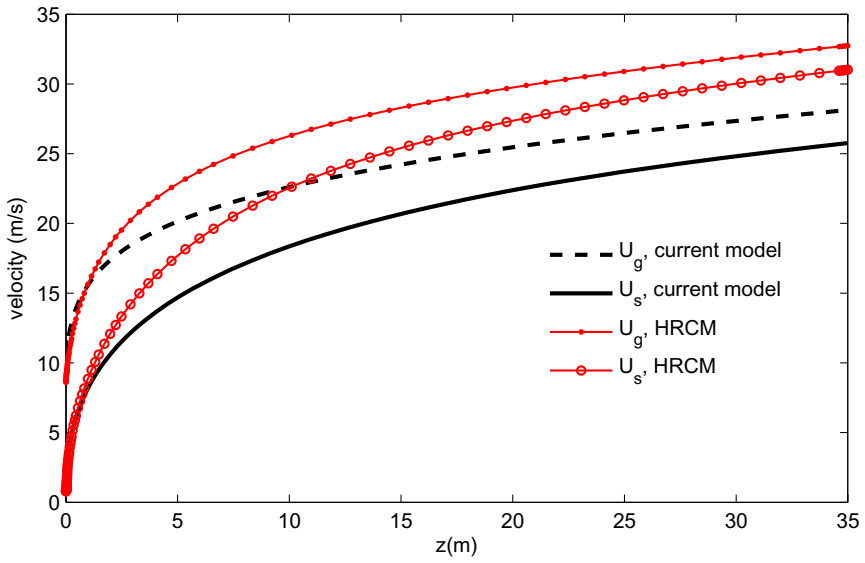

Figure 4.7 Velocity of solid and gas phase along the riser.

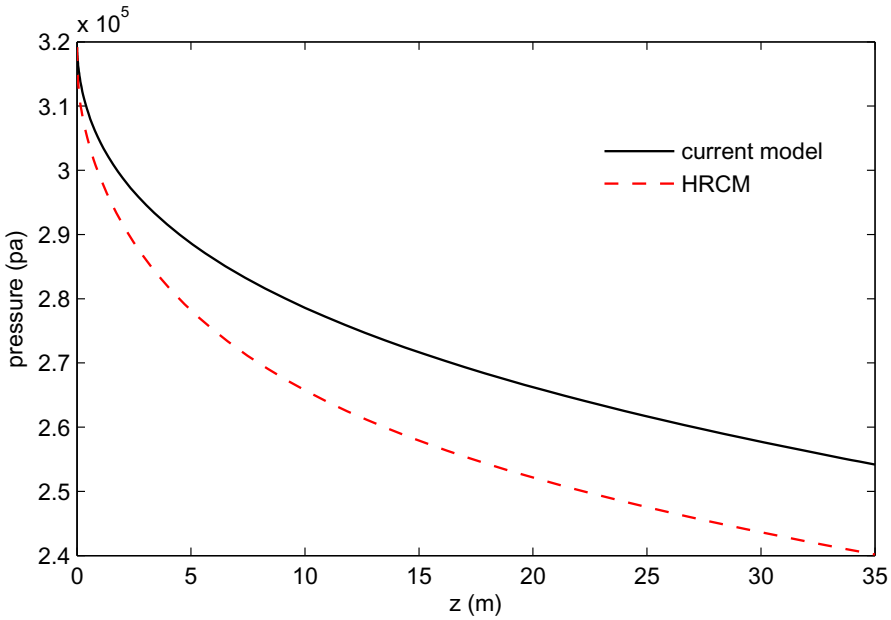

Figure 4.8 Pressure drop along riser.

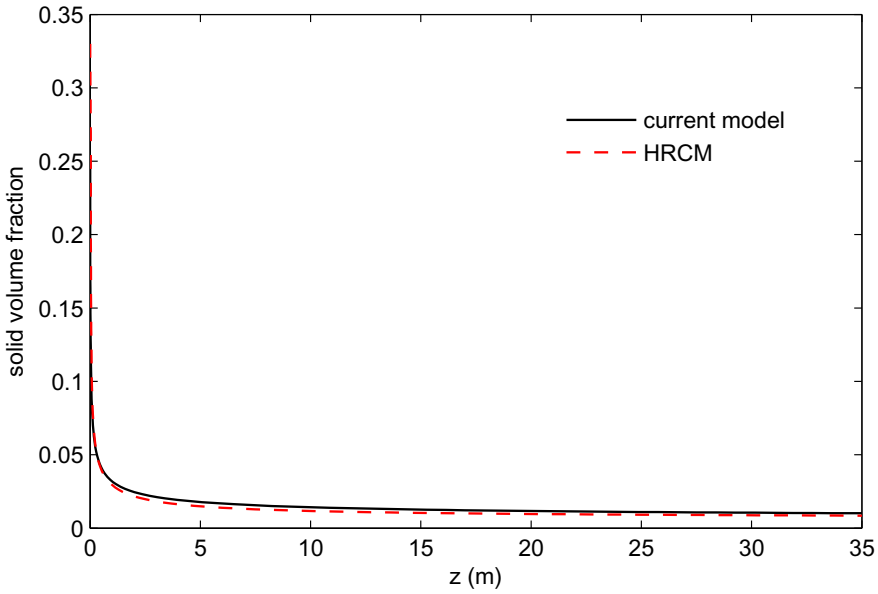

Figure 4.9 Catalyst volume fraction along riser.

4.4.1 Parametric Studies

This section presents the results of a parametric study on the effect of the inlet CTO ratio and catalyst inlet temperature. Figures 4.10 to 4.13 illustrate, respectively, the

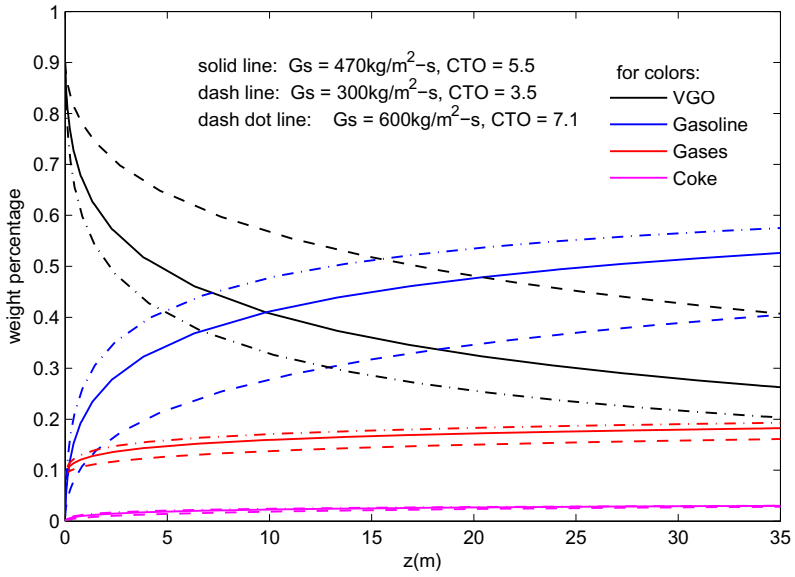

Figure 4.10 Effects of CTO on product yields and VGO conversion.

effects of inlet CTO on product yields, VGO conversion, temperature, pressure and catalyst coke content. They all show the expected results. The same is true of the effect of catalyst inlet temperature, as illustrated in Figures 4.14 to 4.16.

4.4.2 Selectivity and Conversion

The selectivities toward different products depend on intensity factors such as inlet CTO and catalyst temperature. Figure 4.17 plots product selectivities versus changes in VGO conversion via CTO adjustments. By contrast, Figure 4.18 shows a similar plot in which the variation of conversion is achieved via adjustments in catalyst inlet temperature. As can be seen, the two intensity factors give rise to very different selectivity-conversion behaviors. Thus, the two-zone model can be used to find the optimum operating conditions for maximizing the yield of the most desirable products.

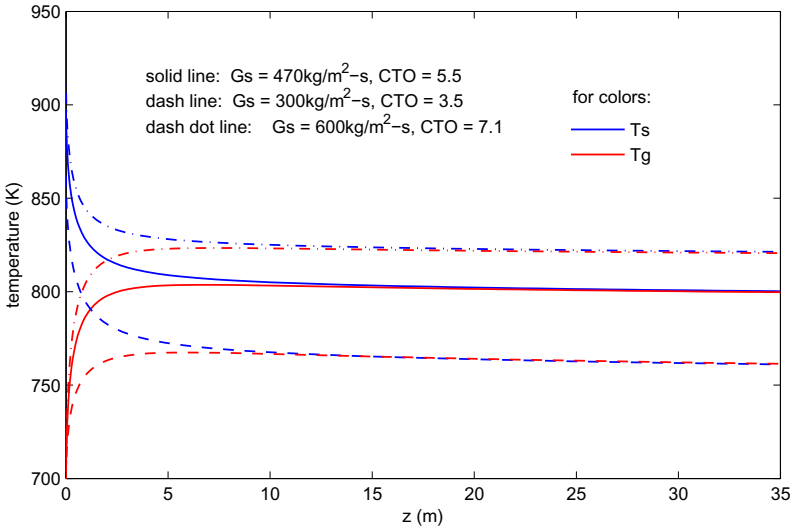

Figure 4.11 Effects of CTO on temperature profiles of gas and catalyst.

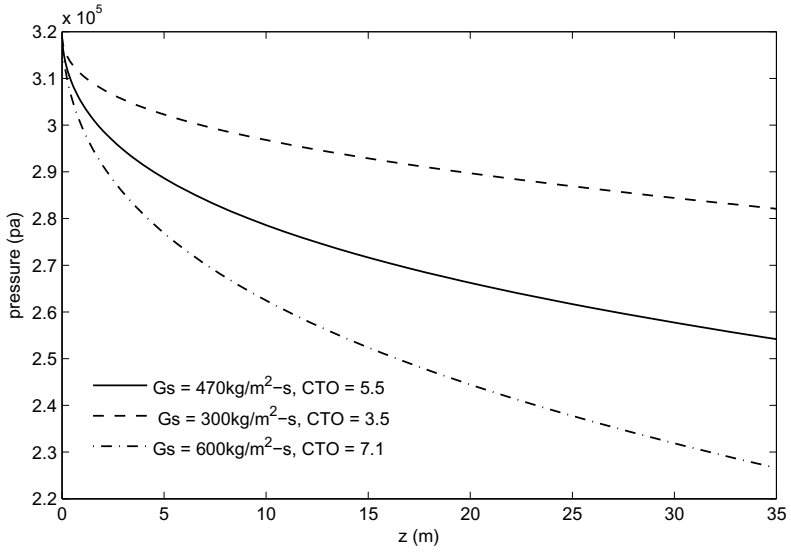

Figure 4.12 Effects of CTO on pressure along the riser.

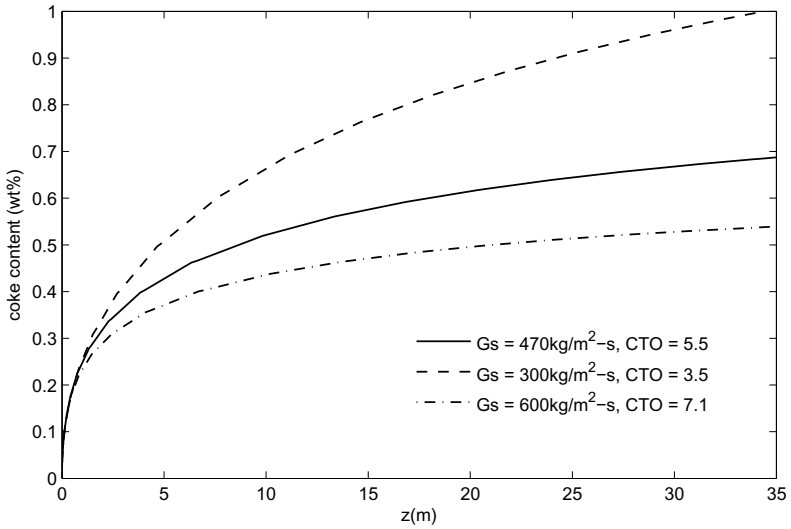

Figure 4.13 Effects of CTO on catalyst coke content.

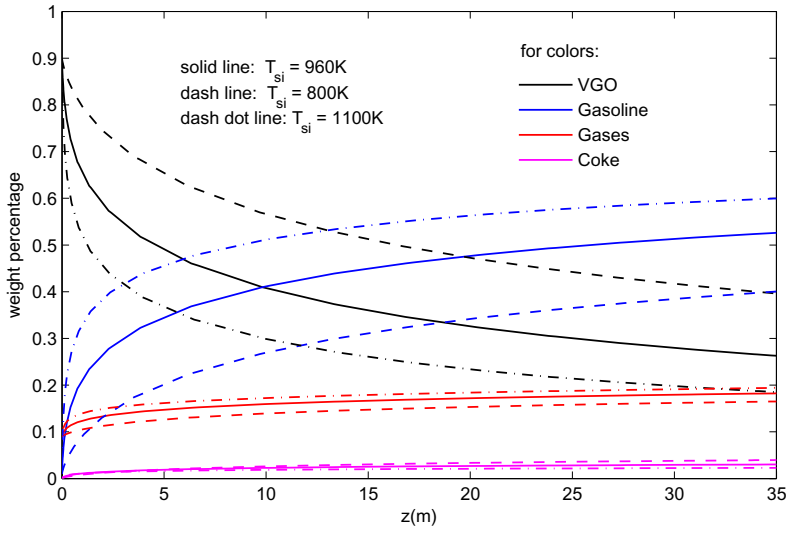

Figure 4.14 Effect of catalyst inlet temperature on product yields and VGO conversion.

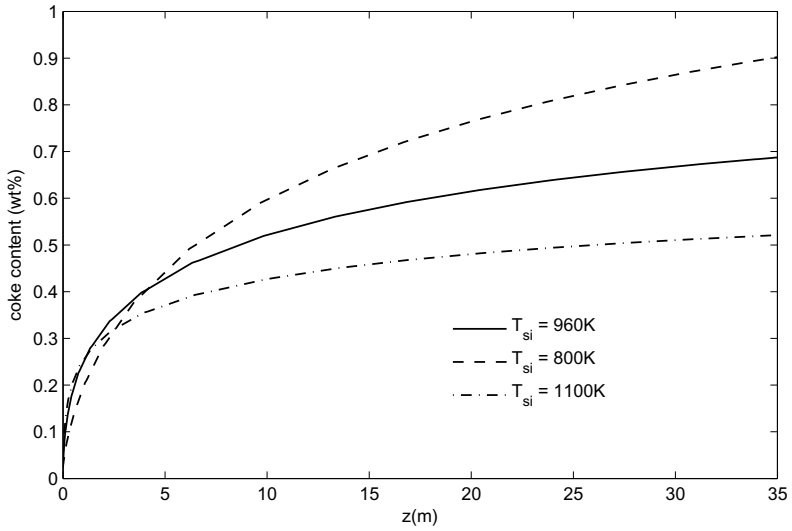

Figure 4.15 Effect of catalyst inlet temperature on catalyst coke content.

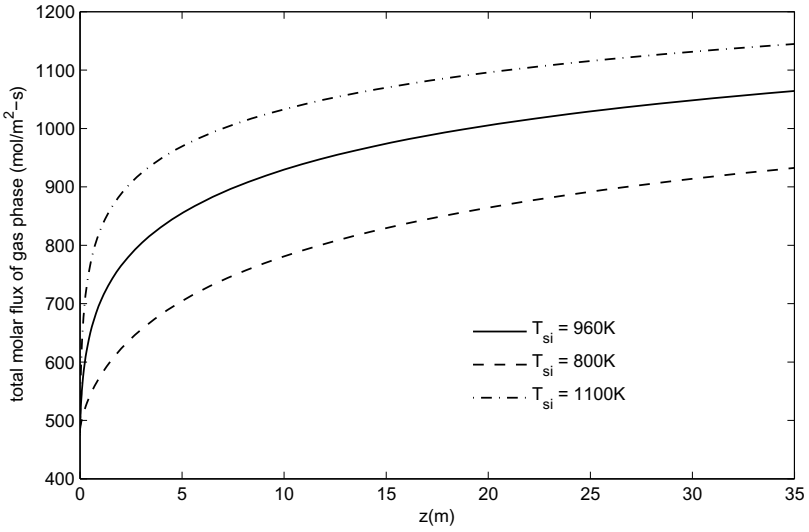

Figure 4.16 Effect of catalyst inlet temperature on total molar flux of gas phase.

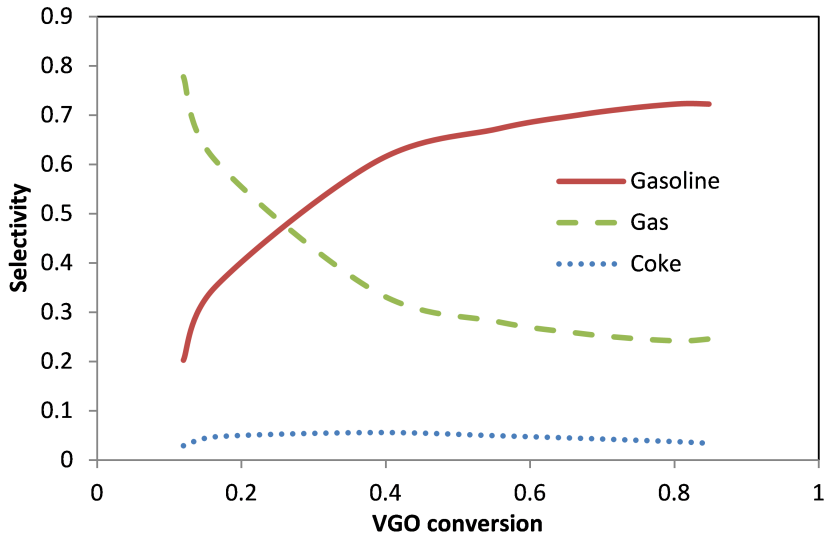

Figure 4.17 Effect of Conversion on product selectivities via CTO adjustments.

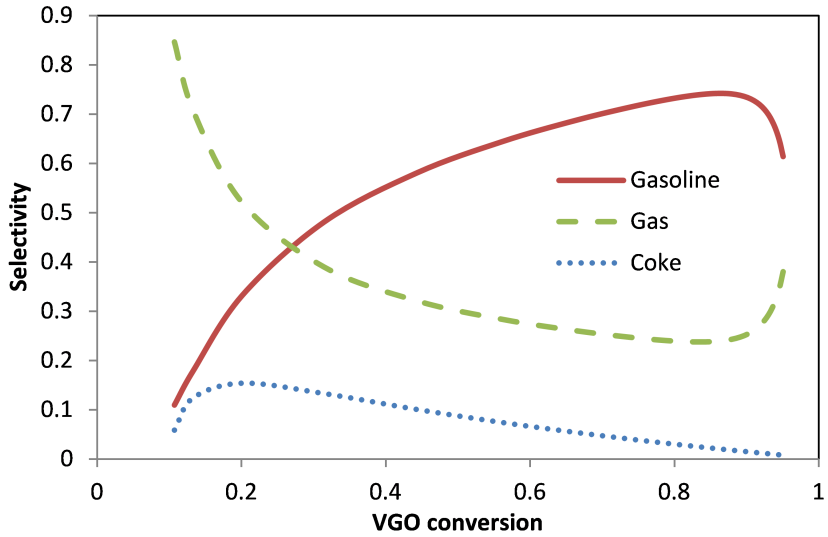

Figure 4.18 Effect of conversion on product selectivities via adjustments in catalyst inlet temperature.

4.5 Concluding Remarks

The view has been that an attempt should be made to develop a modeling approach that strikes an optimum balance between the kinetics- and CFD-dominated approaches. Moreover, the weight of evidence has indicated that modeling of entrance cracking should be an integral part of any FCC riser model, as borne out by

Derouin et al.s commercial data that have baffled many FCC modelers. With todays remarkably active catalysts and high-efficiency atomizers, it is hardly surprising that significant cracking occurs in the feed injection zone where temperature and catalyst activity/concentration are highest. Despite this, relatively little attention has been paid to modeling of the interplay of reaction and interfacial transfer in the feed injection zone.

It has been shown that the underlying physics of the FCC process is such that it has an inherent two-zone character. The two-zone model developed in this work explains and predicts Derouin et al.'s data. This result demonstrates that FCC process, highly complex as it may seem, is amenable to a quantitative treatment with a computationally simple model. While a coarse four-lump kinetic model is used in this study, the two-zone model can easily admit a composition-based kinetic model. The present work provides a basis for further exploitation of the two-zone modeling approach.

CHAPTER 5

CONTINUOUS MODEL OF AXIAL AND RADIAL FLOW STRUCTURE IN GAS-SOLIDS RISERS

5.1 Introduction

Gas-solids risers are widely adopted for transportation and reactions in many industrial applications such as fluid catalytic cracking (FCC) in petroleum refinery processes. Despite of their widespread applications, the dynamics of gas-solids transport of risers is still far away from being thoroughly understood and theoretically described, which partly due to complex gas-solids flow structure, and partly due to difficulties in measurement of local transport properties in the dense gas-solid flows. Typically in FCC riser reactors, the axial and radial non-uniformity of gas-solids flow has significant influence on the hydrodynamic transport, heat and mass transfer, and reaction rates. A better understanding of the flow structure and hydrodynamics of gas-solid in risers can be very important to an improved product yield or more stabilized operation in related industrial applications.

The gas-solids flow structure in risers exhibit strong heterogeneous characteristics in both axial and radial directions. The heterogeneity in riser flow may be categorized into the phase heterogeneity and hydrodynamic heterogeneity. The phase heterogeneity refers to the non-uniform distribution of a mixture of solids in form of individual particles, clusters and agglomerates, while the hydrodynamic heterogeneity refers to the non-uniform distribution of gas-solids transport properties both in axial and radial directions. The axial non-uniformity of gas-solids transport is mainly due to the phase acceleration and inter-particle collision, while the radial non-uniformity is mainly due to the riser wall effect, which causes the gas stagnation as well as the radial mass and momentum balances between the collision-induced diffusion and the

turbulent convection of solids. The axial nonuniform distribution of solids volume fractions in risers is characterized as an "S" shape with dense phase regime at bottom, dilute phase regime at top and intermediate acceleration/transition regime [49, 3, 68, 57, 82], while the radial nonuniform distribution of gas-solids transport properties in riser flow is characterized as core-annulus (wall) regime with dilute up-flow of solids in core regime and dense down-flow of solids in wall regime [38], or a double ring core-annulus-wall three-zone flow structure under some operational conditions [16]. The most significant hydrodynamic properties include the local catalyst concentration, the back flow carrying spent catalysts from wall region and the pressure drop. Besides temperature, the local catalytic reaction rate depends on the local catalyst-to-oil ratio (CTO), the mixed fractions of fresh catalysts and spent catalysts and the pressure.

To improve the performance of the existing FCC processes and to facilitate new applications, the understanding on development of nonuniform gas-solids flow structure in risers is now become subject of interest for many researchers. Numerous research efforts have been made to study the gas-solids flow structure in gas-solids risers both by conducting experiments on laboratory scale risers and development of theoretical models. Previous modeling of riser flow can be mainly categorized into three groups [32]: (1) the models that predict the axial variation of the solid suspension density, but not the radial variation; (2) the models that predict the radial variation and the high average slip velocities by assuming two or more regions, such as core-annulus or clustering annulus flow models; and (3) the models which are based on the numerical modeling of the conservation equations for mass, momentum, and energy for gas and solid phases.

In the first group, literature modeling for axial non-uniform distribution of gas-solids transport properties are based on assumption of a uniform distribution phase properties over the cross section. In such modeling approach, the area and

mass fluxes of gas and solid phases remains constant along the riser [53, 8, 52, 27, 91]. The drawback of these 1-D axial models is that it fails to account for the back-flow of solids in the wall region, which may not be adequate to describe the hydrodynamics of gas-solids riser flow. The hydrodynamic characteristics of gas-solids flow in core and annulus (wall) regimes are strikingly different; consequently, it may be not physical to combine the transport properties of two regions as a uniform flow. This could lead to large bias on reaction rate since the back-flow carries spent catalyst rather than fresh catalyst. Besides, the existence of back-flow would change the cross-sectional flow pattern, such as local pressure, temperature, velocity and the CTO, all of which are key factors of reaction rate to FCC riser reactor.

Modeling efforts have also been made time to time to study the axial and radial nonuniform gas-solid flow structure in risers as classified in second group. Some literature model the radial non-uniformity of gas-solid transport in riser flow [70] based on empirical correlations for radial transport of phases, which are limited by operation range of risers, types of solid particles and geometry of CFB risers. Some other studies consider radial non-uniform gas-solid flow structure in risers by proposing two-regime modeling [5, 67, 41, 72], which assumes that the particle flow in the riser consists of dilute up-flow suspension of solids in the center of riser (core regime) and dense down-flow suspension of the particles adjacent to the riser wall (annulus or film regime). In such modelings, the core and wall regime boundary and back-flow are predefined, and the radial transport of the particles are not truly based on the governing mechanisms but built-in transport coefficients and semi-empirical correlations. The predicted axial distributions of transport properties, especially for pressure gradient, have not yet been validated.

As in third group, current numerical modeling (e.g., CFD simulation), which based on the partial differential equations for conservation of mass, momentum and energy of gas and solid phases, is losing physical base as well (collision force in dense

particle flow, for example). In the dense regime of a gas-solid flow, the specially slow solids acceleration (even with high velocity slip ratio to gas phase) is result of the particle-particle collisions, which damp the solid momentum before it reaches higher velocity. This collision force can be related to local particle drag force, producing local non-uniformity.

In sum, while the literature on gas-solids transport in riser is vast, very little general valid and physically based equations/mechanisms for both radial and axial non-uniformity have been proposed in the literature. And very little modeling work has been done on continuous modeling of axial and radial distribution of gas-solids transport properties in riser flows. The governing mechanisms are poorly understood, especially in the dense transport region, where catalyst acceleration has been very much damped by non-equilibrium inter-particle collisions.

Against the above backdrops, this work aims to propose a continuous modeling theory to reasonably predict both axial and radial distributions of transport properties along a riser, from the end of the feed vaporization zone (or riser inlet) to the top exit (referring to Figure 5.2). According to continuous modeling theory, cross-section average axial distribution of the phases can be expressed as differential-integral equations providing the radial non-uniform distribution of transport properties for each phase at any cross-section of the risers. The 2nd order polynomial (parabolic) representation, among one of the simplest dimensionless correlations, has been validated against many experimental measurements from published literature. A mechanistic model for solids radial transport based on the turbulent convective and diffusive radial transportation balance across the core-anulus boundary is proposed to physically characterize the formation of radial nonuniform gas-solids flow structure. This proposed modeling approach, being able to identify the motions of down-flow of solids in the wall region and the upward flow of solids in the core regime, eliminates empirical determinations of some important transport properties such as

core-wall boundary and back-mixing ratio. Rather these transport properties become flow-coupled and model calculated.

5.2 Model Development

Consider a steady, isothermal gas-solids riser as shown in Figure 5.1. Based on the dynamics of the solid phase, the flow structure along the riser can be divided into three regimes dense phase regime, acceleration phase regime and dilute phase regime, respectively. While radially, there are always two typical regimes, dilute core and dense annulus regimes, respectively, due to wall effect (non-slip condition of gas phase at wall, thus particles nearby wall are unsupported and may goes backward). A sketch of radial and axial transportation trait of gas-solid phase is indicated in Figure 5.1.

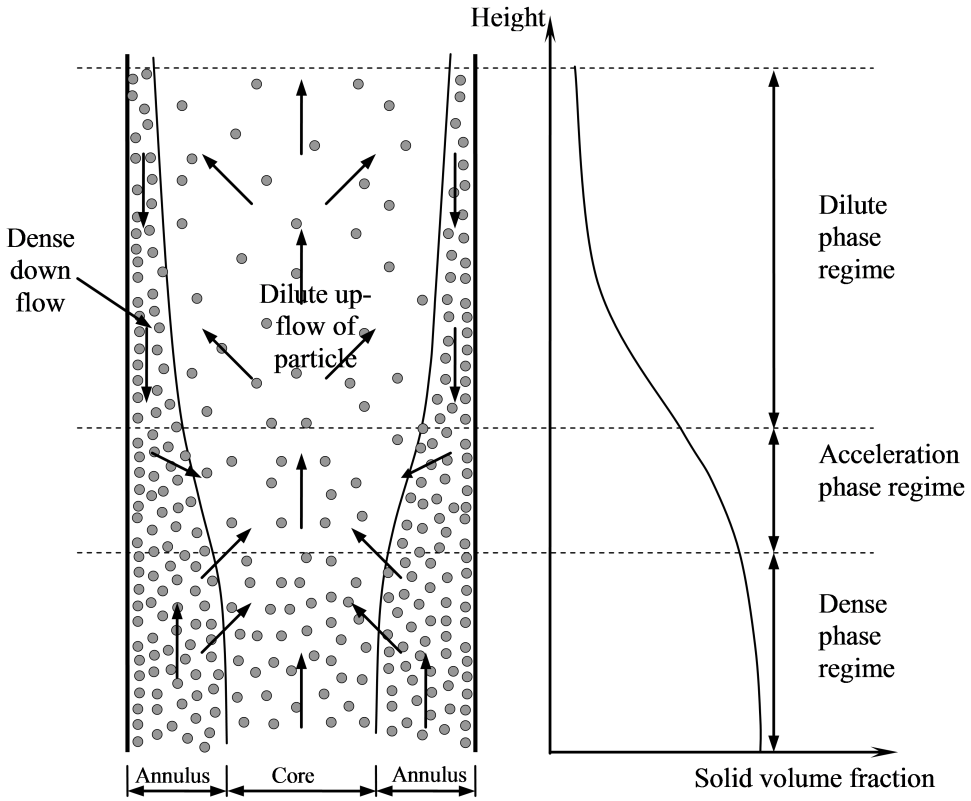

Figure 5.1 Schematic representation of core-annulus riser regimes with radial transport mechanism and flow regimes along of riser.

To develop an analytic model to capture the dominant features of the system, the following assumptions are made. (1) The effect of solid deceleration at the top of the riser and the intensive turbulent mixing regime at the inlet of the risers are ignored. (2) The gas phase follows the ideal gas law. (3) Conical effect are neglected, which means the cross section area keeps constant along the riser. (4) The riser flow is assumed to be axisymmetric. Based on above assumptions, a schematic diagram of radial heterogeneous gas-solids flow structure and the computation domain is shown in Figure 5.2.

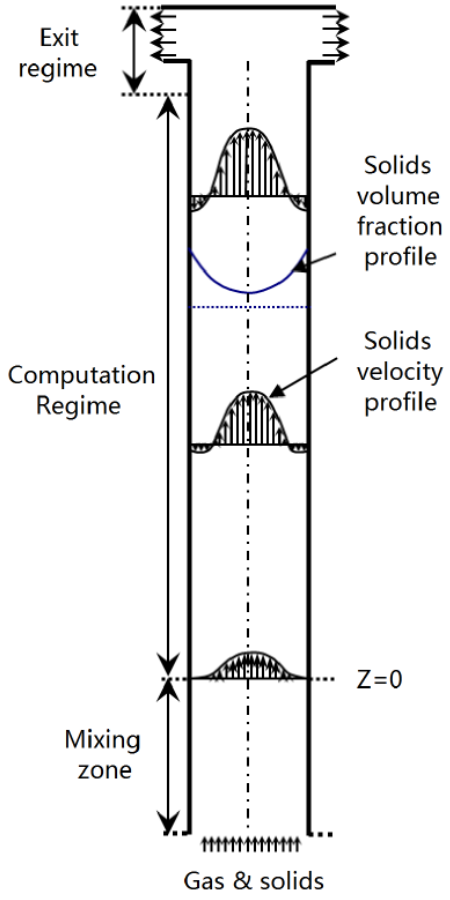

Figure 5.2 Radial heterogeneous flow structure and computation domain.

5.2.1 Hydrodynamic Model for Axial Phase Distribution

With above simplifying assumptions, mass balance of gas and solid flow in its dominant (axial) direction can be expressed as,

$$\frac{d}{dz}\left(\int \alpha_g \rho_g U_g dA\right) = 0 \tag{5.1}$$

$$\frac{d}{dz}\left(\int \alpha_s \rho_s U_s dA\right) = 0 \tag{5.2}$$

Similarly, the momentum balance of the gas and solid phase can be given by,

$$\frac{d}{dz}\left(\int \alpha_g \rho_g U_g^2 dA\right) = -\int \alpha_g \rho_g g dA - \int \frac{dp}{dz} dA - \int f_D dA \tag{5.3}$$

$$\frac{d}{dz}\left(\int \alpha_s \rho_s U_s^2 dA\right) = -\int \alpha_s \rho_s g dA + \int f_D dA - \int f_C dA \tag{5.4}$$

The drag and collision forces per unit volume(f_D, f_C) in Equations 5.3 and 5.4 varies along the radial locations depending on local hydrodynamic properties (α, U) of both phases. Specifically, the drag force per unit volume, f_D, is expressed by modified Richardson-Zaki Equation [84],

$$f_D = \xi_1 \cdot \frac{18\mu\alpha_s}{d_s^2 \alpha_g^{(n_{RZ}-2)}}(U_g - U_s) \tag{5.5}$$

The empirical Richardson–Zaki index (n_{RZ}) can be correlated to d_s/D and particle Reynolds number [69] , which is expressed as,

$$n_{RZ} = \begin{cases} 4.65 + 19.5\dfrac{d_p}{D} & Re_p < 0.2 \\ \left(4.35 + 17.5\dfrac{d_p}{D}\right) \mathrm{Re}_p{}^{-0.03} & 0.2 < Re_p < 1 \\ \left(4.45 + 18\dfrac{d_p}{D}\right) \mathrm{Re}_p{}^{-0.1} & 1 < R_e p < 200 \\ 4.45 \mathrm{Re}_p{}^{-0.1} & 200 < Re_p < 500 \\ 2.39 & Re_p > 500 \end{cases} \tag{5.6}$$

The inter-particle collision force is dues to the inelastic normal compression and rebounding, sliding, non-sliding micro-slip and rolling effects among particles during the transport. The "S" shape axial distribution of solid volume concentration [44] indicates low solid velocity or high slip velocity in the dense phase regime, which is mainly due to energy dissipation by inter-particle collision. The order of magnitude of collision force should be in the same order of magnitude as drag force in the dense phase regime and its reaches almost zero in the dilute phase regime. The formulation of the collision force from the basic principles is very complicated due to normal, tangential and oblique collision among the particles. In this study, the phenomenological semi-empirical model for collision force per unit volume as a function of drag force [84] is adopted,

$$f_C = (1 - \xi_2\xi_3)\, f_D - (1 - \xi_3)\, \alpha_s \rho_s g \tag{5.7}$$

where the correction factors ξ_1 in Equation 5.5 is introduced to account for pair particle wake effect on drag force, while ξ_2 and ξ_3 in Equation 5.7 are introduced to account for energy dissipation partition effects by collisions, which are explained in Table 4.3 in Chapter 4.

The volume fraction of gas and solid phase are constrained by

$$\alpha_g + \alpha_s = 1 \tag{5.8}$$

The gas phase density, following the ideal gas law can be written as

$$\rho_g = \frac{p}{R_g T} \tag{5.9}$$

It is noticed that, although there may be slight fluctuations of pressure in radial direction at any arbitrary cross-section, but the pressure gradient in radial direction is much less than that along the riser. Thus, it is safe to assume the pressure distribution

is uniform over cross-section of the riser at any axial location, which applies to gas density as well.

The integral terms in the Equations 5.1 to 5.4 represent the overall cross-sectioned transport properties of the phases, where α_g, U_g, α_s, and U_s are the local volume fraction, velocity of gas and solids phase, respectively. For 1-D (axial) modeling approach with uniform radial distribution assumption [84, 88, 37], the local values of these phase transport properties equals to cross-sectional averaged values, which simplifies the integral terms to be easily expressed explicitly and reaches problem closure. Yet the heterogeneous modeling with non-uniform property profiles requires predefined formula for further integration.

5.2.2 Modeling of Radial Nonuniform Phase Distribution

The formation of radial heterogeneous gas-solid flow structure in the riser is mainly due to the riser wall effect and dynamic balance between turbulent convection and collision-induced diffusion of particles. This concept requires certain intrinsic mechanisms or correlations of radial distribution for problem closure. The preliminary study shows that, the published experiment data for radial distribution of transport properties of gas-solids in the riser are reasonably fitted by parabolic approximation. Nearly 70 cases of experiment data for radial distribution of transport properties of solid phase from different research groups [56, 81, 42, 57, 63], have been reviewed. Figures 5.3 and 5.4 demonstrate an example of parabolic fit on nondimensional solid velocity and volume fraction data.

Hence, here parabolic approximation for radial distribution of both phase transport properties is adopted. Considering axisymmetric condition in riser, the parabolic radial distribution of phases can be expressed as;

$$\phi(r, z) = c_{\phi 2}(z) \cdot r^2 + c_{\phi 0}(z) \tag{5.10}$$

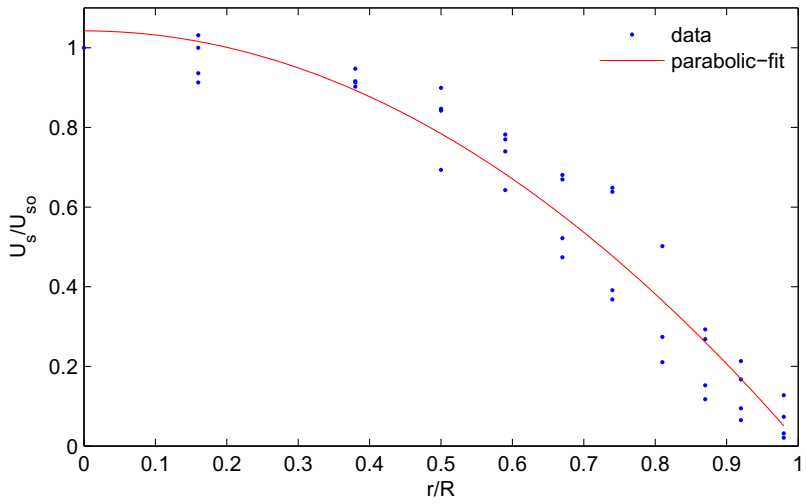

Figure 5.3 Parabolic fitting of radial solid velocity data

Source: [57]

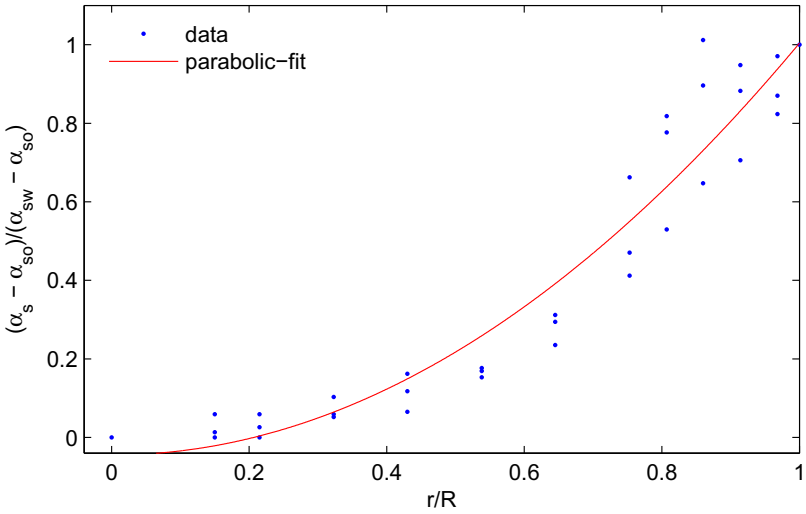

Figure 5.4 Parabolic fitting of radial solid concentration data.

Source: [81]

Here $\phi(r,z)$ can be $U(r,z)$ and $\alpha(r,z)$ for gas and solid phase. The first degree term is vanished when applying the axisymmetric condition ($\frac{d\phi(r,z)}{dr}|_{r=0} = 0$). The radial distribution of gas and solid transport properties can be determined from Equation

5.10, provided characteristics values of two coefficients $c_{\phi i}$ for each transport property at any cross-section of the riser. The characteristic values for $c_{\phi i}$ can be determined from local properties of each phase at wall boundary (ϕ_w) and center line (ϕ_0) at any cross-section of the riser. As detailed below, The centerline ($r = 0$) property (ϕ_0) of each phase at any cross-section of riser can be written as

$$\phi_0 = c_{\phi 0} \tag{5.11}$$

The property of transport parameter at wall (r = R) at any cross-section of riser can be written as

$$\phi_w = c_{\phi 2} R^2 + c_{\phi 0} \tag{5.12}$$

Reorganize Equations 5.11 and 5.12, the characteristic values of coefficient $c_{\phi i}$ at any cross-section of the riser can be expresses as function of ϕ_w and ϕ_0,

$$c_{\phi 0} = \phi_0 \tag{5.13}$$

$$c_{\phi 2} = \frac{\phi_w - \phi_0}{R^2} \tag{5.14}$$

Insert the above $c_{\phi 0}$ and $c_{\phi 2}$ to Equation 5.10,

$$\phi(r, z) = \frac{\phi_w - \phi_0}{R^2} r^2 + \phi_0 \tag{5.15}$$

From the parabolic approximation, radial distribution of property $\phi(r, z)$ can be determined provided with its local value at wall boundary and centerline. Equation 5.15 gives an explicit expression for transportation properties in the integral terms in Equations 5.1 to 5.4. To differentiate from 1-D modeling, the heterogeneous modeling with consideration of continuous radial profile is named as Continuous Modeling.

The cross-section area average of volume fraction ($\bar{\alpha}$) at any cross-section of riser is then defined as

$$\bar{\alpha} \equiv \frac{1}{A}\int_0^A \alpha\left(r,z\right)dA \tag{5.16}$$

Based on Equation 5.15,

$$\bar{\alpha_i} = \frac{\alpha_{iw}+\alpha_{i0}}{2}, (i=g,s) \tag{5.17}$$

The cross-section average of velocity ($\bar{U}$) at any cross-section of riser is defined as

$$\bar{U} \equiv \frac{\int \alpha U dA}{\int \alpha dA} = \frac{\overline{\alpha U}}{\bar{\alpha}} \tag{5.18}$$

With a simple integration, velocity of both solid and gas phases can be expressed in matrix form as,

$$\bar{U_i} = \frac{\begin{pmatrix}\alpha_{iw} & \alpha_{i0}\end{pmatrix}\begin{pmatrix}2 & 1\\ 1 & 2\end{pmatrix}\begin{pmatrix}U_{iw}\\ U_{i0}\end{pmatrix}}{3\begin{pmatrix}\alpha_{iw} & \alpha_{i0}\end{pmatrix}\begin{pmatrix}1\\ 1\end{pmatrix}}, (i=g,s) \tag{5.19}$$

With definitions in Equations 5.16 and 5.18, Equations 5.1 to 5.4 can be rewritten as,

$$\frac{d}{dz}\left(\bar{\alpha}_g\rho_g\bar{U}_gA\right) = 0 \tag{5.20}$$

$$\frac{d}{dz}\left(\bar{\alpha}_s\rho_s\bar{U}_sA\right) = 0 \tag{5.21}$$

$$\frac{d}{dz}\left(\rho_g\bar{\alpha}_g\overline{U_gU_g}A\right) = -\bar{\alpha}_g\rho_ggA - \frac{dp}{dz}A - \int f_D dA \tag{5.22}$$

$$\frac{d}{dz}\left(\bar{\alpha}_s\rho_s\overline{U_sU_s}A\right) = -\bar{\alpha}_s\rho_sgA + \int f_D dA - \int f_C dA \tag{5.23}$$

Here $\overline{UU}$ for both gas and solid phases in Equations 5.22 and 5.23 is defined as,

$$\overline{UU} \equiv \frac{\int \alpha U U dA}{\int \alpha dA} = \frac{\overline{\alpha UU}}{\bar{\alpha}} \tag{5.24}$$

Omitting the redundant integration, $\overline{U_i U_i}, (i = g, s)$ is given in matrix form as function of α_i and U_i,

$$\overline{U_i U_i} = \frac{\begin{pmatrix} \alpha_{iw} & \alpha_{i0} \end{pmatrix} \begin{pmatrix} 3 & 1 & 2 \\ 1 & 3 & 2 \end{pmatrix} \begin{pmatrix} U_{iw}^2 \\ U_{i0}^2 \\ U_{i0} U_{iw} \end{pmatrix}}{6 \begin{pmatrix} \alpha_w & \alpha_0 \end{pmatrix} \begin{pmatrix} 1 \\ 1 \end{pmatrix}}, (i = g, s) \tag{5.25}$$

Introducing more unknowns (ϕ_w, ϕ_0) by polynomial approximation allows all terms to be integrated out, yet requires more equations (intrinsic mechanisms) to approach problem closure. The volume fraction constrain in Equation 5.8 now can be split into two equations,

$$\alpha_{gw} + \alpha_{sw} = 1 \tag{5.26}$$

and

$$\alpha_{g0} + \alpha_{s0} = 1 \tag{5.27}$$

Now there are 14 unknowns (α_{s0}, α_{sw}, $\bar{\alpha}_s$, α_{g0}, α_{gw}, $\bar{\alpha}_g$, u_{s0}, u_{sw}, $\bar{u}_s$, u_{g0}, u_{gw}, $\bar{u}_g$, p and ρ_g) and 11 independent Equations (5.20, 5.21,5.22, 5.23, 5.17(2), 5.19(2), 5.26, 5.27 and 5.9), which describes the axial heterogeneous flow structure in terms of cross-section averaged flow parameters ($\bar{\alpha}_s$, $\bar{u}_s$, $\bar{u}_g$, and p). To close the problem for heterogeneous flow structure in both radial and axial directions, additional intrinsic mechanisms (e.g., radial transport) or boundary conditions should be provided.

5.2.3 Intrinsic Mechanism and Problem Csslosure

Boundary condition The non-slip condition of gas phase at the wall boundary provides that

$$U_{gw}(z) = 0 \tag{5.28}$$

Solids at the wall sliding down by gravity will be subjected to friction resistance from the wall boundary. Most published literature used friction force or friction factor between the solid particles and wall to determine the solid velocity at the wall, which can be expressed as

$$\tau_{sw} = \frac{1}{2} f_s \alpha_{sw} \rho_s {U_{sw}}^2 \tag{5.29}$$

Where, f_s represent friction factor. The above equation is derived by balancing the pressure drop per unit length due to the wall-shear friction with the weight of the particles from pipe flow theory. Note that the core-annulus interface friction is neglected. To determine the average particle velocity in the wall regime from Equation 5.29, the axial distribution of wall shear stress and average solid volume fraction need to be known. Also the core and wall regime need to be pre-defined to obtain average solid phase flow properties in wall regime. Instead of dealing with so many unknowns/uncertainties to determine particle velocity at wall regime, in this study a correlation with single adjustable parameter is proposed.

$$U_{sw} = \bar{U}_s \exp\left(-\beta \frac{z}{H}\right) - U_{pt} \tag{5.30}$$

Here β is an adjustable coefficient, which is a function of the riser operation conditions.

Solid radial transportation assumption The riser wall blocks the radial movement of both gas and solid phase. The radial transport of the solids in riser flow is mainly due to the turbulent fluctuation induced particle transport and collision diffusive mass transfer of solids particles.

The intensity of turbulent convection induced mass transfer of solids is mainly dependent on local intensity of gas turbulence and the velocity gradient of particles in the radial direction and is from high turbulent fluctuation of the particles to the low turbulent fluctuation of particles. The intensity of particle collision induced diffusive mass transfer is dependent on the local solids concentration and the concentration gradient of particles in the radial direction, the direction is from high concentration to low concentration. At steady state, time and space averaged net mass transportation of particles through the core-anulus boundary is balanced, which gives;

$$\overline{<\alpha'_s \rho_s V'_{sT}>}\,|_{r_c^-} = \overline{<\alpha'_s \rho_s V'_{sD}>}\,|_{r_c^+} \tag{5.31}$$

Where r_c is the radius of core-anulus boundary. It can be expressed by setting $U_s = 0$, which will give,

$$r_c = \sqrt{\frac{U_{s0} R^2}{U_{s0} - U_{sw}}} \tag{5.32}$$

The radial transport of the particles due to the turbulence induced particle fluctuation can be best approximated in terms of its main stream velocity at the center of the riser,

$$\overline{<V'_{sT}>}\,|_{r_c^-} = k_{sT} U_{s0} \tag{5.33}$$

Here k_{sT} represents turbulent fluctuation induced radial transport coefficient for particles, which was estimated as function of ratio of particle Stokes number to Reynolds number.

$$k_{sT} = f(\frac{\mathrm{St}}{\mathrm{Re_p}}) \tag{5.34}$$

Using Boussinesqs approximation [6] by introducing a transport coefficient, thus the right term in Equation 5.31 can be expressed as;

$$\overline{<\alpha_s{}' V_{sD}{}'>}\,|_{r_c^+} = -D_{sD} \cdot \nabla \alpha_s\,|_{r_c} \tag{5.35}$$

Here D_{sD} is radial transport coefficient for particles due to radial concentration gradient.

In sum, the riser wall boundary and solids radial transportation mechanism provides an additional three physics based constitutive equations (Equations 5.28, 5.30 and 5.31). Thus, the proposed model reaches closure.

5.3 Result and Discussion

The heterogeneous model is partially validated by comparing model predictions against literature experimental data for both axial and radial evolution of phase transport properties. The model is calibrated for axial predictions by comparing model predictions for cross-sectional averaged solids volume fraction and pressure gradient against experiment data. Then predictions of radial distribution of solid volume concentration and velocity were compared against literature data. The core-wall boundary and particle back-mixing mass flux is also calculated and analyzed.

5.3.1 Operating and Inlet Condition

To solve the foregoing system of governing equations requires appropriately prescribed operating and inlet conditions. The experimental operating condition from literature [57] is applied in this modeling for further comparison. The height of riser is 10 m long, with internal diameter 76 mm. The diameter of FCC catalysts particles is 67 μm with density of 1500 kg/m^3. Randomly, the operating case of 300 kg/s-m^2 solid supply with 8 m/s gas velocity is selected. The proper inlet conditions are set as follow. At riser inlet, solid flow is assumed to be fairly uniform with volume fraction of 0.35, while nonuniform for gas phase. The centerline velocity for gas phase is determined from its average velocity. The inlet pressure p_0 is estimated by iteration that making sure exit pressure reasonably agree with the measurements. The radial

transport coefficients for gas-solids phase are presumed to predict appropriate axial and radial distribution of transport properties.

5.3.2 Model Validation

Provided with above inlet and operational conditions, the sets of coupled equations (ODEs) can be solved numerically by 5^{th} order of Runge-Kutta method. In this section, the modeling results are illustrated and plotted against reported experimental data [57]. More results of axial and radial profile of hydrodynamic characteristics are also presented.

Figures 5.5, 5.6 and 5.7 give the solid volume fraction, gas velocity and solid velocity axial profile along the riser height, respectively. Figure 5.5 indicates that solid volume fraction at the centerline and wall region follow the same pattern of dilution along axial direction as its average value.

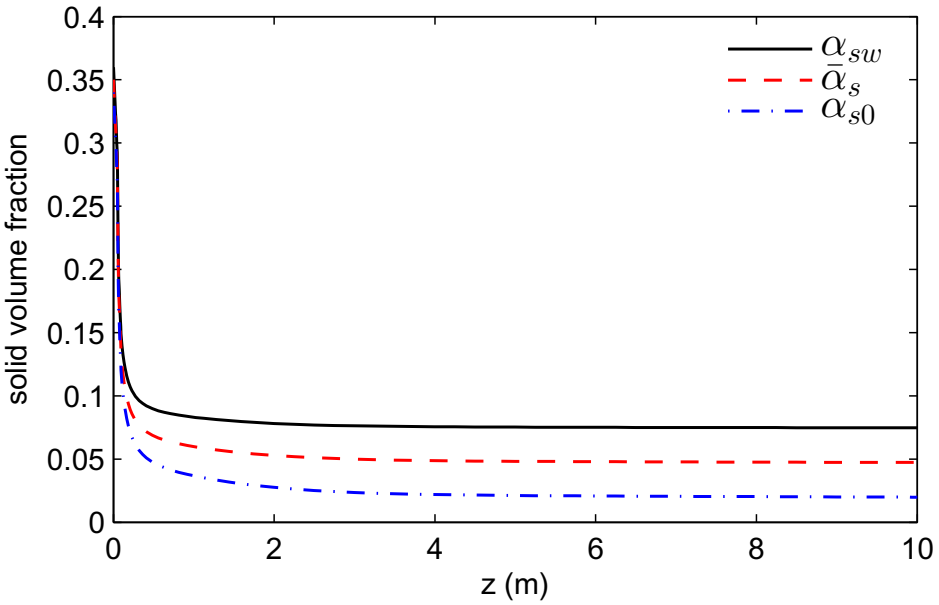

Figure 5.5 Solid volume fraction axial profile.

Figure 5.6 shows the likeness of gas phase velocity between values of average and centerline, both of which decrease rapidly at the bottom of riser due to the large drag from dense solid phase then gradually increase in dilute regime as pressure falling.

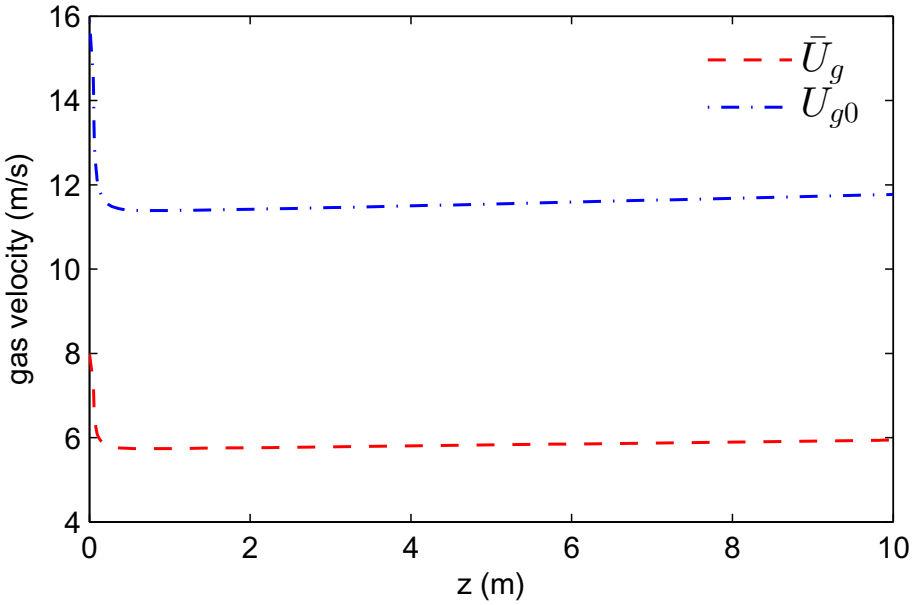

Figure 5.6 Gas phase velocity axial profile.

Figure 5.7 shows that solids are slowly catching up the speed and continues speeding up until reaching up to terminal velocity at the centerline. Note that solids velocity at the wall region will starts reducing when the upward inertia is neutralized away by gravity and collision. At and above certain level, solids at wall lose the upward driven inertia and the velocity turns to negative meaning that particles are sliding down (back flow).

Figure 5.8 gives the axial profile of pressure and gas phase density along riser, which shows the decreasing pattern as expected.

The predicted radial profile of solid velocity at different height comparing against experimental data [57] is plotted in Figure 5.9. Same variable in non-dimensional form is also plotted in Figure 5.10. Both figures indicate that modeling results on solid velocity radial profile at different height fairly agree with the data,

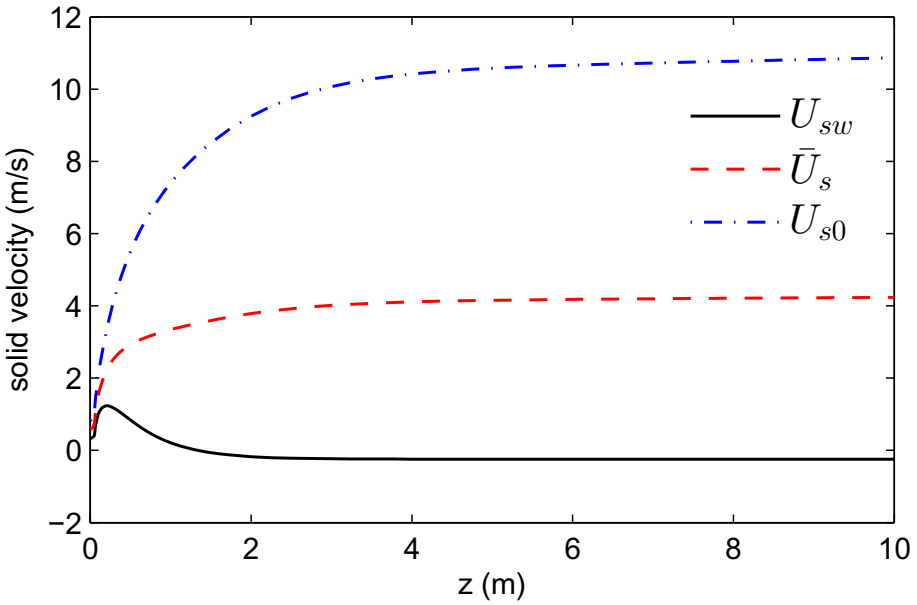

Figure 5.7 Solid velocity axial profile.

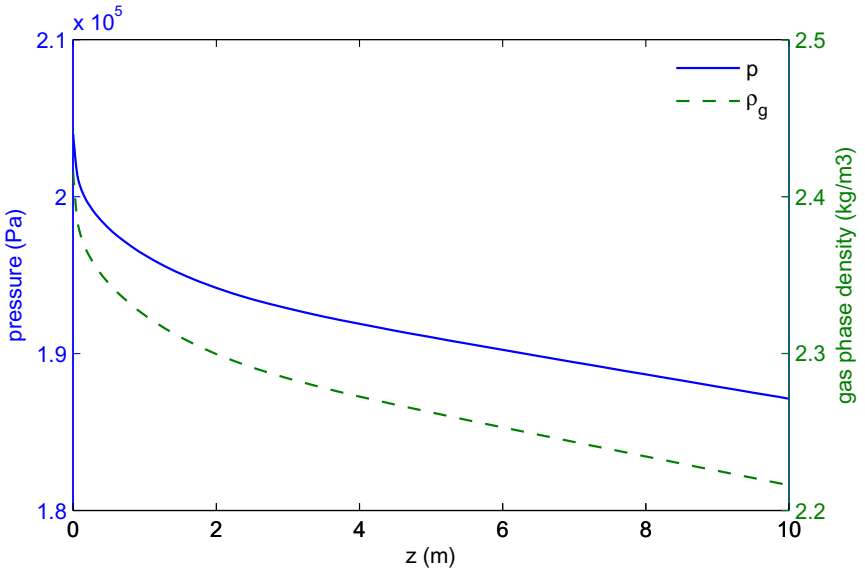

Figure 5.8 Pressure and gas phase density axial profile.

especially at lower height of riser. When solids transport up to the upper part of riser, the flow comes to fully developed turbulent condition. Thus its radial profile becomes more uniform in the center with relatively thin boundary layer at the wall.

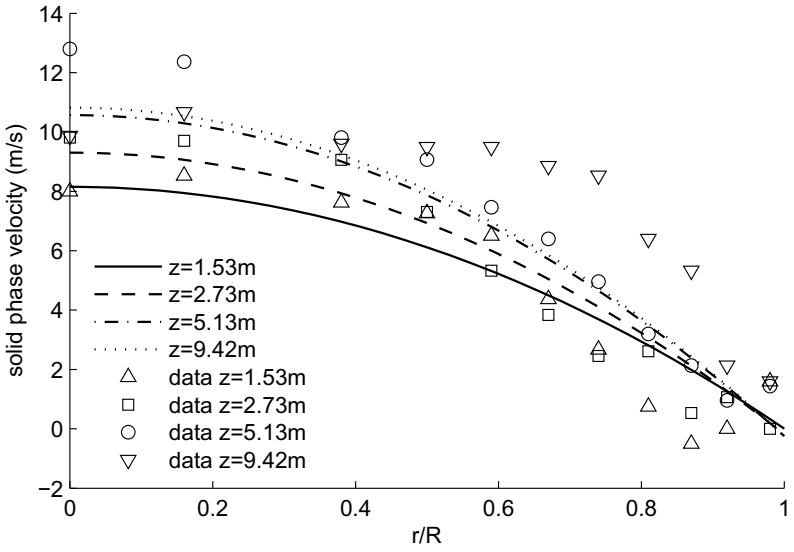

Figure 5.9 Radial profile of solid velocity comparing with data at different height.

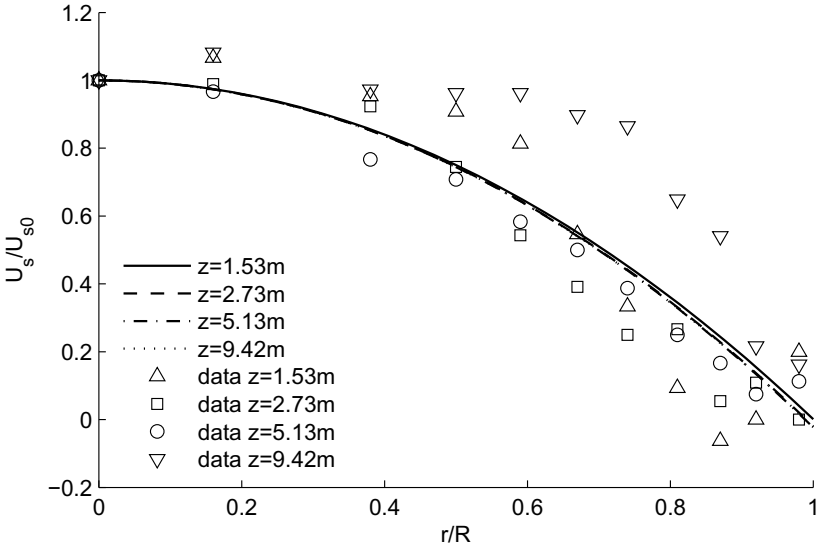

Figure 5.10 Radial profile of non-dimensional solid velocity comparing with data at different height.

Although parabolic approximation at top of riser may not perform so well as the rest, the prediction and measurements are within the same order of magnitude overall.

Figure 5.11 plots radial profile of non-dimensional solid volume fraction at different height against with experimental data [81], showing well agreements in between.

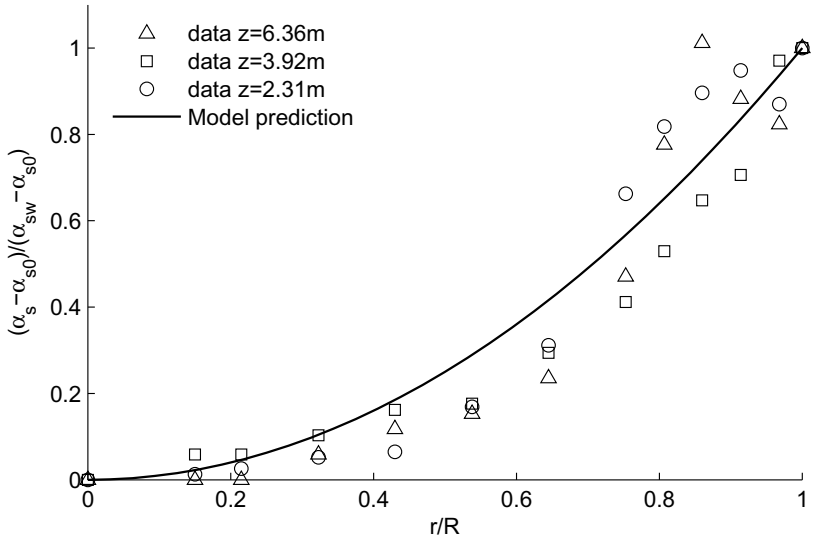

Figure 5.11 Radial profile of non-dimensional solid volume fraction comparing with data at different height.

Figures 5.12 to 5.15 show the radial profile of hydrodynamic characteristics (e.g., velocity and concentration of both gas and solid phases) develops along riser. Echoing to gas axial profile (Figure 5.6), Figure 5.12 shows that during a very short distance above riser inlet, gas velocity (especially in center) decrease rapidly. Gas velocity will increase a little after passing through the dense regime. Figure 5.13 shows that starting from a roughly uniform flow, solids in center gradually gain more momentum than those at wall. Most of solid velocity is gained in acceleration regime, which is right after dense regime. Solids velocity at wall, instead of accelerating, starts falling down soon. Figure 5.14 gives the non-dimensional solid velocity profile at different height of riser, which indicating that solids flow will become more and more non-uniform and showing certain similarity when reaching fully developed flow. Figure 5.15, shows a quick fall of solid volume fraction at lower bottom of riser. Figure

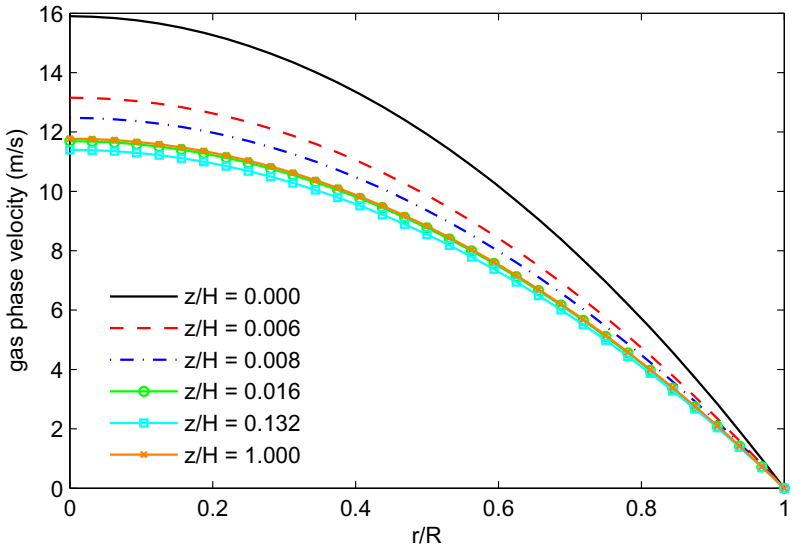

Figure 5.12 Radial profile of gas velocity at different height.

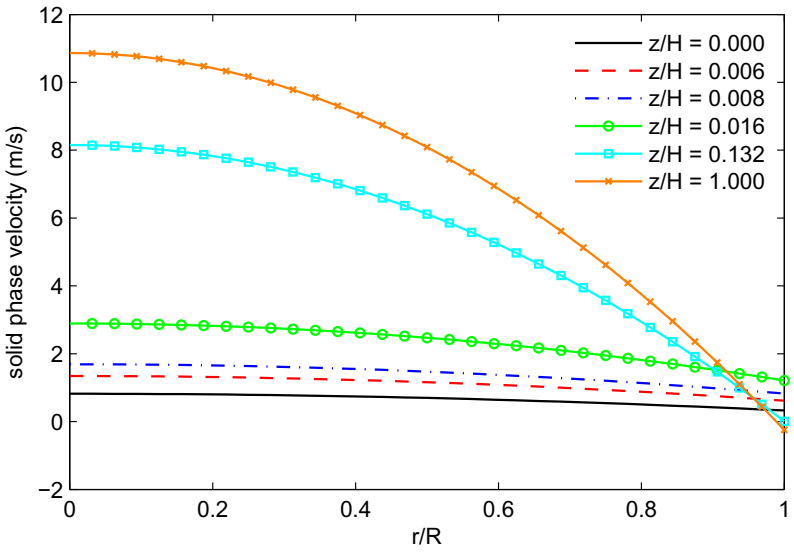

Figure 5.13 Radial profile of solid velocity at different height.

5.16 shows the calculated back flow boundary along riser.

5.4 Conclusion

In this chapter, a continuous model was developed to describe the heterogeneous structure of gas-solids riser flow in both radial and axial directions. The model

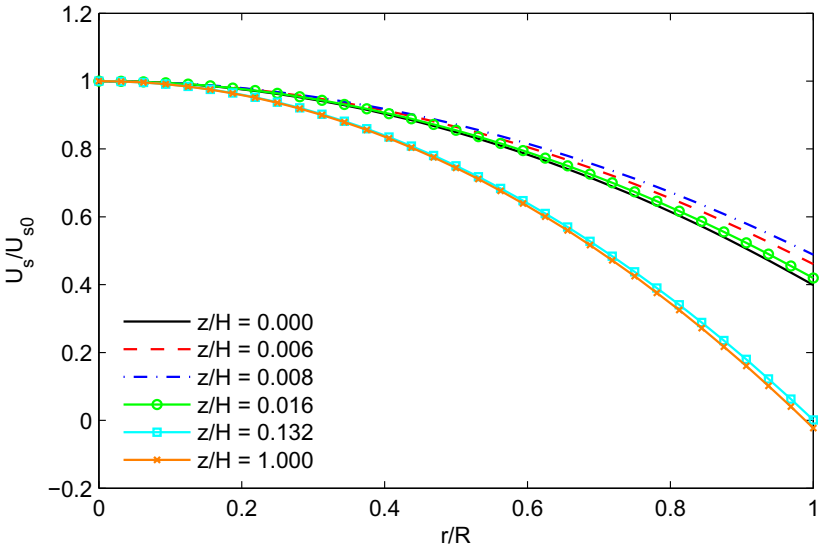

Figure 5.14 Radial profile of non-dimensional solid velocity at different height.

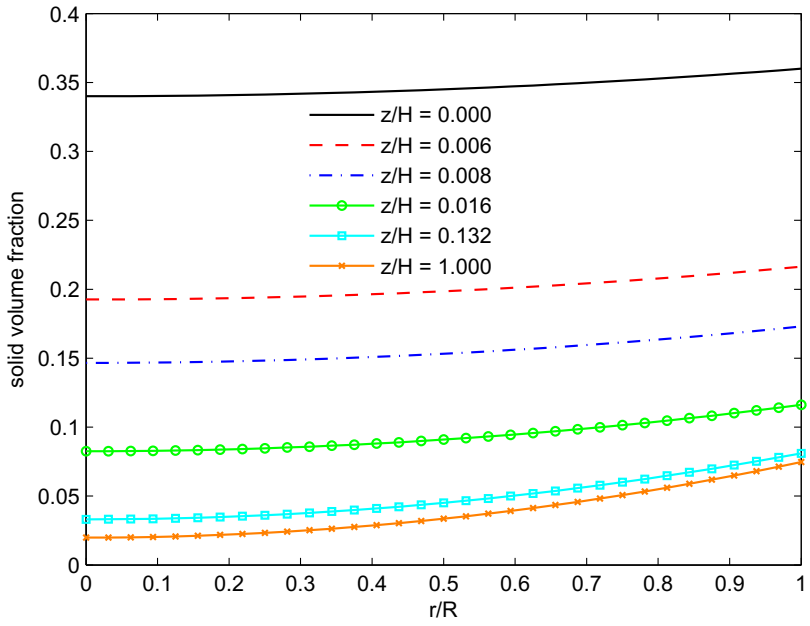

Figure 5.15 Radial profile of solid volume fraction at different height.

adopted integral-differential form of governing equations based on mass and momentum conservation of gas and solids phases. The 2nd order polynomials are used to represent the radial profiles of hydrodynamic parameters of riser flow. A radial transport

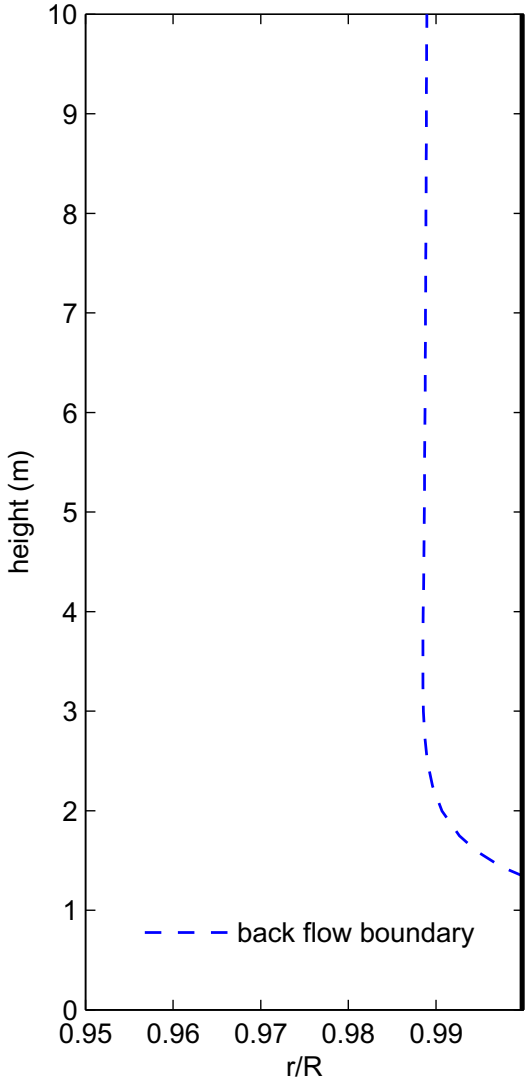

Figure 5.16 Solid back flow boundary

mechanism, which accounts for the turbulent and diffusive transport balance between core and anulus regime, are proposed for the closure of the problem. The model predictions on the radial and axial profiles of key hydrodynamic parameters such as pressure drop, solids volume fraction and velocity are validated with previously published experimental data. A typical example is then analyzed for the radial and

axial evolution of heterogeneous structure of riser flow. Key parameters such as upwards flow boundary, back-mixing ratio are then analyzed and discussed.

CHAPTER 6

CONCLUSION AND SUGGESTION FOR FUTURE RESEARCH

6.1 Summary of Current Study

This dissertation study is aim to understand the complicated phenomenon with the mechanisms of heat, momentum and mass transfer between liquid, solid and gas phases coupled with reaction in the upward riser flow. The major topics include spray impingement caused solids wetting and solid-droplet collision probability distributions, the multi-evaporating spray trajectory and their interactions throughout the ambient gas-solid flow coupled with reaction, two-zone gas-solid transportation with reaction considering entrance (pre-cracking) effect, and the wall boundary restricted solid back-flow in the gas-solid transportation.

The major contributions can be summarized below:

1) A two-zone model for fluid catalytic cracking (FCC) riser with multiple feed injectors is proposed and developed to successfully predict yield and conversion against commercial data. Heat transfer model between vapor and catalysts in riser reactor is coupled into above model to account for different temperature axial profiles of solid and gas phase, which affects hydrodynamics (pressure and velocity) and reaction (product yield and conversion) [37];

2) Multi-spray interaction model, coupled with vaporization and vapor-cracking, is built up to simulate hydrodynamics and kinetic reactions in feed injection zone, which provide corresponding inlet condition for gas-solid transport in downstream of riser [59];

3) An innovative experimental methodology for statistical characterization of collision-based liquid attachment and momentum transfer is performed [36];

4) The continuous model for describing hydrodynamic heterogeneous structure of

gas-solids riser flow in both radial and axial directions is proposed and partially validated with published data [35].

6.2 Suggestions on Future Study

Some future study is suggested and listed here:

1) Current liquid attachment study assumes collision below Leidenfrost temperature which might be justifiable due to the porous structure of catalytic particles, while the effect of heat transfer above Leidenfrost temperature deserve to be future considered.

2) The cross section average concept in two-zone model can be further improved by taking the radial non-uniformity effect into account. The taper effect (cross area change) in feed zone may be also considered in the future.

3) Better modeling of solid velocity at wall regime and solid radial migration is an option for improving continuous model. Further integration of continuous model to reaction model is suggested to describe the FCC process in riser reactor more precisely.

BIBLIOGRAPHY

[1] GN Abramovich. *The theory of turbulent jets*. The Massachussets Institute of Technology Press, Cambridge, 1963.

[2] Ryan P Anderson and Alfonso Ortega. Experiments and modeling of a liquid droplet transported by a gas stream impinging on a heated surface: single phase regime. In *ASME 2009 InterPACK Conference collocated with the ASME 2009 Summer Heat Transfer Conference and the ASME 2009 3rd International Conference on Energy Sustainability*, pages 229–237. American Society of Mechanical Engineers, 2009.

[3] D-R Bai, Y Jin, Z-Q Yu, and J-X Zhu. The axial distribution of the cross-sectionally averaged voidage in fast fluidized beds. *Powder Technology*, 71(1):51–58, 1992.

[4] Yaghoub Behjat, Shahrokh Shahhosseini, and Mahdi Ahmadi Marvast. CFD analysis of hydrodynamic, heat transfer and reaction of three phase riser reactor. *Chemical Engineering Research and Design*, 89(7):978–989, 2011.

[5] LW Bolton and JF Davidson. Recirculation of particles in fast fluidized risers. *Circulating Fluidized Bed Technology II*, pages 139–146, 1988.

[6] Joseph Boussinesq. *Essai sur la théorie des eaux courantes*, volume 2. Imprimerie nationale, 1877.

[7] J Scott Buchanan. Analysis of heating and vaporization of feed droplets in fluidized catalytic cracking risers. *Industrial & Engineering Chemistry Research*, 33(12):3104–3111, 1994.

[8] Walter Büssing and Lothar Reh. On viscous momentum transfer by solids in gas–solids flow through risers. *Chemical Engineering Science*, 56(12):3803–3813, 2001.

[9] CANMET. Development of a pilot-scaled nozzle to simulate the performance of a full-scale tebm-2b coker feed nozzle. *Research Dept. Progress Report*, 35(11), 2006.

[10] S-L Chang and CQ Zhou. Simulation of FCC riser flow with multiphase heat transfer and cracking reactions. *Computational Mechanics*, 31(6):519–532, 2003.

[11] Gary Christensen, Minas R Apelian, Karlton J Hickey, and Stephen B Jaffe. Future directions in modeling the FCC process: An emphasis on product quality. *Chemical Engineering Science*, 54(13):2753–2764, 1999.

[12] A Corma and J Martinez-Triguero. Kinetics of gasoil cracking and catalyst decay on sapo-37 and usy molecular sieves. *Applied Catalysis A: General*, 118(2):153–162, 1994.

[13] Asit K Das, Juray De Wilde, GJ Heynderickx, GB Marin, Jan Vierendeels, and Erik Dick. CFD simulation of dilute phase gas-solid riser reactors: part I - A new solution method and flow model validation. *Chemical Engineering Science*, 59(1):167–186, 2004.

[14] Céline Derouin, David Nevicato, Michel Forissier, Gabriel Wild, and Jean-René Bernard. Hydrodynamics of riser units and their impact on fcc operation. *Industrial & Engineering Chemistry Research*, 36(11):4504–4515, 1997.

[15] Andres J Diaz and Alfonso Ortega. Numerical investigation of a liquid droplet transported by a gas stream impinging on a heated surface: single-phase regime. In *Thermal and Thermomechanical Phenomena in Electronic Systems (ITherm), 2010 12th IEEE Intersociety Conference on*, pages 1–9. IEEE, 2010.

[16] Bing Du, W Warsito, and Liang-Shih Fan. ECT studies of the choking phenomenon in a gas–solid circulating fluidized bed. *AIChE journal*, 50(7):1386–1406, 2004.

[17] PM Dupuy, N Kleinohl, M Fernandino, HA Jakobsen, and HF Svendsen. Droplet–surface impact at high pressures. *Chemical Engineering Science*, 65(19):5320–5343, 2010.

[18] Sabri Ergun. Fluid flow through packed columns. *Chem. Eng. Prog.*, 48, 1952.

[19] L-S Fan, R Lau, C Zhu, K Vuong, W Warsito, X Wang, and G Liu. Evaporative liquid jets in gas–liquid–solid flow system. *Chemical Engineering Science*, 56(21):5871–5891, 2001.

[20] Liang-Shih Fan and Chao Zhu. *Principles of gas-solid flows*. Cambridge University Press, 1998.

[21] M Forissier, M Formenti, and JR Bernard. Effect of the total pressure on catalytic cracking reactions. *Catalysis Today*, 11(1):73–83, 1991.

[22] Hitoshi Fujimoto, Yu Shiotani, Albert Y Tong, Takayuki Hama, and Hirohiko Takuda. Three-dimensional numerical analysis of the deformation behavior of droplets impinging onto a solid substrate. *International Journal of Multiphase Flow*, 33(3):317–332, 2007.

[23] Yang Ge and L-S Fan. Three-dimensional simulation of impingement of a liquid droplet on a flat surface in the leidenfrost regime. *Physics of Fluids*, 17(2):027104, 2005.

[24] Yang Ge and L-S Fan. 3-D modeling of the dynamics and heat transfer characteristics of subcooled droplet impact on a surface with film boiling. *International Journal of Heat and Mass Transfer*, 49(21):4231–4249, 2006.

[25] Yang Ge and L-S Fan. Droplet–particle collision mechanics with film-boiling evaporation. *Journal of Fluid Mechanics*, 573:311–337, 2007.

[26] Sebastian Gehrke and K-E Wirth. Liquid feed injection in a high-density riser. *Chemical Engineering & Technology*, 31(11):1701–1705, 2008.

[27] ŽB Grbavčić, RV Garić, S Dj Jovanović, and Lj S Rožić. Hydrodynamic modeling of vertical accelerating gas-solids flow. *Powder Technology*, 94(2):91–97, 1997.

[28] Ajay Gupta and D Subba Rao. Effect of feed atomization on FCC performance: simulation of entire unit. *Chemical Engineering Science*, 58(20):4567–4579, 2003.

[29] Raj Kumar Gupta, Vineet Kumar, and VK Srivastava. A new generic approach for the modeling of fluid catalytic cracking (FCC) riser reactor. *Chemical Engineering Science*, 62(17):4510–4528, 2007.

[30] In-Su Han and Chang-Bock Chung. Dynamic modeling and simulation of a fluidized catalytic cracking process. part II: Property estimation and simulation. *Chemical Engineering Science*, 56(5):1973–1990, 2001.

[31] Francis H Harlow and John P Shannon. The splash of a liquid drop. *Journal of Applied Physics*, 38(10):3855–3866, 1967.

[32] BJ Harris and JF Davidson. Modelling options for circulating fluidized beds: a core/annulus deposition model. *Circulating Fluidized Bed Technology IV*, page 32, 1994.

[33] N Hatta, H Fujimoto, and H Takuda. Numerical analysis of flow pattern of impinging liquid sprays in a cold model for cooling a hot flat plate. *Applied Scientific Research*, 50(2):129–147, 1993.

[34] Natsuo Hatta, Hitoshi Fujimoto, and Hirohiko Takuda. Deformation process of a water droplet impinging on a solid surface. *Journal of Fluids Engineering*, 117(3):394–401, 1995.

[35] Pengfei He, Rajesh Patel, Dawei Wang, and Chao Zhu. A continuous model of axial and radial flow structure. *Powder Technology, in preparation.*

[36] Pengfei He, Dawei Wang, and Chao Zhu. Liquid attachment and momentum transfer by collisions between free-fall solids and liquid spray droplets. *Powder Technology*, 239:1–11, 2013.

[37] Pengfei He, Chao Zhu, and Teh C. Ho. A two-zone model for fluid catalytic cracking riser with multiple feed injectors. *AIChE J, to be submitted.*

[38] Blaine Herb, Suisheng Dou, Kemal Tuzla, and John C Chen. Solid mass fluxes in circulating fluidized beds. *Powder Technology*, 70(3):197–205, 1992.

[39] Teh C Ho. Modeling of reaction kinetics for petroleum fractions. *Practical Advances in Petroleum Processing*, pages 653–694. Springer, 2006.

[40] Teh C Ho. Kinetic modeling of large-scale reaction systems. *Catalysis Reviews*, 50(3):287–378, 2008.

[41] Masayuki Horio, Kenji Morishita, Osamu Tachibana, and Naoki Murata. Solid distribution and movement in circulating fluidized beds. *Circulating Fluidized Bed Technology II*, pages 147–154, 1988.

[42] Allan S Issangya, John R Grace, Dingrong Bai, and Jingxu Zhu. Further measurements of flow dynamics in a high-density circulating fluidized bed riser. *Powder Technology*, 111(1):104–113, 2000.

[43] X Jia, JB McLaughlin, and K Kontomaris. Lattice boltzmann simulations of drops colliding with solid surfaces. *The European Physical Journal Special Topics*, 171(1):105–112, 2009.

[44] Mooson Kwauk, N Wang, Y Li, B Chen, and Z Shen. Fast fluidization at ICM. *Circulating Fluidized Bed Technology*, 33:62, 1986.

[45] Xingying Lan, Chunming Xu, Gang Wang, Li Wu, and Jinsen Gao. CFD modeling of gas–solid flow and cracking reaction in two-stage riser fcc reactors. *Chemical Engineering Science*, 64(17):3847–3858, 2009.

[46] Liang-Sun Lee, Yu-Wen Chen, Tsung-Nien Huang, and Wen-Yen Pan. Four-lump kinetic model for fluid catalytic cracking process. *The Canadian Journal of Chemical Engineering*, 67(4):615–619, 1989.

[47] Arthur Lefebvre. *Atomization and sprays*. CRC press, 1988.

[48] Tingwen Li, Konstantin Pougatch, Martha Salcudean, and Dana Grecov. Numerical modeling of an evaporative spray in a riser. *Powder Technology*, 201(3):213–229, 2010.

[49] Youchou Li and Mooson Kwauk. The dynamics of fast fluidization. *Fluidization*, pages 537–544. Springer, 1980.

[50] Jianzhong Lin, Lijuan Qian, and Hongbin Xiong. Relationship between deposition properties and operating parameters for droplet onto surface in the atomization impinging spray. *Powder Technology*, 191(3):340–348, 2009.

[51] Gabriela Cantarelli Lopes, LM Rosa, Milton Mori, José Roberto Nunhez, and Waldir Pedro Martignoni. Three-dimensional modeling of fluid catalytic cracking industrial riser flow and reactions. *Computers & Chemical Engineering*, 35(11):2159–2168, 2011.

[52] M Louge and H Chang. Pressure and voidage gradients in vertical gas-solid risers. *Powder Technology*, 60(2):197–201, 1990.

[53] MY Louge, E Mastorakos, and JT Jenkins. The role of particle collisions in pneumatic transport. *Journal of Fluid Mechanics*, 231:345–359, 1991.

[54] CHR Mundo, M Sommerfeld, and C Tropea. Droplet-wall collisions: Experimental studies of the deformation and breakup process. *International Journal of Multiphase Flow*, 21(2):151–173, 1995.

[55] Subramanya V Nayak, Saket L Joshi, and Vivek V Ranade. Modeling of vaporization and cracking of liquid oil injected in a gas–solid riser. *Chemical Engineering Science*, 60(22):6049–6066, 2005.

[56] JJ Nieuwland, R Meijer, JAM Kuipers, and WPM Van Swaaij. Measurements of solids concentration and axial solids velocity in gas-solid two-phase flows. *Powder Technology*, 87(2):127–139, 1996.

[57] JH Pärssinen and J-X Zhu. Particle velocity and flow development in a long and high-flux circulating fluidized bed riser. *Chemical Engineering Science*, 56(18):5295–5303, 2001.

[58] Rajesh Patel. Ph.D. Thesis: Modeling of non-uniform hydrodynamics and catalytic reaction in a solids-laden riser. 2011.

[59] Rajesh Patel, Pengfei He, Bo Zhang, and Chao Zhu. Transport of interacting and evaporating liquid sprays in a gas–solid riser reactor. *Chemical Engineering Science*, 100:433–444, 2013.

[60] Rajesh Patel, Dawei Wang, Chao Zhu, and Teh C Ho. Effect of injection zone cracking on fluid catalytic cracking. *AIChE Journal*, 59(4):1226–1235, 2013.

[61] Isabelle Pitault, David Nevicato, Michel Forissier, and Jean-René Bernard. Kinetic model based on a molecular description for catalytic cracking of vacuum gas oil. *Chemical Engineering Science*, 49(24):4249–4262, 1994.

[62] JL Platten and JE Keffer. Entrainment in deflected axisymmetric jets at various angles to the stream. *Tech. Rep.*, page 6808, 1968.

[63] X-B Qi, W-X Huang, and Jesse Zhu. Comparative study of flow structure in circulating fluidized bed risers with FCC and sand particles. *Chemical Engineering & Technology*, 31(4):542–553, 2008.

[64] Muhammad MR Qureshi, Chao Zhu, Chao-Hsin Lin, and Liang-Shih Fan. Effect of nozzle fan angle on sprays in gas-solid riser flow. *China Particuology*, 4(3):147–152, 2006.

[65] Muhammad Mushahid Rafique Qureshi and Chao Zhu. Crossflow evaporating sprays in gas–solid flows: Effect of aspect ratio of rectangular nozzles. *Powder Technology*, 166(2):60–71, 2006.

[66] Martin Rein. Phenomena of liquid drop impact on solid and liquid surfaces. *Fluid Dynamics Research*, 12(2):61, 1993.

[67] MJ Rhodes and D Geldart. A model for the circulating fluidized bed. *Powder Technology*, 53(3):155–162, 1987.

[68] MJ Rhodes, M Sollaart, and XS Wang. Flow structure in a fast fluid bed. *Powder Technology*, 99(2):194–200, 1998.

[69] JF Richardson and WN Zaki. Sedimentation and fluidisation: Part I. *Trans. Inst. Chem. Eng.*, 32:35–53, 1954.

[70] P Schlichthaerle and J1 Werther. Axial pressure profiles and solids concentration distributions in the CFB bottom zone. *Chemical Engineering Science*, 54(22):5485–5493, 1999.

[71] Ulises A Sedran. Laboratory testing of FCC catalysts and hydrogen transfer properties evaluation. *Catalysis Reviews*, 36(3):405–431, 1994.

[72] Richard C Senior and Clive Brereton. Modelling of circulating fluidised-bed solids flow and distribution. *Chemical Engineering Science*, 47(2):281–296, 1992.

[73] David C Skouby. Hydrodynamic studies in a 0.45-m riser with liquid feed injection. In *AIChE Symposium Series*, volume 95, pages 67–70. New York, NY: American Institute of Chemical Engineers, 1971-c2002., 1999.

[74] KN Theologos, AI Lygeros, and NC Markatos. Feedstock atomization effects on fcc riser reactors selectivity. *Chemical Engineering Science*, 54(22):5617–5625, 1999.

[75] KN Theologos and NC Markatos. Advanced modeling of fluid catalytic cracking riser-type reactors. *AIChE Journal*, 39(6):1007–1017, 1993.

[76] Albert Y Tong, Saurabh Kasliwal, and Hitoshi Fujimoto. On the successive impingement of droplets onto a substrate. *Numerical Heat Transfer, Part A: Applications*, 52(6):531–548, 2007.

[77] BGM Van Wachem, JC Schouten, CM Van den Bleek, R Krishna, and JL Sinclair. CFD modeling of gas-fluidized beds with a bimodal particle mixture. *AIChE Journal*, 47(6):1292–1302, 2001.

[78] Dawei Wang, Zheng Shen, and Chao Zhu. Phase transfer in a droplet–solid sphere collision. In *AIChE Annual Meeting, Philadelphia, PA*, 2008.

[79] Xiaohua Wang, Chao Zhu, and Rajesh Ahluwalia. Numerical simulation of evaporating spray jets in concurrent gas–solids pipe flows. *Powder Technology*, 140(1):56–67, 2004.

[80] Vern W Weekman and Donald M Nace. Kinetics of catalytic cracking selectivity in fixed, moving, and fluid bed reactors. *AIChE Journal*, 16(3):397–404, 1970.

[81] Fei Wei, Hongfei Lin, Yi Cheng, Zhanwen Wang, and Yong Jin. Profiles of particle velocity and solids fraction in a high-density riser. *Powder Technology*, 100(2):183–189, 1998.

[82] Aijie Yan and Jesse Zhu. Scale-up effect of riser reactors (1): axial and radial solids concentration distribution and flow development. *Industrial & Engineering Chemistry Research*, 43(18):5810–5819, 2004.

[83] AL Yarin. Drop impact dynamics: splashing, spreading, receding, bouncing. *Annu. Rev. Fluid Mech.*, 38:159–192, 2006.

[84] Jun You, Rajesh Patel, Dawei Wang, and Chao Zhu. Role of inter-particle collision on solids acceleration in riser. *Particuology*, 8(1):13–18, 2010.

[85] Zhao Yu, Yang Ge, and L-S Fan. Multi-scale simulation of oblique collisions of a droplet on a surface in the leidenfrost regime. *Chemical Engineering Science*, 62(13):3462–3472, 2007.

[86] C Zhu, SC Liang, and L Sh Fan. Particle wake effects on the drag force of an interactive particle. *International Journal of Multiphase Flow*, 20(1):117–129, 1994.

[87] C Zhu, GL Liu, X Wang, and L-S Fan. A parametric model for evaporating liquid jets in dilute gas–solid flows. *International Journal of Multiphase Flow*, 28(9):1479–1495, 2002.

[88] Chao Zhu, You Jun, Rajesh Patel, Dawei Wang, and Teh C Ho. Interactions of flow and reaction in fluid catalytic cracking risers. *AIChE Journal*, 57(11):3122–3131, 2011.

[89] Chao Zhu, Xiaohua Wang, and Liang-Shih Fan. Effect of solids concentration on evaporative liquid jets in gas–solid flows. *Powder Technology*, 111(1):79–82, 2000.

[90] Chao Zhu, Xiaohua Wang, Guangliang Liu, and Liang-Shih Fan. A similarity model of evaporating liquid spray jets in concurrent gas–solid flows. *Powder Technology*, 119(2):292–297, 2001.

[91] Chao Zhu, Jun You, Dawei Wang, and Liang-Shih Fan. Modeling on heterogeneous structure in acceleration regime of gas-solid riser flows. In *The 12th International Conference on Fluidization-New Horizons in Fluidization Engineering*, page 13. bepress, 2007.